A novel approach to decomposing and identifying individual magnetohydrodynamic wave modes in sunspots.

Abdulrahman Albidah

Supervisors:
Dr Istvan Ballai
Dr Gary Verth
Dr Viktor Fedun

The University Of Sheffield.

University of Sheffield

School of Mathematics and Statistics

A thesis submitted in partial fulfilment of the requirements for the degree of

Doctor of Philosophy

April, 2022

Acknowledgements

First of all, I express my great thanks to God.

I would like to convey my heartfelt thanks to the numerous people who helped me complete my thesis with their help, encouragement and guidance.

- Drs. Istvan Ballai, Gary Verth, and Viktor Fedun, my supervisors, deserve my sincere gratitude for their encouragement and support during my Ph.D. studies. Thanks to their scientific, unique, and smart help, I overcame numerous challenges and accomplished this assignment effectively; working under their supervision was an honour and pleasure for me.

- I owe a debt of gratitude to my parents and grandparents, who have always believed in my ability to earn my Ph.D. and have always encouraged me to do so. I appreciate all of their love, generosity, and support throughout the years. None of this would have been possible without you.

- My wife, Afnan Altwala, deserves a particular thanks for being my first supporter, and loving wife during my education journey. I appreciate her patience, cheerfulness, and all of the optimism she has given towards me. I am happy to dedicate this thesis to you.

- I want to express my gratitude to my children, Hisham and Shahykhah, for their love, smiles, support, and happiness that they have shown me throughout the years. I want to express my gratitude to my family and friends for their support.

- Dr. Yi Li, my adviser, for his encouragement, unwavering support, and academic guidance.

- Dr. Jonathan Higham for his help with in the methodology of mode decomposition.

- Prof. David Jess and Conor MacBride for providing the dataset and the observations information (see sections 4.2, 5.2 and 6.2) of sunspots that have been used in this Thesis.

- Dr. Anwar Aldhafeeri for providing the theoretical modes of the Elliptical flux tube model, and her help with the model of the irregular cross-sectional shape.

- Dr. Suzana Silva for her suggestions and help during my studies.

I want to thank the Saudi Government, Ministry of Education, Majmaah University, the Royal Embassy of Saudi Arabia in London, the Saudi Cultural Bureau in London for supporting my studies at the University of Sheffield.

Declaration of Authorship

I hereby declare that, except where clear reference is made to the work of others, the contents of this dissertation are original and have not, in whole or in part, been submitted to this or any other university for consideration for any other degree or qualification. This dissertation is my own work and contains nothing which is the outcome of work done in collaboration with others, except as specified in the text and Acknowledgements. This dissertation contains fewer than 80,000 words including appendices, bibliography, footnotes, tables, figures and equations.

Abdulrahman Albidah
Tuesday 5th April, 2022

Abstract

High resolution solar observations show the complexity of the temporal and spatial structure of the magnetohydrodynamic (MHD) wave motion, that makes the identification of the nature and properties of waves rather difficult. In general, observations of waves in solar magnetic structures are limited to the determination of one single wave that turns out to be the most energetic one, i.e. having the largest amplitude. Based on mechanical analogy of waves in elastic media, it would be natural to expect the appearance of other modes, too. However, these eluded the observers for many years. The present Thesis aims to address this shortcoming and propose new methods for wave identification.

In particular, in this Thesis, we are applying both the Proper Orthogonal Decomposition (POD) and Dynamic Mode Decomposition (DMD) techniques on solar observational data. These techniques are well documented and validated in the areas of fluid mechanics, hydraulics, and granular flows, yet are relatively new to the field of solar physics. While POD identifies modes based on orthogonality in space and it provides a clear ranking of modes in terms of their contribution to the total variance of the signal, DMD resolves modes that are orthogonal in time, i.e. different modes cannot have identical frequencies.

The clear presence of the fundamental slow body sausage ($n = 0$) and kink ($n = 1$) modes, as well as the higher-order modes ($n \geq 2$) has been evidenced based on the POD and DMD analysis of chromospheric Hα observation for sunspots with a circular and elliptical cross-sectional shapes. Additionally to the various slow body modes, evidence for the presence of the fast surface kink mode was found in the circular sunspot.

Moreover, for a further analysis, the assumption of changing of the boundary's shape with time is considered on a long time period of chromospheric HMI sunspot with a circular cross-sectional shape.

All the MHD modes patterns recovered from observations were cross-correlated with their theoretically predicted counterparts and we demonstrated that the higher-order MHD wave modes were more sensitive to the changes in the umbral cross-sectional shape, hence this must be taken into account for more accurate modelling of the resonant modes of sunspots and pores.

List of Publications

This Thesis is based on the following publications:

- Albidah AB, Brevis W, Fedun V, Ballai I, Jess DB, Stangalini M, Higham J, Verth G. 2021 Proper orthogonal and dynamic mode decomposition of sunspot data. Phil. Trans. R. Soc. A 379: 20200181. URL: http://dx.doi.org/10.1098/rsta.2020.0181
- Albidah, A. B., Fedun, V., Aldhafeeri, A. A., Ballai, I., Brevis, W., Jess,D. B., Higham, J., Stangalini, M., Silva, S. S. A. and Verth, G. (2022), 'Magnetohydrodynamic wave mode identification in circular and elliptical sunspot umbrae: Evidence for high-order modes', The Astrophysical Journal 927(2), 201. URL: https://doi.org/10.3847/1538-4357/ac51d9
- Albidah AB, Fedun V, Aldhafeeri AA, Ballai I, Brevis W, Jess DB, MacBride C, Higham J, Stangalini M, Silva SSA, Verth G. 2021 Temporal evaluation of MHD waves in sunspots (in a final stage of preparation).

Contents

List of Figures

List of Tables

CHAPTER 1

Introduction

1.1 A brief overview of the history of solar science

The Sun is a fascinating celestial object that has piqued people's curiosity for thousands of years and it has been a source of scientific attraction and research. Despite centuries of discoveries related to the Sun, scientists are still puzzled by a number of solar phenomena that still elude their full explanation. The Sun is the primary source of energy in the solar system and, given its proximity, it is the most studied star. The following historical overview has been adopted from (Hufbauer, 1991; Hawking, 2002; Priest, 2014).

Solar observations have a long history, dating back to records of eclipses by Chinese astronomers as early as 2000 BC. Possibly the first record of sunspots was made by Chinese astronomers about 800 BC, and later in 300 BC by the ancient Greeks. Their observation of the dark spots was with no explanation. The earliest mention of corona, which has the highest temperature in the solar atmosphere, was on 22 December 968 during a complete eclipse and is credited to Leo Diaconus, a Byzantine scholar.

The 17th century can be considered as a starting point for the study of many of astronomical phenomena that helped in their interpretation and understanding. Galileo Galilei and Thomas Harriot made the first observations of sunspots with telescopes in 1610. Later, in 1612, Galilei began a more thorough analysis of the solar spots, concluding that the Sun rotated about its own axis based on the spot's apparent motion over the solar disc (see the left panel of Figure 1.1). However, in the 18th century, the physical nature of sunspots caused a lot of debate as they were assumed to be cloud-like formations or thick objects in the solar atmosphere.

During the 19th century, the newly developed spectroscopical techniques led to a real revolution in the fields of solar and astronomical studies. The

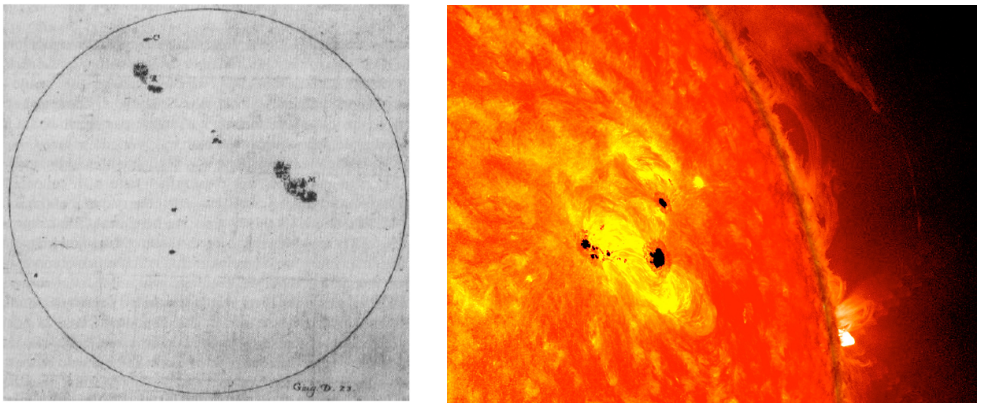

Figure 1.1: Left panel shows the sunspot drawn by Galileo Galilei in 1612. The right panel shows the active region on the Sun with dark sunspots. Credit: *Solar Dynamics Observatory (SDO)*

modern space study is considered to begin with these observations and that marks the beginning of the fundamental era for Solar Physics. In the 1830s, the French physicist Claude Pouillet was the first to defined the Sun's energy output as the 'solar constant'. Besides monitoring sunspot activity, astronomers went even further and investigated what is known as the sunspot cycle. The sunspot cycle is defined as the change in the number of sunspots that begins at its lowest point, increases to a maximum of about 250 sunspots, and then decreases back to its lowest point. Schwabe was the first scientist to recognize that the number of sunspots changes periodically in time (Arlt, 2014). In 1843 he established the 11-year sunspot period. In 1858, Richard Carrington and Gustav Spörer discovered that the position of sunspots and their motion varies with time and latitude. They showed that sunspots have a faster movement over the solar surface when they are closer to the solar equator. Hence, Carrington concluded that our Sun has a differential rotation. In 1959, Carrington and Hodgson observed the solar flare for the first time.

In the beginning of the 20th century, research in the properties of our Sun received a new impetus with the advancement of observational accuracy and new observational facilities. The optical resolution of the observations had increased as a result of the invention of a new kind of tower telescope by Hale (1908*b*). In the same year, using the Zeeman splitting of spectral lines in umbral regions of sunspots, Hale (1908*a*) was able to determine the magnetic nature of the sunspots and found that sunspots had significant magnetic fields. By the middle of the 20th century, major advances have been achieved in the quantitative behaviour of solar phenomena using the newly formulated theory of magnetohydrodynamics (MHD) by Hannes Alfvén (see. Alfvén, 1942). This

theory describes how magnetic fields impact the dynamic of solar atmospheric plasma (a detailed description of the MHD framework will be presented in Chapter 2). In addition, the study by Parker (1958) predicted the existence of the solar wind, which nowadays is one of the most studied parts of the heliosphere, given its impact on Earth. In 1962 Leighton et al. (1962) determined that the surface of the Sun undergoes a periodic up and down motion, with an average period of 5 minutes. These oscillations were explained in terms of pressure-driven standing sound waves (or p-modes) that are able to penetrate deep layers of the solar interior, making them an ideal tool for the seismological studies (helioseismology). In 1969, Jacques Beckers and Paul Tallant made the first detection of waves in the sunspot umbra (Beckers and Tallant, 1969). Since my Thesis deals with waves propagating in the umbral regions of sunspots, a detailed review of the results related to these waves is presented later in this Chapter.

1.2 Physical properties and the structure of the Sun

Our Sun, located in the centre of the solar system, is an exceedingly inhomogeneous sphere of plasma. It mostly consists of H (92%) and He (8%), with the other heavier components, such as C, N, and O, accounting for less than 0.1 %. Due to the high temperatures, the atoms are mostly ionised, especially in the solar interior and solar corona, where temperatures can reach million degrees. The Sun is characterised by the presence of a strong magnetic field that drives and controls the activity of the Sun's atmosphere, generating features such as sunspots (Section 1.3), prominences, coronal mass ejections (CMEs), spicules, the solar wind, etc. The majority of the current section is based on work by Aschwanden (2004); Priest (2014), and should be considered as references, unless a different reference is stated.

The Sun has a mass of about 1.99×10^{30} kg, which is about 330,000 times the mass of the Earth. The Sun losses of its mass at a rate of about $1-1.5\times10^{9}$ kg s^{-1} (Parker, 1958). The radius of the Sun is about 695.5 Mm, which is 109 times larger than the radius of the Earth. The gravitational acceleration at the surface is 274 m s^{-2}, which is 27 times grater that of the Earth, while the mean density of the Sun, which is 1.4×10^{3} kg m^{-3}, is roughly equal to that of the Earth (5.5×10^{3} kg m^{-3}). The average distance between the Sun and the Earth is 149.6 million kilometres (1 astronomical unit), and light takes

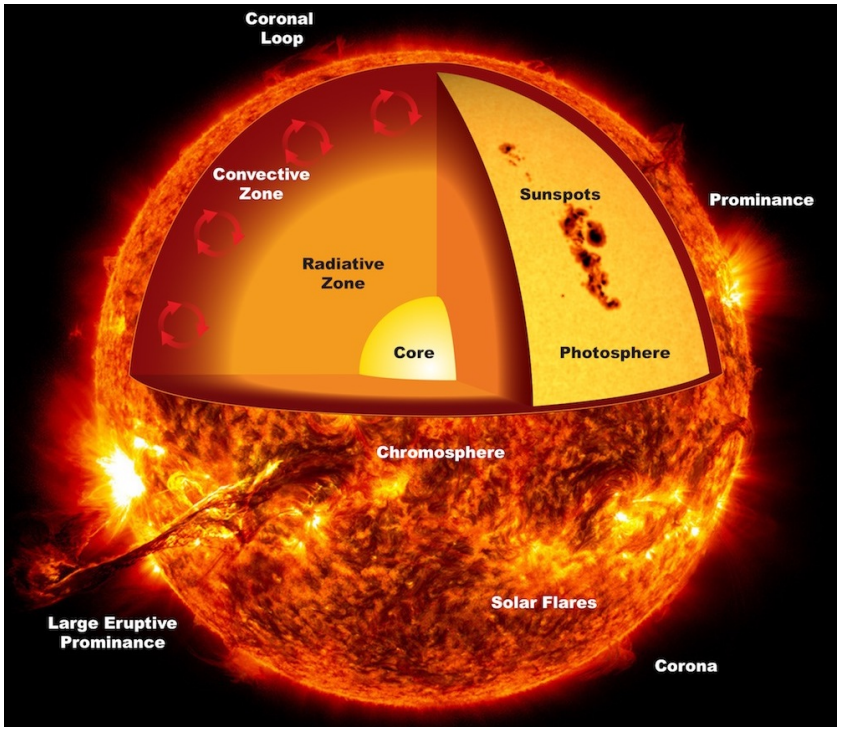

Figure 1.2: The structure of the Sun. The opaque inner layers are the core, radiative zone, and convective zone, while the visible outer layers are the photosphere, chromosphere, and corona. The figure also shows some observable solar atmospheric phenomena, such as solar flares, prominences, sunspots and coronal loops. Credit: *The Space Place Webpage of NASA*

approximately 8 minutes to cover that distance (Capitaine et al., 2012). The Sun has a differential rotation, with an equatorial and polar cycle of 25-days and 34-days respectively.

Traditionally the Sun is divided into its interior and atmosphere, where only the atmosphere can be observed in different wavelengths. The solar interior consists of three regions: the core, the radiative zone and the convective zone. The solar atmosphere consists of several regions, each with its own properties. First, at the solar surface we have the photosphere, which is the visible thin and relatively cool layer of the atmosphere, followed the chromosphere that shows a slight increase of the temperature comparing with the photosphere, but is very dynamic. At the top of the chromosphere we have a thin transition region, where the temperature has a two orders of magnitude increase. Finally, the multi-million degree corona extends from the transition region out into the solar wind (see Figure 1.2).

1.2.1 The solar interior

The core of the Sun is the main source of solar energy, where 99% of the solar energy is generated, due to nuclear fusion reactions. Here hydrogen atoms fuse together to form helium and an enormous amount of energy. The core extends from the center of the Sun to about 25% of its radius. The mass of the core is approximately 34% of the Sun's mass, whereas it is only 8% of the Sun's volume. The density of the solar core is approximately 150 times that of water, tremendous pressures up to 265 billion bar, and temperatures up to 15 million kelvin (K).

The radiative zone is the layer just above the core, and it extends up to about 70% of the solar radius. The temperature and the density in the radiative zone decrease dramatically as we go upward from the bottom to the top, from about 7 million K to about 2 million K and 20 g/cm^3 to 0.2 g/cm^3. Photons, that are generated in the core, take about 170,000 years to cross the layer, where the layer is incredibly opaque. If this layer would be optically thin, it would take only 2 seconds for photons to cross this layer (Mitalas and Sills, 1992).

The convection zone is the top part of the solar interior, where the outward energy transportation is dominated by convection. The convective motions can be visibly recognised as granules and supergranules at the solar surface. The convection zone extends from about 70% to 100% of the Sun's radius. As we go upward from the bottom of the convection zone to the solar surface, the temperature drops from 2 million K to about 6000 K.

1.2.2 The solar atmosphere

It is widely believed that magnetic dynamo effects are responsible for creating the solar magnetic inside the Sun due to electrical currents generated by the flow of hot, ionized gases in the convection zone. Convective plasma motion can lift up the magnetic field taking it to the surface of the Sun, where it emerges in the form of flux tubes of different intensity. Due to the differential rotation of the Sun, the magnetic field lines are twisted up like a coil. The strong magnetic fields are responsible for the activities that appear in the solar atmosphere, generating features such as solar flares, sunspots, solar prominences and coronal loops. The solar atmosphere is the observable part of the Sun and it is divided into four layers: photosphere, chromosphere, transition region, and corona (see Figure 1.2). These layers are mostly dispersed

according to density and temperature (See Figure 1.3). Moreover, the effect of the magnetic field in the layers of the solar atmosphere varies from one to another. The dynamical behaviour of the plasma can be understood in terms of the so called plasma-β parameter, that can be defined as the ratio of the plasma pressure to the magnetic pressure. The magnitude of this parameter (relative to 1) also tells us whether pressure forces or magnetic forces are dominant. In the solar photosphere plasma-$\beta \gg 1$, so the plasma motion is driven mainly by pressure forces. In contrast, in the solar corona plasma-$\beta \ll 1$, meaning that magnetic forces are responsible for the behaviour and evolution of the plasma. Knowing the origin of the high temperature in the corona is one of the most critical problems in solar physics (the coronal heating problem is one of the most acute unexplained problems in solar and stellar physics).

Most of the Sun's visible light is emitted from the photosphere, which is the lowest layer of the Sun's atmosphere. The photosphere is a relatively thin layer, around 500 km thick, and is the densest region of the solar atmosphere. As we go upward, from the bottom to the top of the layer, the temperature drops by around 2000 Kelvin and reaching the minimum temperature (See Figure 1.3). The photosphere has some features that are related to solar magnetic activity or convection such as granules and sunspots. The granules are the small convection cells that cover the Sun's surface, and the intergranular lanes are the locations where the magnetic field emanates to the surface. The granules have lifetime of 1 to 20 minutes, and the diameters ranging from 0.3 to 2 Mm.

Sunspots are identified as dark spots with predominantly vertical magnetic field on the surface of the Sun that are cooler than the surrounding region (see left panel of Figure 1.5). A more detailed description of sunspots will given in Section 1.3.

In the following 1,500-2,000 km thick layer, the chromosphere, the temperature increases with height up to approximately 10,000 K at the top of the layer. The magnetic field becomes more inclined forming the magnetic network and it is responsible for the existence of several phenomena in the chromosphere such as prominences and spicules. On the Sun's surface, prominences are luminous ionised gas eruptions that may stretch thousands of kilometres from the chromosphere to corona (Buss, 1926). Spicules are defined as dynamic jets that stretch from the photosphere to the chromosphere (Tavabi et al., 2012).

At the interface between the chromosphere and corona, we have the approximately 100 km thick layer called the transition region. In this layer, the

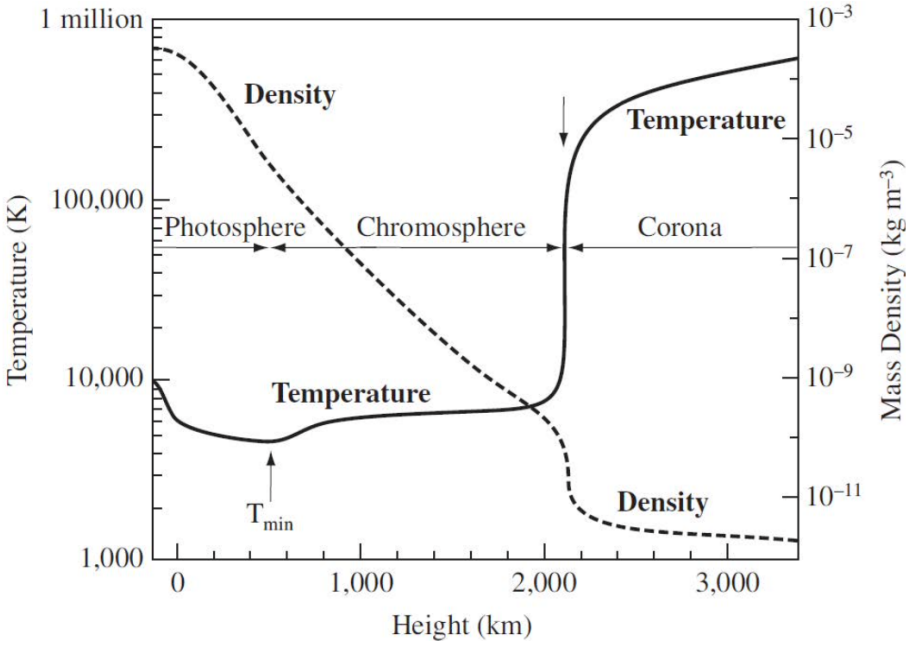

Figure 1.3: The average variation of density and temperature with height in the solar atmosphere based on the solar atmospheric model developed by Avrett and Loeser (2008)

temperature increases dramatically from 10,000 K up to a million Kelvin.

The solar corona is the uppermost part of the Sun's atmosphere and extends millions of kilometres outwards. The density of corona is 10 million times less than that of the sun's surface, therefore corona appears significantly less luminous than the Sun's surface. During eclipses, the corona is seen as a pale halo of low density and high temperature as shown in the left panel of Figure 1.4. The solar corona shows a very strong magnetic structuring into coronal loops of different lengths and thicknesses. Coronal loops are described as magnetic arcs that originate and terminate in the Sun surface (see Figure 1.4). The length of the coronal loops is depending on the activity region, where the small active-region loops have a length in the range of 1 Mm to 10 Mm. The length of the standard active-region loops is 100 Mm, and it extends to 1,000 Mm for giant arches. The flaring loops have temperatures up to 10 MK, while it is 2-3 MK in the active-region loops and 10^5 K for quiet, cool loops. The corona is the birthplace of many very energetic phenomena, such as flares and coronal mass ejections (CMEs) thanks to interconnecting magnetic fields of different polarity. Each of such interaction (also called magnetic reconnection) comes with a huge amount of energy and particle release that are expelled into the interplanetary space.

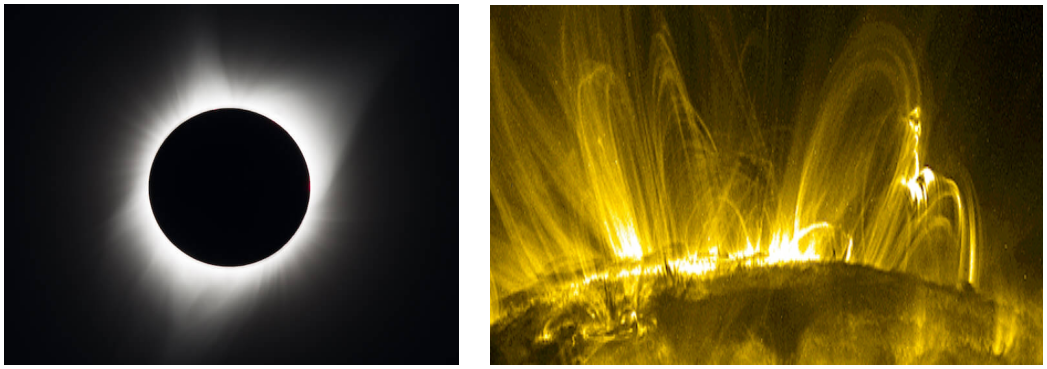

Figure 1.4: The left panel shows the glowing white corona that can be seen surrounding the Sun during a total solar eclipse, when the moon blocks out the bright light of the Sun. The right panel shows coronal loops as seen in Extreme Ultra Violet (EUV) 171 Å. Credit: *The Space Place Webpage of NASA*

1.3 Sunspots

Sunspots observations have played a significant role in the history and development of solar physics, as they were the first solar objects to be identified using a telescope more than four centuries ago. The rotation of the Sun was demonstrated with the help of the sunspots' movement over the solar disc. Furthermore, the rate of solar rotation was discovered to be differential, since sunspots rotate at a faster pace when they are nearer to the solar equator than at higher latitudes. The 11-year sunspot cycle was discovered due to the temporal fluctuation of sunspot numbers. Sunspots appear preferentially at heliographic latitudes of roughly $\pm 35^{\circ}$ at the start of a sunspot cycle, while they appear at latitudes of around $\pm 5^{\circ}$ at the end of the solar cycle.

1.3.1 The Structure of Sunspots and their Properties

At first glance, sunspots seem to be distinct darker spots on the Sun's surface, however they are the most visible manifestation of the rather complex solar magnetism. Their diameters vary from 3.5 Mm to more than 60 Mm, while the largest spots are visible by the human eye (Solanki, 2003). Due to the spread of the strong magnetic field lines from the solar interior through the surface, complex sunspot regions arise and the convection of plasma is inhibited. Therefore, sunspots look darker and colder by a few thousand degrees than the surrounding areas, hence they emit less energy (see Figure 1.5). The lifetimes of sunspots are proportionate to their diameter, thus a spot with a diameter of 10 Mm lasts 2 to 3 days, while one with a diameter of 60 Mm lasts

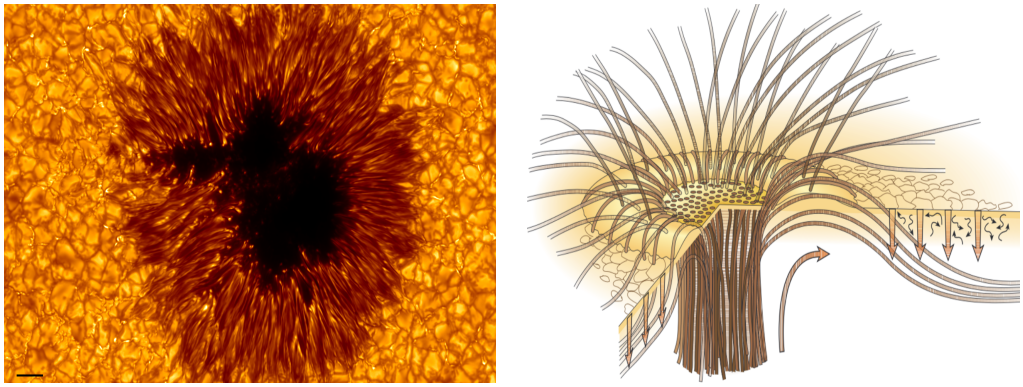

Figure 1.5: Left panel shows a high-resolution observation of a sunspot, where the central dark area is the umbra, surrounded by penumbra. The region outside the sunspot shows the dense pattern of granular cells. Credit: *The Swedish Solar Telescope (SST)* The right panel displays a sketch of the magnetic field topology in sunspots. The brown lines show the distribution of magnetic field lines in the umbra, penumbra and granular vicinity of the spot. The arrows illustrate the convection motion. Credit: Thomas et al. (2002)

80 to 90 days.

In general, sunspots are divided into two regions: the umbra, which is the central darkest region, and the surrounding penumbra, which is brighter than the umbra, as shown in the left panel of Figure 1.5. The umbra has a radius of about 40% of the radius of the sunspot. Moreover, the magnetic field strength changes gradually with the radius of the sunspot. The magnetic field lines are approximately vertical in the umbra, while they are more inclined in the penumbra, as shown in the right panel of Figure 1.5. In the penumbra, the inclination of the magnetic field lines is changing from 40° in the inner penumbra to almost 80° in the outer penumbra (Langhans et al., 2005). The umbra has a typical magnetic field strength of about 2.8 kG (0.28 T), while the typical magnetic field in the penumbra is less than 900 G (0.09 T) (see. Balthasar and Schmidt, 1993; Thomas et al., 2002). Livingston et al. (2006) observed the strongest solar magnetic fields in the umbral region at 6.2 kG (0.62 T). Kopp and Rabin (1992) have shown that the relation between the temperature and magnetic field strength, across the diameters of six sunspots is nonlinear and the magnetic field strength diminishes as the temperature increases.

The umbra develop a fully surrounding penumbra when the magnetic field strength is strong. In contrast, when the magnetic field strength of the umbra is not strong enough, we may only have a half-sided penumbra or even no penumbra at all (see. Schlichenmaier et al., 2010; Jurčák et al., 2015). In the

absence of the penumbra, the small spots on the Sun surface are called pores with typical diameters of the order of 1-7 Mm. The pores include much smaller bright structures as the heat flow from below is not completely suppressed. When the magnetic field strength is increased in the pores, the pores are developed and constitute the initial step of sunspot evolution. The magnetic field strength at the centre of the pores is in the range between 1.8 kG and 2.3 kG, while at the edge of the pores the strength is dropping to 1 kG. The active regions on the Sun's surface appear as bright plages of emission. Plages contain intense flux tubes and they harbour the pores, they appear within $\pm$ 30° of the Sun's equator, i.e around or surrounding sunspots.

High-resolution observations indicate that the umbral region of sunspots and pores contain some bright features, such as light bridges and umbral dots, which might be a sign of convective energy transmission. The light bridges are described as the bright features (of penumbral brightness) that divide the umbral areas into two or more irregular zones. The strength of magnetic field is reduced and tend to be more horizontal in light bridges. Moreover, the appearance of the brightening in the light bridge, or arising of a new one, might signal the sunspot's disintegration and fragmentation. The umbral dots are the bright dots that appear in sunspot's umbra and they also appear in pores. In the study by Sobotka and Hanslmeier (2005) the authors analyzed observations of two sunspots and two pores and found the umbral dots are colder than the undisturbed photosphere by 500–1000 K, and hotter than the coldest region in the umbra by 1000 K. The umbral dots are classified based on their location, central and peripheral dots. The central dots appear in the internal region of the umbra, whereas the peripheral dots appear at the boundary of the umbra. The peripheral umbral dots are brighter and have weaker (and inclined) magnetic fields than the central umbral dots. Watanabe et al. (2009) observed that umbral dots form in areas where the magnetic field is weaker and inclined, and they vanish in areas where the magnetic field is stronger and vertical.

The appearance of a sunspot varies drastically in various atmospheric layers. In the solar chromosphere and the layers above, the structure and dynamics of sunspots are governed by the magnetic field, where plasma$-\beta \ll 1$. The umbral and penumbral zones are less distinct in the chromosphere. In the lower photosphere, the strength of the magnetic field in the umbra decreases with height by 1 - 3 G km^{-1}, and in the upper photosphere and chromosphere it decreases by 0.3 - 0.6 G km^{-1} (Balthasar and Schmidt, 1993). Overall, the

strength of the magnetic field drops from 3 kG, in the lower photosphere, to below 1.5 kG, in the chromosphere and a few G in the solar corona. (Rueedi et al., 1995).

Superpenumbral fibrils are chromospheric loops (5 Mm high) that create virtually radial patterns around a mature sunspot, and they may be stretching out the boundary of the penumbra. It is reported that superpenumbral fibrils that appear around a sunspot are powered by the oscillations of the sunspot. Chae et al. (2014) have observed an outward propagation that arises from the internal region and then developed into the fibrils. Moreover, Jing et al. (2019) state that the observed flows along fibrils are unlikely to be an oscillation/wave phenomena.

Sunspots are well-known for their darkness, compared to their surrounding. However, in the transition region, sunspots are typically brighter than their surroundings, and this brightness is called the active regions (or sunspot plume). The first detection of the sunspot plume was by Foukal et al. (1974). Brynildsen et al. (2001) have observed the plume in 20 out of 21 sunspots concluding that not all sunspots have a plume. Furthermore, the authors found that most sunspot plumes display downflows of more than 25 km s^{-1} at temperatures close to 250,000 K.

1.4 Waves and Oscillations in Sunspots

The study of solar oscillations started with the discovery of standing pressure waves (acoustic p-modes) that are able to penetrate into the deep layers of the solar interior and have an upper reflecting point in the photosphere (Leighton et al., 1962). Naturally, the way the global p-modes penetrate the sunspots has attracted much attention. Beckers and Tallant (1969) determined the observational parameters of umbral flashes, a phenomena in which a sunspot exhibits oscillatory behaviour. Later, Bhatnagar (1971) discovered Doppler velocity oscillations in sunspots of the order of $180 - 220s$. One year later, Beckers and Schultz (1972) observed the 3-min oscillation of the vertical velocity of the umbral sunspot. The problem of Doppler velocity oscillations has been further addressed by Moore (1981), who found Doppler velocity oscillations of the order of $120 - 180s$ in the umbral region, and $240 - 300s$ in the penumbral region. Bhatnagar and Tanaka (1972) detected oscillations with a period of $170 \pm 40s$ by measuring the intensity directly from time lapse filtergram movies.

The frequency and power of the oscillations are dependent on which layer of the atmosphere they are and the portion of the sunspot under study. Thomas et al. (1984) have shown that the wave power rises by more than a factor of ten when it approaches the chromosphere above the umbra, and the dominant peaks in the power spectra of the umbra are shifted from 3.5 mHz ($\sim$ 5-min) in the photospheric layer, to 6 mHz ($\sim$ 3-min), in the chromospheric layers. The chromospheric oscillations in the sunspots umbrae are nonlinear and produce shock waves (Lites, 1984). Later on, Lites (1986*a*), using He I line observation found a clear evidence for periodic nonlinear umbral oscillations. Moreover, Lites (1986*b*) found that there is no correlation between the areas with high oscillatory power in the range of 3-min and those with high oscillatory power in the range of 5-min. Because of this, Lites (1986*b*) claimed that the 5-min photospheric oscillations do not drive the 3-min chromospheric oscillations. Wave phenomena in sunspots have been traditionally categorized, according to their periods, into three categories as: 5-min oscillations in the sunspot at the phosphoric layer, 3-min oscillations and the umbral flashes in the chromospheric umbra and, lastly, running penumbral waves in the penumbral chromosphere (Lites, 1992).

Recently, several studies supported the claim that the dominant oscillations in sunspots and pores have periods of 5-min at photospheric heights, and 3-min at chromospheric heights, while global oscillations of sunspots, as a whole, have periods that range from hours to days (to name but a few Nagashima et al., 2007; Stangalini et al., 2011; Jess et al., 2012; Jess et al., 2015; Khomenko and Collados, 2015). In contrast, Stangalini et al. (2021) have shown for the first time that the dominant oscillations of a magnetic pore observed by means of The Interferometric BIdimensional Spectropolarimeter (IBIS) have periods of 3-min in the photosphere, instead of the expected 5-min period.

Umbral flashes are described to be the periodic brightness increases in the umbral core of chromospheric sunspots (Beckers and Tallant, 1969; Wittmann, 1969). The umbral flashes appear with periods of 2 to 3-min and they are accompanied by up and down movements with the same period and amplitudes of $\pm$10 km s^{-1} (Beckers and Schultz, 1972; Phillis, 1975), with an upward motion at the start of each flash. Rouppe van der Voort et al. (2003) have shown that the appearance of the umbral flashes is the consequence of upward shock propagation and a subsequent coherent wave spreading throughout the whole sunspot. The umbral flashes are 3–5 arcsec wide, about the same size as the umbral spots. Nevertheless, umbral flashes and umbral dots have no clear

relation (Rouppe van der Voort et al., 2003).

In the transition region, sunspot waves were firstly observed by Gurman et al. (1982) and Henze et al. (1984). They have shown considerable oscillations with periods of 2 to 3-min in line-of-sight velocity by analysing time series of spectra of eight sunspots. In sunspot umbrae, Fludra (1999, 2001) and Maltby et al. (2001) have found 3-min oscillations in transition region lines. Moreover, the presence of oscillations in the layers that above the umbra, from the lowest temperature to the upper corona was shown by O'shea et al. (2002) and Banerjee et al. (2002).

Using high-resolution observations Solar Optical Telescope (SOT) on board Hinode, Nagashima et al. (2007) have studied the spatial distribution of the power spectral density (PSD) of the oscillatory signal in and around the active region (AR) NOAA 10935. Their study was carried out by observing the photospheric oscillations in the G band, while the lower chromospheric oscillations observed by using a Ca II H band. They have found that the intensity oscillations in the umbra in the lower chromosphere, the umbral flashes, have their power peak at around 5.5 mHz (3-min), whereas, in all frequency ranges, the oscillatory power is suppressed in the photospheric line data. The relation between the 3-min and 5-min oscillation in sunspots has been studied by Zhou and Liang (2017), who showed that the running waves are propagating across the umbra–penumbra as 3-min oscillations when they are located at the umbra region, and 5-min oscillations in the penumbra region.

The running penumbral waves (RPWs) were observed moving out through the chromospheric penumbral region of the sunspot, and these waves were firstly observed by (Giovanelli, 1972; Zirin and Stein, 1972). These waves (believed to be acoustic in nature), show intensity fluctuations ranging from 10% to 20%. RPWs are propagating with a phase velocity of 10 – 20 km s^{-1} at the umbral/penumbra boundary, while at the outer boundary of the penumbra they slow down, to be in the range of 5 to 7 km s^{-1}. The fluctuation of frequencies and phase speeds between the penumbra's inner and outer edges has been investigated by Brisken and Zirin (1997) and Kobanov and Makarchik (2004). These studies have revealed the frequency of 3 mHz and the phase speed of 40 km s^{-1} are shifted at the inner edge of the penumbra to 1 mHz, and 10 km s^{-1}, at the outer edge of the penumbra. Later on, Jess et al. (2013) have explained the variance of RPWs periods by the effect of the low-frequency acoustic cutoff period.

The wavelet time series analysis has also been widely used to study MHD

wave modes and their properties in the sunspot umbra region. O'shea et al. (2002) have applied a combined wavelet and Fourier analysis on an umbral regions of an observed sunspot using different spectral lines that covers the range of temperatures from the low chromosphere to corona in order to evidence the appearance of oscillations at all investigated temperatures, with frequencies in the range of 5.4 mHz to 8.9 mHz. Christopoulou et al. (2003) have used this methodology for identification of the 3-min oscillations in the sunspot umbral region.

Recently, Jess et al. (2017) have detected slow body kink modes propagating along the azimuthal direction of a sunspot using Hα images acquired by the Hydrogen-Alpha Rapid Dynamics camera (HARDcam). The authors carried out their analysis by applying a temporal, and simultaneously, a spatial bandpass Fourier filter covering ($5 < \omega < 6.3$ mHz) and ($0.45 - 0.90$ arcsec^{-1}) to extract the dominant umbral oscillations and the larger spatial fluctuations.

Keys et al. (2018) revealed the separate existence of surface and body surface sausage modes in their study on 7 pores that had mostly an elliptical cross-section. Their analysis was carried out by taking a one-dimensional cross-cut along the pore and measuring the power at the boundary and at the centre of the pore along the time series to identify the sausage mode. To investigate whether the sausage mode is surface or body, authors assumed that the magnitude of surface waves has its maximum at the boundary and has its minimum at the center of the pore, while for the body modes the amplitude has the maximum at the center and minimum at the boundary of the pore. However, their assumption may not be fully satisfied, especially for the surface sausage mode for the pore with an approximately elliptical cross-sectional shape. As it has been recently shown by Aldhafeeri et al. (2021), the magnitude of the surface sausage mode has its maximum amplitude at the boundary along the minor axis, while it attains its minimum amplitude at the boundary along the major axis. Therefore, the assumption employed by Keys et al. (2018) may be valid only for a pore that has a cross-sectional shape close to a circle. The present Thesis, that involves the use of the POD/DMD techniques will address this issue, and show how they are reliable in the identification of surface and body modes, simultaneously.

Finally, in the study by Dorotovič et al. (2014) on two sunspots and one pore, they have detected fast and slow surface sausage waves. Using the wavelet analysis and the empirical mode decomposition (EMD), these authors also showed that the pattern of these waves corresponds to the harmonics of stand-

ing waves.

1.5 Aims and Thesis outline

The qualitative description of plasma dynamics in solar and space environment are one of the most challenging aspects of solar physics. The variety of plasma motions subject to restoring forces (e.g. pressure gradient, gravitational, Lorentz etc.) give rise to magnetohydrodynamic (MHD) waves and oscillations. In the absence of these restoring forces perturbations might evolve into laminar and turbulent flows, shocks, nonlinear patterns, etc. Waves have the property to carry energy and information about the medium in which they propagate, making them an ideal tool for plasma and field diagnostics. However, their true diagnostic potential can be put at use only if high resolution observations are available that could determine the accurate determination the nature of waves and their properties. Sunspots, which are the most studied features in the solar atmosphere, are the most prominent manifestations of the emergence of magnetic field in the lower regions of the solar atmosphere and they are often the footpoints of ARs that are able to considerably influence the space weather.

To a very large extent the traditional analysis of oscillations in sunspots involves applying Fourier analysis to provide the power spectra, and that can be carried out by integration over a region of interest (ROI) or even on pixel by pixel basis. The assumption of a sinusoidal basis in the spatial domain can be considered as a disadvantage of using Fourier analysis since we are applying it in a flux tubes models, i.e. models with a circular cross-sectional shape, see section 2.2.3, or even an elliptical shape, see section 2.2.4, where the basis functions are Bessel or Mathieu functions, respectively.

To address this inconsistency, in the present Thesis, we will use the techniques of Proper Orthogonal Decomposition (POD, (Pearson, 1901)), see section 3.1, which allows the determination of spatially orthogonal patterns from signals, and the Dynamic Mode Decomposition (DMD, (Schmid, 2010)), see section 3.2, which allows the determination of temporally orthogonal patterns. Then, we aim to apply these techniques in combination to detect the MHD wave mode in sunspots data. POD and DMD have a further advantage over Fourier analysis as they cross-correlate individual pixels over the region of interest (ROI), in the spatial and temporal domain, respectively. Furthermore, as the POD works by assuming orthogonality in space, it has the capability

to deal with adequate base functions that are orthogonal to each other by definition. The shape of the sunspot may be affected by the surrounding background and, therefore, the shape may lose the property of orthogonality in the spatial domain, and hence the advantage of using POD will be lost. However, DMD can detect modes which are still orthogonal in time. Therefore the best approach for mode identification is to use the POD and DMD techniques in combination.

This Thesis is organized as follows: in Chapter 2 we introduce the mathematical formalism appropriate to study wave propagation in the solar environment and determine the dispersion relation of waves in various configurations. To help in the identification of modes in realistic magnetic structures, we compare the findings of theoretical modeling in the case of a flux tube with circular and elliptical cross-sections.

Chapter 3 is devoted to the background of the methods used in our Thesis, namely the Proper Orthogonal Decomposition (POD) and the Dynamic Mode Decomposition (DMD) techniques. By merging numerous modes of the cylindrical flux tube model, we create a numerical synthetic dataset, for which we then use the POD and DMD to recover every single mode. This step is necessary to validate the two methods, and verify their applicability for MHD modes in realistic waveguides.

In Chapter 4 we apply the POD and DMD techniques on a dataset corresponding to a sunspot that has an approximately circular cross-sectional shape, which is, up to our knowledge, the first time to be applied on a solar physics dataset. Since the dataset has already been analysed earlier by Jess et al. (2017), our investigation will recover not only the modes identified by this study, but some higher order modes, too.

In Chapter 5 we expand our analysis of POD and DMD by applying these techniques on two datasets that correspond to sunspots whose cross-sectional shape is close to a circular and elliptical shapes. Here we show evidence of the appearance of higher-order modes and overtone modes in both sunspots. For the modes we identified in these structures, we calculate some of their physical parameters, such as their longitudinal wavenumber k_z, their phase speed V_{ph} and wavelength λ.

All previous results were obtained by assuming that the shape of the sunspots does not change in time. Of course, this is an idealistic approach, therefore in Chapter 6 we plan to address this shortcoming by applying the POD and DMD techniques in connection to a sunspot for which observational

data are available for a long time. This analysis aims to investigate how the change in the shape of the sunspot will affect the nature and morphology of the waves.

Finally, our conclusions and possible future research directions are presented in Chapter 7.

CHAPTER 2

Theoretical Background: waves in magnetic guides

Plasma - the fourth state of matter - is defined as an ionized gas that has a collective motion under the influence of electric and magnetic field. Plasma occupies most of the known universe, and our Sun is one of the most studied examples of astrophysical plasmas.

A fully ionised magnetic fluid where the temporal changes are much longer than any characteristic times for collisions between particles can be considered as a single fluid, whose dynamics can be well described within the framework of Magnetohydrodynamics (MHD). Dynamics in these systems are driven by macroscopic forces and the evolution of thermodynamic parameters are governed by the usual thermodynamic laws.

The MHD equations are governed by Maxwell's equations, ideal gas law, and the equations of mass, momentum and energy conservation. In addition, the induction equation, which connects the electromagnetic fields and fluid properties, describes the temporal evolution of the magnetic field in terms of the plasma velocity, can be obtained by combining the Maxwell's equations and Ohm's law (Priest, 2014).

High resolution observations of the last few decades showed that the solar atmospheric plasma is very dynamic, waves are present in every part of the solar plasma. Due to the interaction between the magnetic field and plasma, MHD waves can propagate along and across the field and their properties can be studied by means of dispersion relations. There are several types of wave modes with different restoring forces. Alfvén waves owe their existence to the magnetic tension, that works against any changes in the magnetic field. When magnetic pressure and plasma pressure act together, they can produce fast magneto-acoustic waves, while, if they act against each other, they can produce slow magneto-acoustic waves.

The solar plasma is far from being uniform. The magnetic field tends to accumulate into smaller or larger structures, such as sunspots, prominences,

spicules, coronal loops, etc. Waves are observed to be connected to these structures and their investigation requires an approach that assumes that waves are somehow guided along the field. That is why an accurate description of waves in the solar atmosphere requires the analysis of waves propagating along various waveguides. The most used models in solar physics study the wave propagation along a magnetic interface (Roberts, 1981*a*), guided by magnetic slabs (Edwin and Roberts, 1982) or magnetic cylinders (Edwin and Roberts, 1983). Clearly the dispersion relation of these waves will depend on the particular waveguide. The present chapter is dedicated to the presentation of the properties of waves propagating in such structures, as guided waves and their study represent the core of the study of the present Thesis.

2.1 MHD waves

Presenting the linear wave solutions of the MHD equations will provide some understanding of the various waves and oscillations that are constantly observed in the solar atmosphere. The governing equations we are going to use will neglect a series of important ingredients, yet, will provide the necessary framework for a proper description of the properties of MHD waves. Therefore, we assume waves have wavelengths that are much longer than gravitational scale heights (we neglect gravitational effects), the plasma is perfectly conducting (we neglect electrical resistivity) and the length scales we operate are much longer than any characteristic lengths that are involved in transport mechanisms (we neglect viscosity and thermal conductivity). The last two simplifications also mean that the evolution of the physical system occurs such that the energy is conserved. As a result, the MHD equation can be written as

$$\frac{d\rho}{dt} + \rho\nabla.\mathbf{v} = 0, \tag{2.1}$$

$$\rho\frac{d\mathbf{v}}{dt} = -\nabla p + \frac{1}{\mu}[(\nabla \times \mathbf{B}) \times \mathbf{B}], \tag{2.2}$$

$$\frac{d}{dt}(p\rho^{-\gamma}) = 0, \tag{2.3}$$

$$\frac{\partial \mathbf{B}}{\partial t} = \nabla \times (\mathbf{v} \times \mathbf{B}), \tag{2.4}$$

$$\nabla \cdot \mathbf{B} = 0. \tag{2.5}$$

In the above equations ρ, p, $\mathbf{v}$, $\mathbf{B}$, μ, and γ are the density, pressure, velocity, magnetic field, permitivity of free space and adiabatic index, respectively, and

$$\frac{d}{dt} \equiv \frac{\partial}{\partial t} + \mathbf{v} \cdot \nabla \tag{2.6}$$

is the convective time derivative (Priest, 2014).

The first equation is the mass conservation equation that stipulates that the rate of mass flow out of a unit of volume is equal to the decreases of mass in the volume. Equation (2.2) is the momentum equation which describes the motion of a plasma element of unit volume and contains all forces that act on a given plasma element (the gradient pressure and Lorentz force). The energy equation (2.3) connects thermodynamics variables p and ρ, assuming there is no energy loss (or gain) in the system and the thermodynamical evaluation of the system can be described by an adiabatic process. Equation (2.4) is the induction equation which describes the interaction of the magnetic field with the flow velocity. Finally, equation (2.5) is the solenoidal condition and specifies that there are no magnetic monopoles in the system and that the magnetic fields lines are closed.

The above equations are highly nonlinear and their study is very difficult. Analytical progress can be achieved by assuming a linear approach (also known as linearisation) that considers that all physical variables have a small change around their equilibrium value. As a result, all physical quantities (f) will be written as $f = f_0 + f_1$, with $|f_1| \ll f_0$, where quantities with an index 0 are the equilibrium values and the quantities with an index 1 are their Eulerian perturbations. In addition, to simplify even more the problem, we assume that the equilibrium is homogeneous and stationary (equilibrium values do not depend on any coordinate and/or time) and the equilibrium is static, i.e. $\mathbf{v}_0 = 0$. As a result, the system of linearised MHD equations will contains terms that, at most, are products of an equilibrium quantity and a perturbation. With these simplifications the linearised MHD equations become

$$\frac{\partial \rho_1}{\partial t} + \rho_0(\nabla \cdot \mathbf{v}_1) = 0, \tag{2.7}$$

$$\rho_0 \frac{\partial \mathbf{v}_1}{\partial t} = -\nabla p_1 + \frac{1}{\mu}(\nabla \times \mathbf{B}_1) \times \mathbf{B}_0, \tag{2.8}$$

$$\frac{\partial p_1}{\partial t} - c_0^2 \frac{\partial \rho_1}{\partial t} = 0, \tag{2.9}$$

$$\frac{\partial \mathbf{B}_1}{\partial t} = \nabla \times (\mathbf{v}_1 \times \mathbf{B}_0), \tag{2.10}$$

$$\nabla \cdot \mathbf{B}_1 = 0, \tag{2.11}$$

where $c_0^2 = \gamma p_0/\rho_0$ is the sound speed.

The above system of equation can be reduced to a single partial differential equation by differentiating Equation (2.8) with respect to time, and using Equations (2.7) to (2.11) as

$$\frac{\partial^2 \mathbf{v}_1}{\partial t^2} = c_0^2 \nabla(\nabla \cdot \mathbf{v}_1) + \{\nabla \times [\nabla \times (\mathbf{v}_1 \times \mathbf{B}_0)]\} \times \frac{\mathbf{B}_0}{\mu\rho_0}. \tag{2.12}$$

Next, since we are looking for solutions that oscillate in time and space, we assume that the velocity can be written as

$$\mathbf{v}_1(\mathbf{r}, t) = \mathbf{v}_1 e^{i(\mathbf{k}\cdot\mathbf{r} - \omega t)}. \tag{2.13}$$

where $\mathbf{k} = (k_x, k_y, k_z)$ is the wavevector, $\mathbf{r}$ are the three coordinates and ω is the frequency (in the absence of dissipative effects, here assumed a real quantity). In the light of the above ansatz, the derivative operators transform into $\nabla \to i\mathbf{k}$ and $\partial/\partial t \to -i\omega$. As a result, Equation (2.12) becomes

$$\omega^2 \mathbf{v}_1 = c_0^2 \mathbf{k}(\mathbf{k} \cdot \mathbf{v}_1) + \{\mathbf{k} \times [\mathbf{k} \times (\mathbf{v}_1 \times \mathbf{B}_0)]\} \times \frac{\mathbf{B}_0}{\mu\rho_0}. \tag{2.14}$$

The solutions of this equation can be discussed in a few limiting cases, that can reveal the properties of MHD waves propagating in plasmas.

2.1.1 Alfvén waves

When the plasma is incompressible ($\nabla \cdot \mathbf{v}_1 = 0$) the dynamics is not affected by pressure forces and the only restoring force is the magnetic tension. In this case Equation (2.14) reduces to

$$\omega^2 \mathbf{v}_1 / v_{A_0}^2 = \{\mathbf{k} \times [\mathbf{k} \times (\mathbf{v}_1 \times \hat{\mathbf{B}}_0)]\} \times \hat{\mathbf{B}}_0, \tag{2.15}$$

where $v_{A_0} = B_0/\sqrt{\mu\rho_0}$ is the Alfvén speed and $\hat{\mathbf{B}}_0$ is the unit vector in the direction of $\mathbf{B}_0$, i.e. $\hat{\mathbf{B}}_0 = \mathbf{B}_0/B_0$. Using standard vector identities the above equation can be written as

$$\omega^2 \mathbf{v}_1 / v_{A_0}^2 = k^2 \cos^2\theta_B \mathbf{v}_1 - (\mathbf{k} \cdot \mathbf{v}_1) k \cos\theta_B \hat{\mathbf{B}}_0 + [(\mathbf{k} \cdot \mathbf{v}_1) - k \cos\theta_B (\hat{\mathbf{B}}_0 \cdot \mathbf{v}_1)]\mathbf{k}. \tag{2.16}$$

where $k = |\mathbf{k}|$ and θ_B is the angle between $\hat{\mathbf{B}}_0$ and $\mathbf{k}$.

In addition, by taking the scalar product of Equation (2.16) with $\hat{\mathbf{B}}_0$, we obtain that $\hat{\mathbf{B}}_0 \cdot \mathbf{v}_1 = 0$, which means that the perturbation of the velocity is perpendicular to the ambient magnetic field, so these waves are transversal.

Thus, for an incompressible plasma, the propagation vector will be perpendicular to the perturbed velocity ($\mathbf{k} \cdot \mathbf{v}_1 = 0$) and hence the dispersion relation of incompressible Alfvén wave is simply

$$\omega = \pm k \; v_{A_0} \; cos\theta_B. \tag{2.17}$$

Clearly Alfvén waves will have their maximum phase speed (ω/k) when they propagate along the magnetic field and they are not able to propagate in the perpendicular direction to the field ($\theta_B = \pi/2$) as shown in Friedrich polar diagram in Figure 2.1.

2.2 Magneto-acoustic waves

When changes in the plasma are opposed by the Lorentz force and the pressure gradient, then Equation (2.14) can be written as

$$\omega^2 \mathbf{v}_1 = k^2 v_{A_0}^2 \cos^2\theta_B \mathbf{v}_1 - (\mathbf{k} \cdot \mathbf{v}_1) v_{A_0}^2 k \cos\theta_B \hat{\mathbf{B}}_0 + [(v_{A_0}^2 + c_0^2)(\mathbf{k} \cdot \mathbf{v}_1) -$$

$$- k \cos\theta_B (\hat{\mathbf{B}}_0 \cdot \mathbf{v}_1)]\mathbf{k}. \tag{2.18}$$

By taking the scalar product of Equation (2.18) with $\hat{\mathbf{B}}_0$, we obtain

$$\frac{\hat{\mathbf{B}}_0 \cdot \mathbf{v}_1}{\mathbf{k} \cdot \mathbf{v}_1} = \frac{k \cos\theta_B c_0^2}{\omega^2}, \tag{2.19}$$

Next, after taking the scalar product of Equation (2.18) with $\mathbf{k}$, we obtain

$$\frac{\hat{\mathbf{B}}_0 \cdot \mathbf{v}_1}{\mathbf{k} \cdot \mathbf{v}_1} = \frac{-\omega^2 + k^2(v_{A_0}^2 + c_0^2)}{k^3 v_{A_0}^2 \cos\theta_B}. \tag{2.20}$$

After equalising the right-hand sides of the last two equations we obtain the dispersion relation of the *magneto-acoustic* waves in the form

$$\omega^4 - k^2\omega^2(c_0^2 + v_{A_0}^2) + k^4 c_0^2 v_{A_0}^2 \cos^2\theta_B = 0. \tag{2.21}$$

This fourth-order polynomial is bi-quadratic in ω, it describes two families

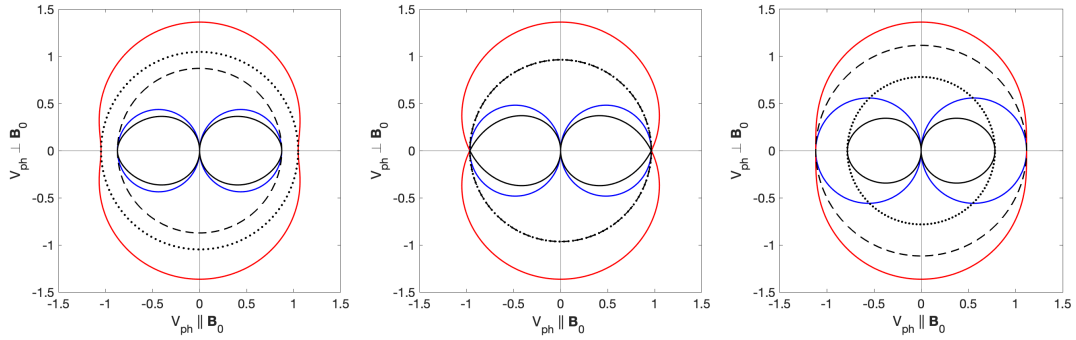

Figure 2.1: Polar (Friedrich) diagram showing the phase speed, v_{ph}, of Alfvén waves (blue solid lines), slow magneto-acoustic waves (black solid lines) and fast magneto-acoustic waves (red solid lines) under different regimes, $c_0 > v_{A_0}$ (left), $c_0 = v_{A_0}$ (middle) and $c_0 < v_{A_0}$ (right). The black dotted lines refer to the magnitude of c_0 and the black dashed lines refer to the magnitude of v_{A_0}. The equilibrium magnetic field $\mathbf{B}_0$ is in the horizontal direction.

of waves propagating in opposite direction, so

$$\frac{\omega^2}{k^2} = \frac{c_0^2 + v_{A_0}^2}{2} \pm \frac{1}{2}\sqrt{c_0^4 + v_{A_0}^4 - 2c_0^2 v_{A_0}^2 \cos 2\theta_B}. \tag{2.22}$$

The above dispersion relation describes fast and slow magneto-acoustic modes corresponding to the *plus* and *minus* signs, respectively. The phase speed, $v_{ph} = \omega/k$, of the fast magneto-acoustic waves extends from $max(c_0, v_{A_0})$ up to $(c_0^2 + v_{A_0}^2)^{1/2}$, while the phase speed of slow magneto-acoustic waves is in the range $0 \leq v_{ph} \leq min(c_0, v_{A_0})$. The phase speed of slow waves reaches its maximum value when propagating along the magnetic field and is equal c_{T_0} (called the tube speed) defined in Equation (2.25) (see, Roberts, 1981*a*).

A full picture of the properties of waves and their propagation speed can be obtained by plotting the variation of the phase speed in a polar diagram (also known as the Friedrich diagram). Here the ambient magnetic field, $\mathbf{B}_0$, points in the horizontal direction and the direction of the wavevector (basically the propagation direction of waves) covers a full 2π range. In Figure (2.1) we plot the phase speed of waves for three cases covering the possible ordering of the two characteristic speeds. It is clear from Figure(2.1) that the fast magneto-acoustic waves can propagate in the perpendicular direction to the magnetic field, whereas the slow magneto-acoustic and Alfvén waves cannot.

In reality the plasma is neither unbounded nor homogeneous. Waves often propagate along well-defined magnetic structures that will confer the medium some spatial rendering. That is why it is natural to extend our analysis and consider the case where the plasma is inhomogeneous via the simplest config-

uration represented by a sharp transition or discontinuity. The discontinuity can be described by an interface separating region with different properties. In particular, we will study the case of a single magnetic interface, the magnetic slab (that can be considered as a system of two interfaces separated by a constant width) and the magnetic flux tube that can be seen as a single curved interface. For all cases we present here the method of finding the dispersion relation consists of solving the MHD equations for the regions on both sides of the interface and join the solutions at the boundary using kinematic and dynamic boundary conditions.

2.2.1 Waves at a single magnetic interface

The simplest configuration that allows the study of guided waves is the problem of waves propagating along a sharp discontinuity separating two semi-infinite regions of different properties. High resolution observations show that there are several places in the solar atmosphere where the plasma structuring can be modelled as an interface, e.g. the boundary of the coronal holes and the edge of sunspots. For simplicity we consider an interface where the magnetic field changes discontinuously and the field is parallel to the interface separating the two regions (with such particular configuration we model a tangential discontinuity), each with its own set of parameters.

The effect of compressibility on the propagation of surface waves at a single interface was investigated by Wentzel (1979). He derived the dispersion relation for an isothermal disturbance. A proper investigation on the nature and properties of waves such interface supports was carried out later by Roberts (1981*a*), who showed that there are two surface waves that could propagate on single magnetic interface.

The analytical method used to derive the dispersion relation for this tangential discontinuity is similar to the method used to study surface waves in hydrodynamics. The stability of the interface requires that the total pressure (plasma pressure and magnetic pressure), and the perpendicular velocity components are continuous at the interface. In addition we assume that the perturbations will be localised to the interface, so waves will be evanescent far away from the interface. Similar conditions will be used in the following two sections to derive the dispersion relation in magnetic slab and magnetic flux tube.

Using the linearised and ideal MHD equations for a homonenous plasma,

the dispersion relation can be given as (Wentzel, 1979; Roberts, 1981*a*)

$$\rho_0(k_z^2 v_{A_0}^2 - \omega^2)(m_e^2 + k_y^2)^{1/2} + \rho_e(k_z^2 v_{A_e}^2 - \omega^2)(m_0^2 + k_y^2)^{1/2} = 0 \tag{2.23}$$

where subscripts 0 and e refer to the two different side of the discontinuity and m_0^2 and m_e^2 are the radial wavenumber defined as

$$m_0^2 = \frac{(k_z^2 c_0^2 - \omega^2)(k_z^2 v_{A_0}^2 - \omega^2)}{(c_0^2 + v_{A_0}^2)(k_z^2 c_{T_0}^2 - \omega^2)}, \quad \text{and} \quad m_e^2 = \frac{(k_z^2 c_e^2 - \omega^2)(k_z^2 v_{A_e}^2 - \omega^2)}{(c_e^2 + v_{A_e}^2)(k_z^2 c_{T_e}^2 - \omega^2)}. \tag{2.24}$$

In the above equations k_z and k_y are the wavenumber components along the z and y axis, and

$$c_{T_0} = \frac{v_{A_0} c_0}{\sqrt{v_{A_0}^2 + c_0^2}}, \qquad c_{T_e} = \frac{v_{A_e} c_e}{\sqrt{v_{A_e}^2 + c_e^2}} \tag{2.25}$$

are the tube speeds on both sides of the interface.

Following the analysis by Roberts (1981*a*), it can be shown that the phase speed of the surface waves (ω/k_z) is between v_{A_0} and v_{A_e} and the single magnetic interface supports the propagation of slow and fast magneto-acoustic modes. However the slow surface wave will be able to propagate only if one of the sides is field-free. The phase speed of the slow mode will be smaller than the tube speed, c_{T_0}. In contrast, the fast surface wave will propagate if the field-free region is hotter than the other side of the interface, hence c_e is greeter than c_0 and the phase speed will be in the range $c_0 \leq v_{ph} \leq min(c_e, v_{A_0})$.

As a natural extension of waves at a single interface is the problem is of two interfaces that now form a waveguide that could model the wave propagation in flux tube or loops. It is well known that waves propagating in a geometrically well-defined structure, become dipsersive, i.e, their phase velocity depends on the wavelength.

There are two distinctive approaches to the problem of guided waves that are mathematically tractable. First we consider waves propagating in a magnetic slab described in Cartesian geometry. The second one is the waves propagating in a magnetic flux tube that assumes a cylindrical geometry. Let us discuss these two approaches and compare the predictions of these models, what the dispersion relations are, how the dispersion curves vary in terms of the wavelength (or wavenumber) and what oscillatory pattern we can recover in these structures. Later, the cylindrical model will be expanded to consider waves in a waveguide of elliptical cross-section.

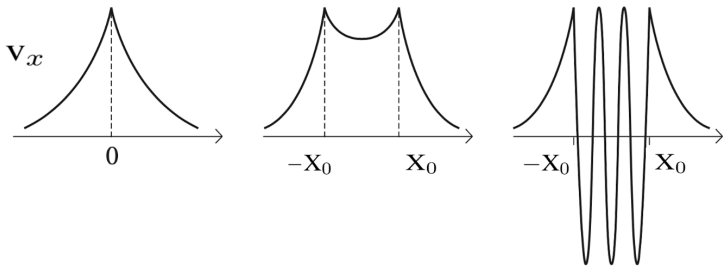

Figure 2.2: This figure shows the profile of the speed amplitude for a surface wave on (left panel) an interface and (middle panel) a slab or a flux tube. (right panel) A body wave on a slab or flux tube. Credit: Priest (2014)

2.2.2 Waves in a magnetic slab

One of the simplest ways to construct a waveguide and study the properties of guided waves is to consider that waves are propagating in an infinite channel of given width. For simplicity we assume that the plasma is structured by two interfaces, infinitely extended in the y and z direction, while it has a width $2x_0$ in the x direction. The problem of MHD waves propagating in these structures is well studied. Parker (1974) described the appearance of surface waves for an incompressible medium in an isolated magnetic slab and he found that the propagation speed of surface waves is less than the local Alfvén speed. A detailed discussion of waves propagating in a magnetic and compressible plasma in a magnetic slab was provided by Roberts (1981*b*). Later, this study was extended by Edwin and Roberts (1982) to include the magnetic field surrounding the slab, a limit that is more appropriate to solar physics. They consider a magnetic slab of width $2x_0$, permeated by a homogeneous internal (B_0) and external magnetic field (B_e), both parallel to the symmetry axis of the slab as shown in the left panel of Figure 2.3. Employing a set of boundary conditions at the two interfaces similar to the one presented in the earlier section, Edwin and Roberts (1982) derived the dispersion relation that governs the wave propagation in a magnetic slab in a magnetic environment. Since the problem deals with two interfaces, a clear distinction must be made between symmetric or kink modes (when the two boundaries oscillate in phase) and anti-symmetric or sausage modes (when the two boundaries oscillate in anti-phase), as shown in the middle and the right panels of Figure 2.3. Following straightforward and standard mathematical steps, the continuity of the total pressure and transversal velocity components leads to the dispersion relations

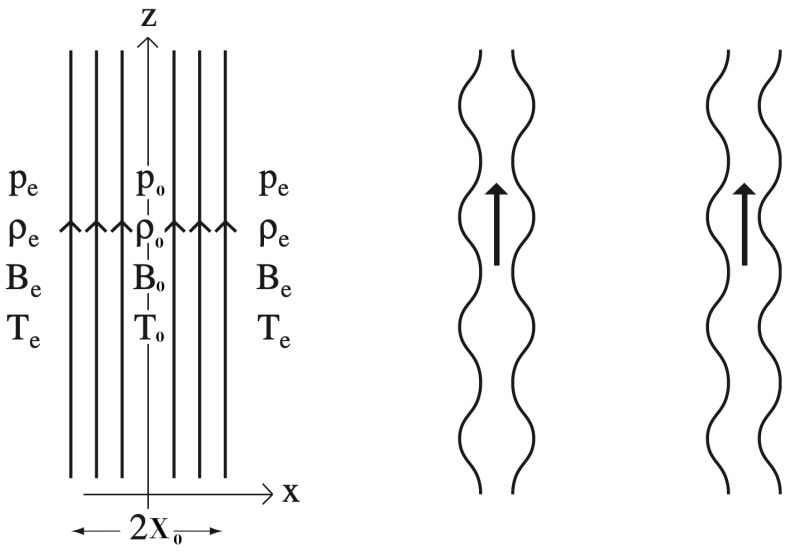

Figure 2.3: The left panel shows a sketch of a uniform magnetic slab surrounded by a uniform medium. The middle panel shows the sausage mode disturbance travelling along the slab (the vertical direction), where the right panel shows the kink mode. Credit: Priest (2014)

given by

$$\rho_e(k^2 v_{A_e}^2 - \omega^2)m_0 \tanh(m_0 x_0) + \rho_0(k^2 v_{A_0}^2 - \omega^2)m_e = 0 \tag{2.26}$$

for sausage modes, and

$$\rho_e(k^2 v_{A_e}^2 - \omega^2)m_0 \coth(m_0 x_0) + \rho_0(k^2 v_{A_0}^2 - \omega^2)m_e = 0 \tag{2.27}$$

for kink modes. The subscripts 0 and e refer to quantities inside and outside the slab. The magneto-acoustic parameters m_0 and m_e were defined earlier (see (2.24)), and m_e^2 is assumed to be positive in order to assure evanescence far away from the boundary of the waveguide.

The plasma-β parameter tells us whether the plasma dynamics is controlled by thermodynamics forces (∇p) or magnetic forces $\Big((\nabla \times \mathbf{B}) \times \mathbf{B}/\mu\Big)$. In the solar atmosphere, plasma-β is changing from being much larger than 1 in the photosphere, to much less than 1 in the corona. Waves can also be categorised depending on the sign of m_0^2. Waves that correspond to $m_0^2 > 0$ are the so-called surface waves whose maximum amplitude is attained at the boundaries of the waveguide and are evanescent inside the slab. On the contrary, when $m_0^2 < 0$ body waves can propagate along the slab and these waves have an oscillatory pattern inside the slab and their maximum occurs inside the slab.

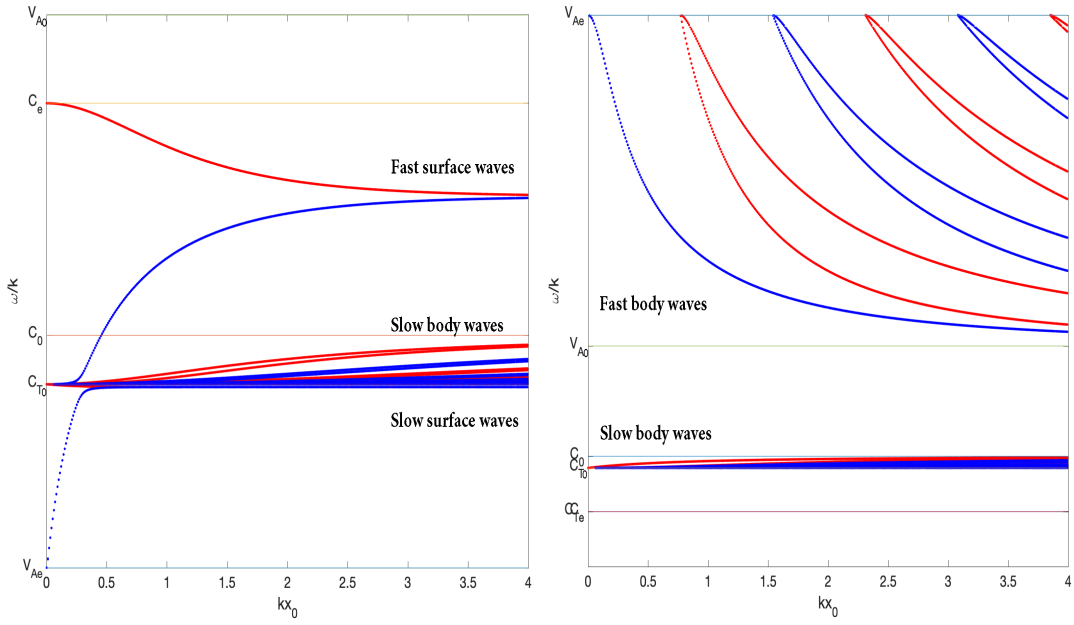

Figure 2.4: The left panel shows the solutions of the dispersion relations for a magnetic slab under photospheric conditions (i.e. $v_{A_0} > c_e > c_0 > c_{Ae}$), with $v_{Ae} = 0.5c_0, c_e = 1.5c_0$ and $v_{A_0} = 2c_0$. The right panel shows the same as the left panel, however, the dispersion curves are plotted for a magnetic slab under coronal condition (i.e. $v_{Ae}, v_{A_0} > c_0, c_e$), with $v_{Ae} = 5c_0, v_{A_0} = 2c_0$ and $c_e = 0.5c_0$. The red and blue dotted lines denote the sausage and kink modes, respectively.

Figure 2.4 shows the variation of the phase speed of waves under photospheric (left panel) and coronal (right panel) conditions in terms of the dimensionless quantity kx_0. Both panels show two families of modes (slow and fast magneto-acoustic). While the slow waves, with phase speeds close to the internal tube speed, c_{T_0}, show rather little variation with kx_0, fast modes have a much pronounced variation with kx_0.

First of all it is clear that since the phase speed of waves vary with k (or its inverse, the wavelength), waves are dispersive. Under coronal conditions (plasma-$\beta \ll 1$) the magnetic slab supports the propagation of only fast and slow body waves, while surface waves cannot propagate. In contrast, under the photospheric conditions (plasma-$\beta \gg 1$), there are slow and fast waves which could be body or surface waves depending on the sign of m_0^2. Fast magneto-acoustic waves propagate at a speed greater than $min(c_0, c_e)$ and $min(v_{A_0}, v_{A_e})$ and slow waves propagate with a phase speed lower than $min(c_0, c_e)$ or $min(v_{A_0}, v_{A_e})$ (Aschwanden, 2006). The phase speed of the slow body and kink waves is almost identical, regardless whether we are studying waves in the photosphere of solar corona. In contrast, fast waves show a much

stronger dispersion and have a much larger variation with the dimensionless parameter kx_0.

2.2.3 Waves in magnetic flux tubes

In reality, it is much more relevant to model the magnetic flux tube with a cylinder. Let us consider a magnetic cylinder described by the cylindrical coordinates (r, θ, z) permeated by a homogeneous and unidirectional magnetic field along the symmetry axis of the structure as shown in Figure 2.5. Edwin and Roberts (1983) extended their study in magnetic slabs (Edwin and Roberts, 1982) to consider the propagation of magneto-acoustic waves in a magnetic cylinder of constant radius a. The plasma dynamics is described by

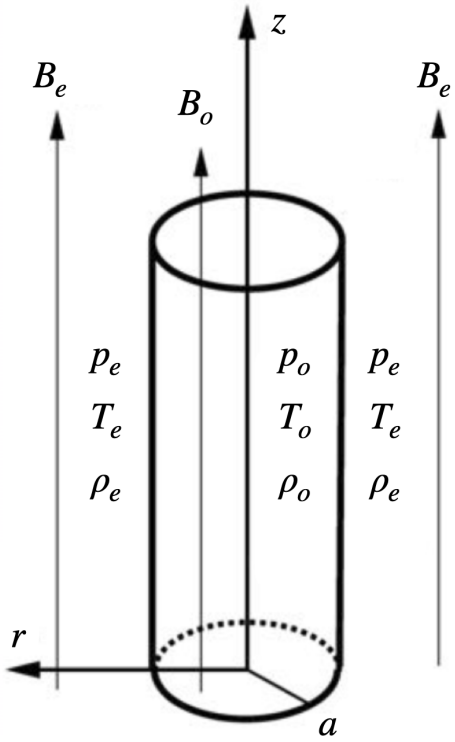

Figure 2.5: A sketch of a uniform magnetic cylinder surrounded by a uniform medium

the linear system of equations (see Equations 2.1-2.5) that can be combined into (Lighthill, 1960; Roberts, 1981*a*; Spruit, 1982)

$$\frac{\partial^4 \Delta}{\partial t^4} - (c_0^2 + v_{A_0}^2)\frac{\partial^2}{\partial t^2}\nabla^2\Delta + c_0^2 v_{A_0}^2 \frac{\partial^2}{\partial z^2}\nabla^2\Delta = 0, \tag{2.28}$$

where $\Delta = \nabla \cdot \mathbf{v}$. The solution of Equation (2.28), is on the form

$$\Delta = R(r)e^{i(\omega t + n\theta + k_z z)}, \tag{2.29}$$

where k_z and n are the longitudinal and azimuthal wave numbers, respectively. Hence, by substituting Equation (2.29) into (2.28), we obtain that the r-dependent amplitude of Δ is described by the Bessel differential equation

$$\frac{d^2R}{dr^2} + \frac{1}{r}\frac{dR}{dr} - \left(m_0^2 + \frac{n^2}{r}\right)R = 0 \tag{2.30}$$

where the magneto-acoustic parameter, m_0^2, has been defined earlier. The solution of the above differential equation is a Bessel (or modified Bessel) function of order n, depending on the sign of m_0^2.

By substituting Equation (2.29) into Equations (2.7) (2.11), the perturbed variables can be expressed as (see. Spruit, 1982)

$$v_r = \frac{\omega^2 - k_z^2 c_0^2}{\omega^2 m_0^2}\frac{d}{dr}\Re_n, \quad v_\theta = i\frac{\omega^2 - k_z^2 c_0^2}{\omega^2 m_0^2}\frac{n}{a}\Re_n, \quad v_z = -i\frac{c_0^2}{\omega^2}k_z\Re_n$$

$$b_r = -B_0\frac{k_z}{\omega}v_r, \quad b_\theta = B_0\frac{k_z}{\omega}v_\theta, \quad b_z = -iB_0\frac{\omega^2 - k_z^2c_0^2}{\omega^2}\Re_n$$

$$p_1 = i\rho_0\frac{c_0^2}{\omega}\Re_n \tag{2.31}$$

In the above relations, v_r, v_θ and v_z are the three components of the velocity perturbation, b_r, b_θ and b_z are the components of the magnetic field perturbation, p_1 is the pressure perturbation, m_0 is defined in Equation (2.24) and $\Re_n$ denotes the Bessel function of order n.

Therefore, the general solution in the internal region of the magnetic flux tube ($r < a$) can be given as

$$\Re_n = A_0 \begin{cases} I_n(m_0 r), & m_0^2 > 0 \\ J_n(n_0 r), & n_0^2 = -m_0^2 > 0. \end{cases} \tag{2.32}$$

Similarly, in the external region of the magnetic flux tube ($r > a$), the general solution is taken as

$$\Re_n = A_e K_n(m_e r), \quad m_e^2 > 0. \tag{2.33}$$

In the above equations A_0 and A_e are constants that will be determined with the help of boundary conditions, K_n, I_n and J_n are Bessel functions of order n and m_e is defined in Equation (2.24).

Since we are dealing with a tangential discontinuity, the continuity conditions at the cylinder boundary ($r = a$) have to written for the perpendicular velocity component and total pressure as

$$v_r(a) = v_{r_e}(a) \quad \text{and} \quad P_{1_e} + \frac{1}{4\pi} B_{0_e} b_{z_e} = P_1 + \frac{1}{4\pi} B_0 b_z,$$

The dispersion relation of linear compressional magneto-acoustic waves propagating along a magnetic cylinder has been derived by Edwin and Roberts (1983) and it reads

$$\rho_0 (k_z^2 v_{A_0}^2 - \omega^2) m_e \frac{K_n'(m_e a)}{K_n(m_e a)} - \rho_e (k_z^2 v_{A_e}^2 - \omega^2) m_0 \frac{I_n'(m_0 a)}{I_n(m_0 a)} = 0, \tag{2.34}$$

for surface waves ($m_0^2 > 0$), and

$$\rho_0 (k_z^2 v_{A_0}^2 - \omega^2) m_e \frac{K_n'(m_e a)}{K_n(m_e a)} - \rho_e (k_z^2 v_{A_e}^2 - \omega^2) n_0 \frac{J_n'(n_0 a)}{J_n(n_0 a)} = 0, \tag{2.35}$$

for body waves with $n_0^2 = -m_0^2 < 0$. As before the subscripts 0 and e refer to quantities inside and outside the cylinder. The dash refers to the derivative of the Bessel functions with respect to their argument.

The solutions of the dispersion relations for photospheric conditions are shown in Figure 2.6. A magnetic flux tube can support fast and slow kink surface waves (Edwin and Roberts, 1983). Furthermore, the slow kink surface mode propagates at speed close to c_{T_0}. In contrast, the fast kink surface mode has phase-speed closed to c_K, where

$$c_K = \sqrt{\frac{\rho_0 v_{A_0}^2 + \rho_e v_{A_e}^2}{\rho_0 + \rho_e}}, \tag{2.36}$$

and it can be regarded as a density-weighted Alfvén speed. The analysis of the dispersion curves also shows that sausage surface modes can propagate in a magnetic cylinder when plasma-$\beta \gg 1$, where the fast mode propagates with a phase speed between c_e and c_0 and the slow mode propagates with a phase speed very close to the slow kink surface mode.

The solutions of the dispersion relations for coronal conditions ($v_{A_0} \gg c_0$) are shown in Figure 2.7. In this case the magnetic flux tube supports the propagation of fast and slow kink and sausage body modes. The fast modes will propagate with a phase speed that is between the two Alfvén speeds, whereas the slow mode has a phase-speed between c_0 and c_{T_0}. Moreover, the

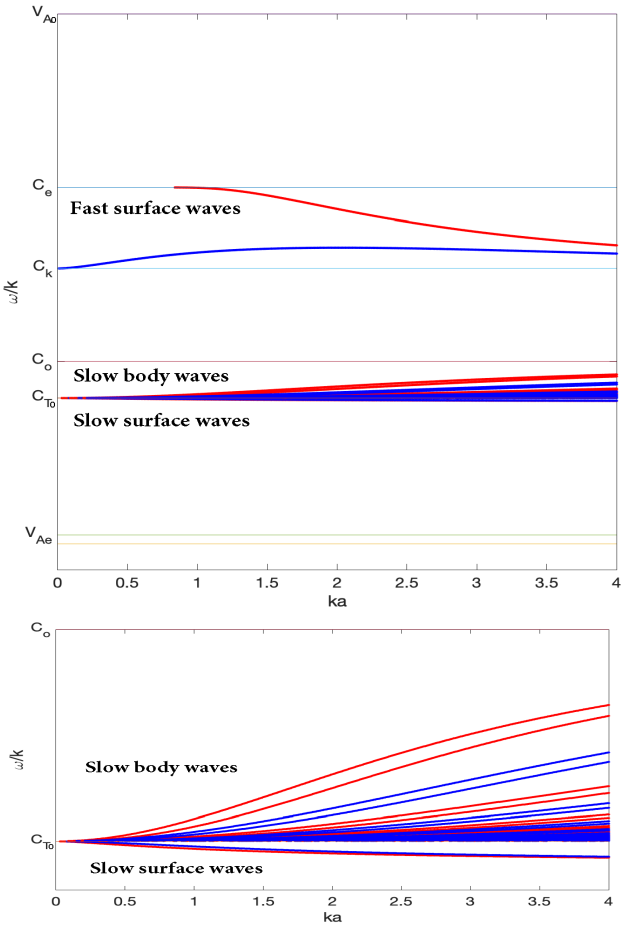

Figure 2.6: The dispersion relations for a magnetic cylinder under photospheric condition (i.e. $v_{Ae} = 0.5c_0, c_e = 1.5c_0$ and $v_{A_0} = 2c_0$). The lower panel is the zoom-in of the slow waves, and the red and blue dotted lines refer to the sausage mode and kink modes, respectively.

fast mode is dispersive, whereas the slow mode will disperse weakly as c_0 is almost equal to c_{T_0}. Finally, magnetic waveguides under coronal conditions do not support the propagation of surface waves.

MHD modes are classified according to their motion with respect to the longitudinal symmetry axis of the waveguide. Sausage modes ($n = 0$) propagate without perturbing the symmetry axis, i.e. they appear as stretching and squeezing oscillations of the magnetic field. Kink modes ($n = 1$) are characterized by a displacement of the symmetry axis of the magnetic flux tube, i.e. they perturb the symmetry axis in a back and forth motion (see Figure 2.8). Finally, fluting modes ($n \geq 2$) have a complex way of perturbing the axis. Although sausage and kink modes are often detected in solar magnetic structures (and their literature is extensive), the higher-order modes (the fluting modes) have eluded researchers.

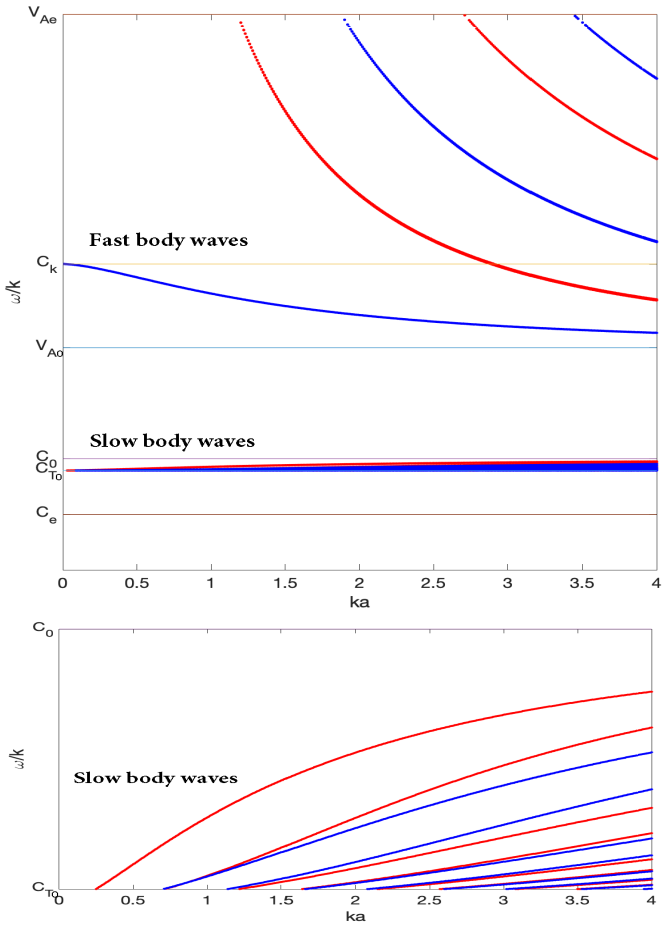

Figure 2.7: The dispersion curves for waves propagating in a magnetic cylinder under coronal conditions (i.e. $v_{Ae} = 5c_0, v_{A_0} = 2c_0$ and $c_e = 0.5c_0$). The lower panel is the zoom-in of the slow wave branch, and the red and blue dotted lines refer to the sausage and kink modes, respectively.

2.2.3.1 MHD wave modes in cylindrical magnetic flux tubes

The number of nodes in the radial direction (fundamental or overtone), the radial structure (surface or body), and the relative propagation speed (slow and fast magneto-acoustic modes, Alfvén or intermediate modes) are all used to classify the propagation of MHD waves.

Body waves exhibit an oscillating pattern in the radial direction within the waveguide and their lowest amplitude is near the waveguide's border. Body waves are likewise evanescent in the external environment (the wave power is localised and it is concentrated within the waveguide). In contrast, surface waves propagate such that they reach their maximum amplitude at the boundary of the waveguide and are evanescent both within and outside the magnetic flux tube.

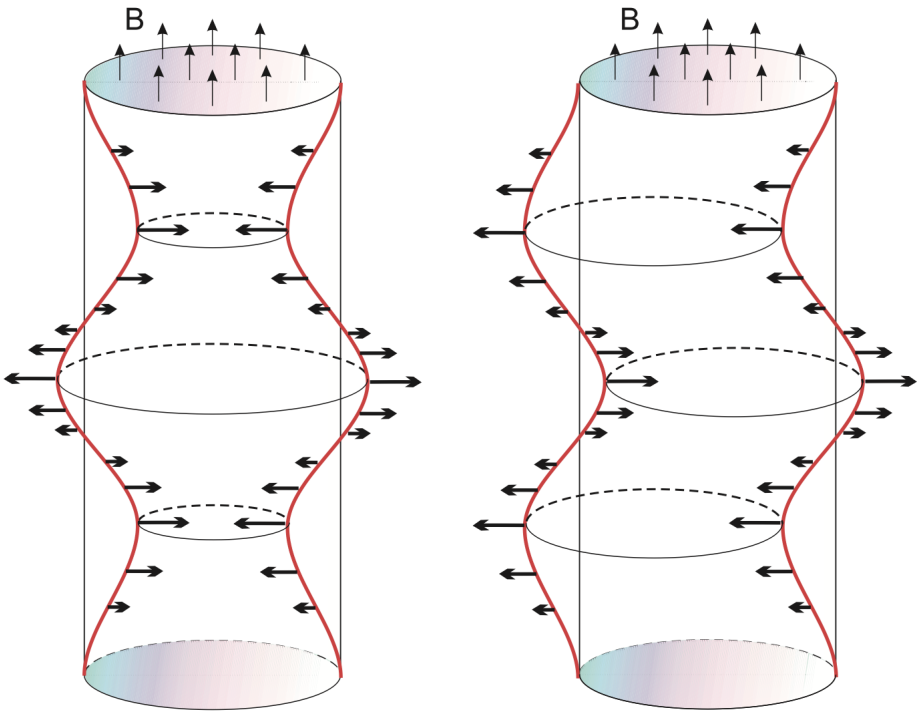

Figure 2.8: The oscillations of a cylindrical magnetic waveguide in the case a longitudinally propagating sausage (left panel) and kink mode (right panel), respectively. The sausage mode is stretching and squeezing the boundary of cylinder. In contrast, the kink mode is displacing the symmetry axis, as shown by the red solid line. The thin upward arrows indicate the direction of the background magnetic field, and the thick side-way arrows indicate the velocity amplitudes. Credit: Morton et al. (2012)

The slow mode propagate mostly along magnetic field lines, and they are prohibited from travelling in the perpendicular direction that corresponds to the radial direction. Fast modes are propagating in any direction and have their maximum speed when they are propagating in the perpendicular direction of the tube as they propagates with the phase speed $v_{ph} = \sqrt{c_0^2 + v_{A_0}^2}$ as shown in Figure 2.1.

By using the continuity Equation (2.1) and the perturbed velocity components (given by Equation 2.31), we have determined numerically the values of the density and the velocity perturbation for the sausage ($n = 0$), kink ($n = 1$) and fluting ($n = 2$) modes respectively. We have also matched the solutions at the boundary of the tube to evidence the motion of the plasma inside and outside the cylindrical flux tube. The variation of the radial velocity and the density perturbation (in kg/m^3) in the case of fast body and surface waves are displayed in Figures 2.9 and 2.10, respectively. The same quantities corresponding to slow body and surface waves are shown in Figures 2.11 and

2.12.

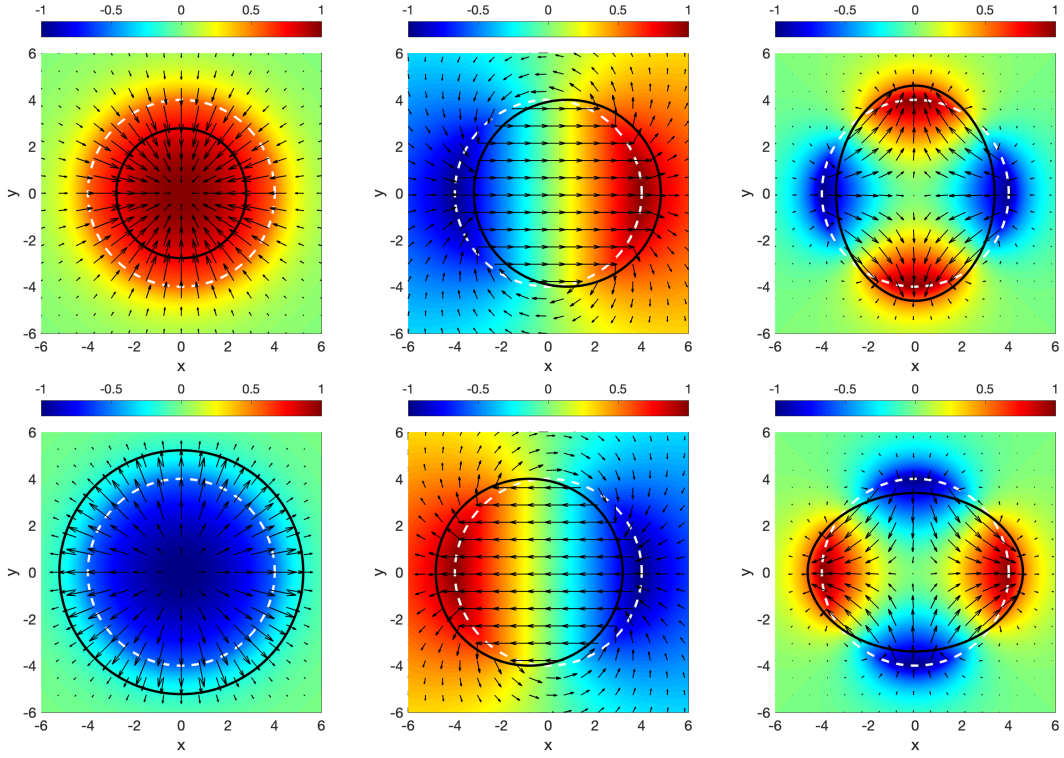

Figure 2.9: This figure shows the fast body waves for the radial velocity perturbation which is shown in black arrows, and the density perturbation (in kg/m^3) which is represented by the colorbar. The columns, from left to right, represent the quantities corresponding to sausage ($n = 0$), kink ($n = 1$) and fluting ($n = 2$) modes. The dashed white circle denote the boundary of the tube in the equilibrium state, and the black solid circle shows the new position of the tube's boundary during the perturbation. The images shown in the two rows are chosen to be in anti-phase, hence, they represent different time snapshots. The same configuration was used for Figures 2.10 to 2.13

Figures 2.9 to 2.12 clearly show that in the case of fast waves (for both body or surface waves), the amplitude of the radial velocity is the highest, while for the two slow waves the value of the radial velocity is lower. As a result, the tube boundary is more significantly affected in the case of fast waves, while there is no remarkable effect on the boundary in the case of slow waves. Furthermore, the fast and slow surface waves have their minimum amplitude of the density perturbation and the radial velocity at the center of the tube, while they have their maximum amplitude at the boundary of the tube. In contrast, the slow body wave have a their amplitude close to zero at the boundary of the tube.

The modes that we described and displayed in these figure are having one node along the radial direction, i.e. they are the so-called fundamental modes. If one considers more nodes in the radial direction, we recover the overtones

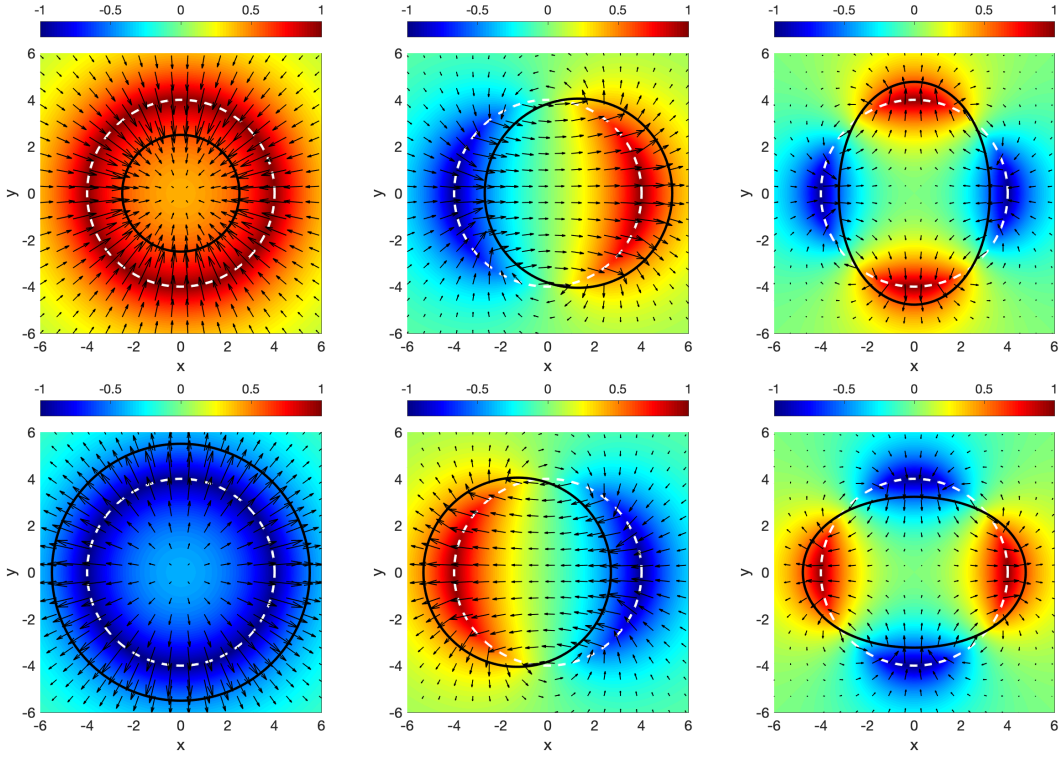

Figure 2.10: The same as Figure 2.9, but here we show the fast surface sausage ($n = 0$), kink ($n = 1$) and fluting ($n = 2$) modes.

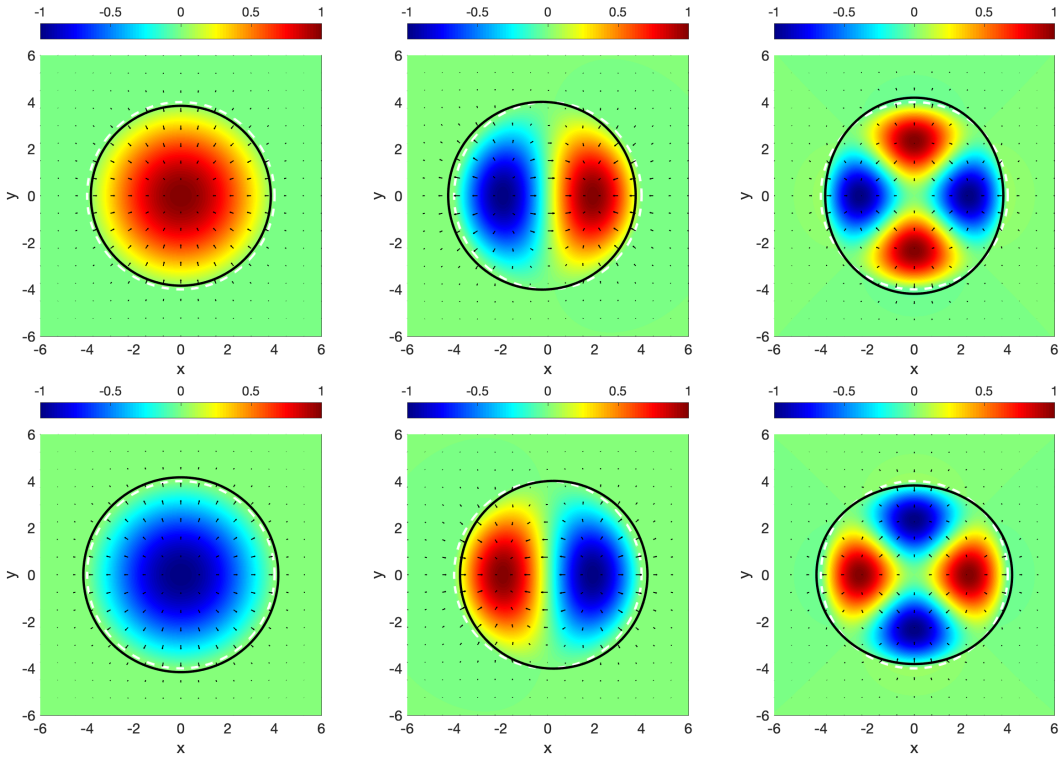

Figure 2.11: The same as Figure 2.9, but here we show the slow body sausage ($n = 0$), kink ($n = 1$) and fluting ($n = 2$) modes.

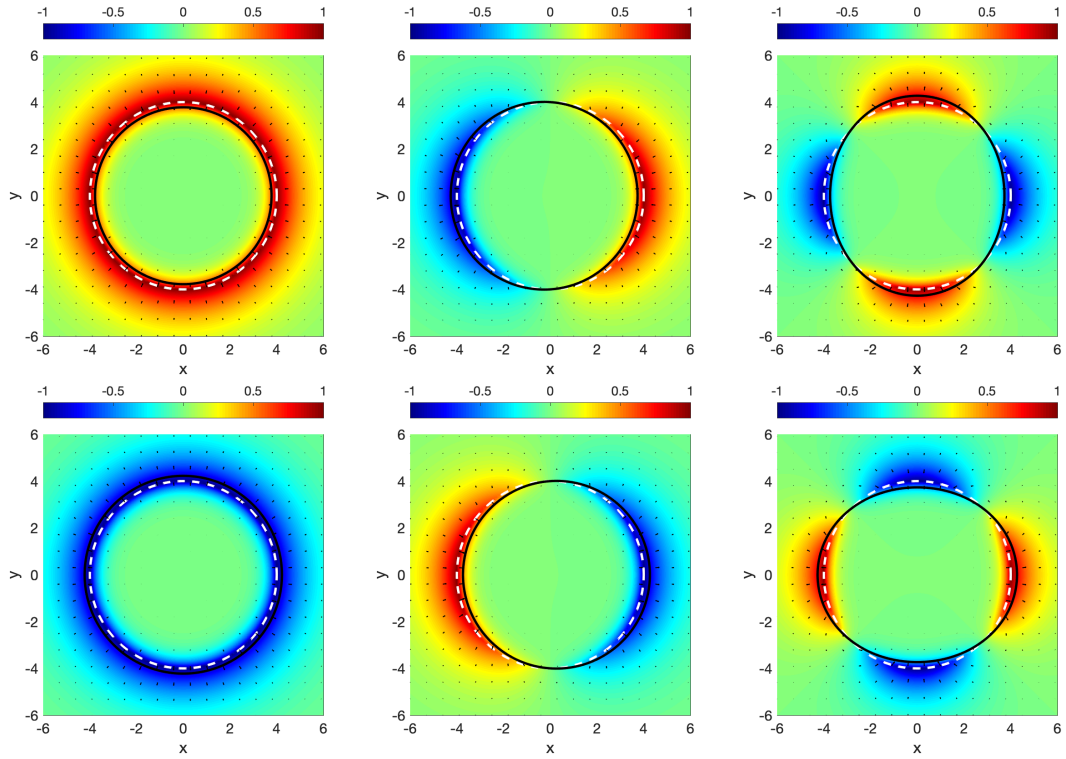

Figure 2.12: The same as Figure 2.9, but here we show the slow surface sausage ($n = 0$), kink ($n = 1$) and fluting ($n = 2$) modes.

of these modes. Our results confirm that body waves will have overtones (as shown in Figure 2.13). In contrast, surface waves do not possess overtones. That is obvious in the dispersion diagram (see Figures 2.6 and 2.7) that show that for a particular value of ka there is only one curve corresponding to surface waves, while in the case of body modes several curves are visible, each curve corresponding to a distinct number of radial nodes. Mathematically our findings are fully justified, as surface waves are described in terms of the Bessel function I_n (see Equation 2.34), which does not have an oscillatory pattern, instead these functions show a monotonic increase, similar to an exponential function. Body waves, however, are described in terms of the Bessel function J_n (see Equation 2.35), that has an oscillatory pattern.

2.2.4 Waves in magnetic flux tubes of elliptical cross section

The model describing the wave propagation in a cylindrical magnetic flux tube developed by Edwin and Roberts (1983) can be expanded to a more general case for studying the propagation of MHD waves in a magnetic waveguide with

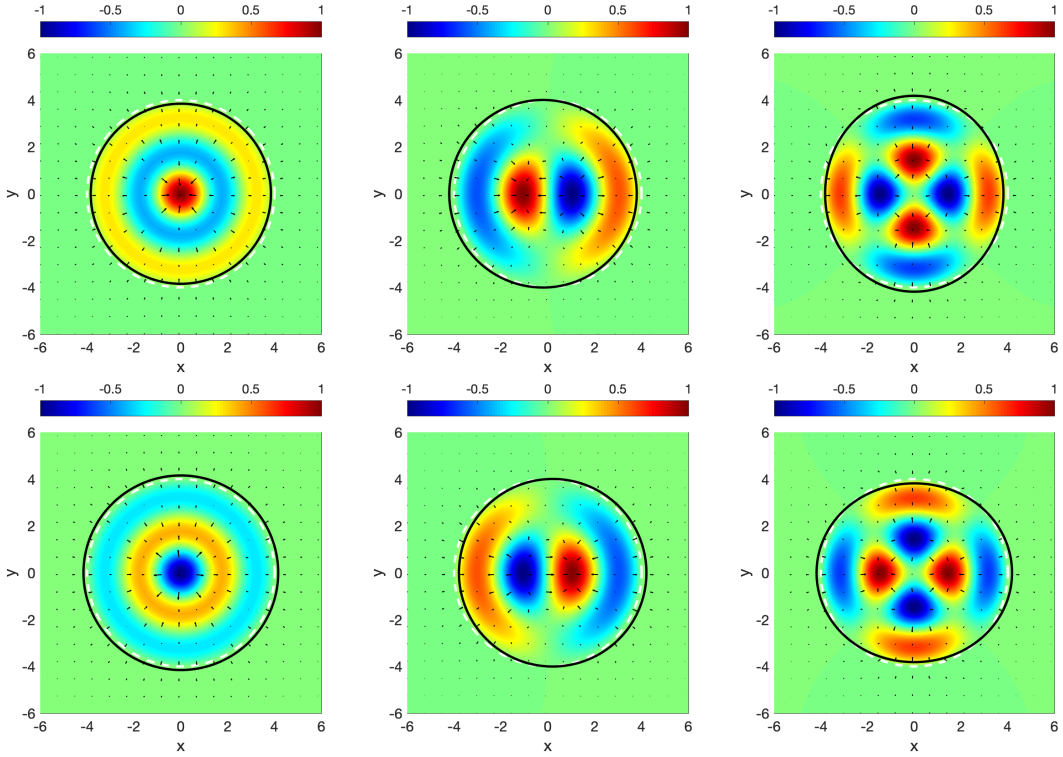

Figure 2.13: The same as Figure 2.9, but here we show the body waves with more than one radial node, i.e. the overtone modes, corresponding to the sausage ($n = 0$), kink ($n = 1$) and fluting ($n = 2$) modes.

an elliptical cross-section (see Aldhafeeri et al., 2021, for more details). In this configuration the dispersion equations for MHD surface and body waves can be represented as

$$\rho_e(k_z^2 v_{Ae}^2 - \omega^2)\frac{\Xi_m^{\prime E,O}(|\tilde{m}_0|, s_0)}{\Xi_m^{E,O}(|\tilde{m}_0|, s_0)} = \rho_0(k_z^2 v_{A_0}^2 - \omega^2)\frac{\Psi_m^{\prime E,O}(|\tilde{m}_e|, s_0)}{\Psi_m^{E,O}(|\tilde{m}_e|, s_0)}, \tag{2.37}$$

$$\rho_e(k_z^2 v_{Ae}^2 - \omega^2)\frac{\Theta_m^{\prime E,O}(\tilde{m}_0, s_0)}{\Theta_m^{E,O}(\tilde{m}_0, s_0)} = \rho_0(k_z^2 v_{A_0}^2 - \omega^2)\frac{\Psi_m^{\prime E,O}(|\tilde{m}_e|, s_0)}{\Psi_m^{E,O}(|\tilde{m}_e|, s_0)}, \tag{2.38}$$

where the new magneto-acoustic parameters are

$$\tilde{m}_0^2 = -\frac{\sigma^2}{4}m_0^2, \quad \tilde{m}_e^2 = -\frac{\sigma^2}{4}m_e^2, \tag{2.39}$$

In the above equations the quantities m_0^2 and m_e^2 are the magneto-acoustic parameters defined earlier in Equation (2.24), σ is the distance from the center of the ellipse to its focal points and s_0 is the flux tube boundary, which is defined by the confocal ellipse. Although the form of dispersion relations (2.37) and (2.38) are rather similar to the case of a waveguide with circular

cross-section, the functions involved in these equations are Mathieu functions, rather than Bessel functions. In the above dispersion relations, $\Xi_m^{E,O}$, $\Theta_m^{E,O}$ and $\Psi_m^{E,O}$ denote the internal solution for body wave, the internal solution for surface wave and the external solution, respectively. The superscripts E and O denote the even and odd solutions and the prime denotes the derivative of the Mathieu function with respect to the confocal elliptic variable, s.

The study by Aldhafeeri et al. (2021) revealed that the higher order modes are strongly influenced by the change in the eccentricity of the waveguide. It was also found that the cross-sectional shape introduces significant changes in the behaviour of waves, as this depends on the polarisation along the major or the minor axis of the ellipse. Their study provided a comparison about the effect on the dispersion curves as the eccentricity (ϵ), defined as $\epsilon = 1/\cosh(s_0)$, increases, i.e. the main axis expands and the minor axis contracts, as shown in their dispersion curve in Figures 2.14 and 2.15. By comparing the dispersion curves of the elliptical flux tube with the cylindrical flux tube, which we have shown earlier in Figures 2.6 and 2.7, we can easily notice that the dispersion curve for the kink mode in the elliptical flux tube is divided into two curves, based on the polarisation direction of the wave. In the cylindrical model, given the rotational symmetry of the shape, such difference is not present.

The results by Aldhafeeri et al. (2021) also show that under coronal conditions (their Figure 2.15), with the increase of ϵ, the phase speed (v_{ph}) of the fast body modes varies depending on the mode's polarisation direction. They have also shown the kink mode with a polarisation along the main axis has a lower frequency compared to the mode propagating along the minor axis. For the slow body modes the opposite effect takes place, i.e. the phase speed of the modes that is polarised along the main axis is higher than the phase speed of the wave polarised along the minor axis (Aldhafeeri et al., 2021).

Moreover, the dispersion curve under photospheric condition is also effected as ϵ increases as shown in Figure 2.14. The study by Aldhafeeri et al. (2021) has shown that the photospheric slow body wave has the same behaviour as under the coronal condition. In contrast, fast surface waves have an opposite behaviour than fast body wave under coronal condition. The fast surface kink mode that is polarised along the main axis has higher frequency than that one polarised along the minor axis.

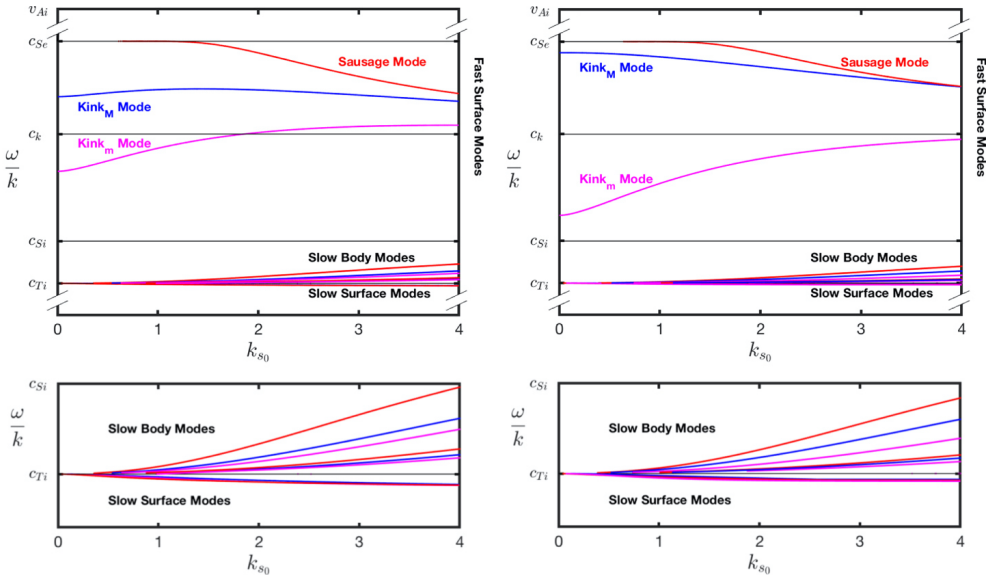

Figure 2.14: This figure shows the dispersion curves under the photospheric condition in a waveguide with elliptical cross-section. Every column represents the curves with a different value of eccentricity (ϵ) of the cross section of the magnetic flux tube. The left column corresponds to $\epsilon = 0.65$ ($s_0 = 0.99$), i.e. the cross section is a moderate ellipse. The right column shows the dispersion curves for waves in an elliptical waveguide with $\epsilon = 0.84$ ($s_0 = 0.60$). The bottom panels are showing a zoom-in of the region for slow waves. Here the red curves represent the sausage modes, and the blue curves represent the kink modes polarised along the major axis. The dispersion curve of kink modes polarised along the minor axis is represented by the magenta curve. Here v_{A_0} is the Alfvén speed, c_S is the sound speed and c_{T_0} is the tube speed. The quantities with index i and e refer to internal and external values, respectively. Credit: Aldhafeeri et al. (2021)

2.2.5 Waves in magnetic irregular cross-sectional flux tube

Observations show that in the reality the cross-section of sunspots is far from being regular. Comparing the solutions of the dispersion relations for regular circular and elliptical cross-sections reveal that the properties of waves and their dispersion curves are sensitive to the transversal geometry of the waveguide (Aldhafeeri et al., 2021). In order to determine the property of waves and their oscillatory patterns in waveguides with irregular cross-section a numerical approach was used to determine the eigenfunctions and the associated eigenvalues. For this problem, we do not assume any preferred geometrical shape of the umbra. Therefore, we used a Cartesian coordinate system, assuming the photospheric level to be the xy-plane and the vertical direction to be along the vertical z axis. The spatial structure of the eigenfunctions

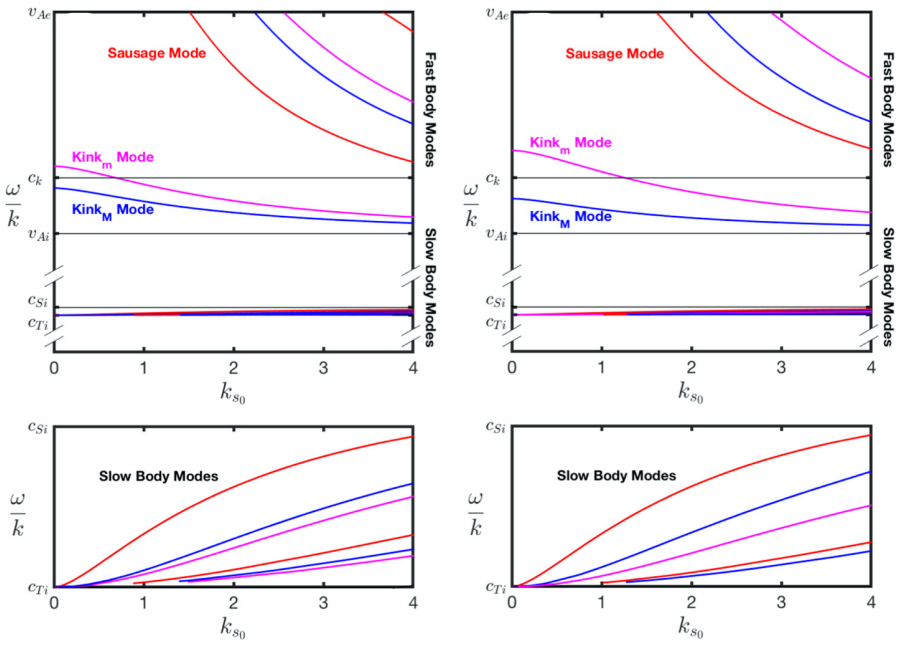

Figure 2.15: The same as Figure 2.14, but here the dispersion curves are plotted under the coronal condition. Credit: Aldhafeeri et al. (2021)

is physically constrained by the cross-sectional shape of the waveguide. The governing equation of the longitudinal velocity perturbation, v_z, was derived and solved by using the observed cross-sectional shape, where the shape is obtained by taking the threshold level of the umbral intensity and set $v_z = 0$ at the umbra/penumbra boundary to be consistent with the observational data (see, Stangalini et al., 2022).

By assuming linear MHD perturbations, the time-independent Helmholtz equation has been derived for the vertical component of velocity perturbation, v_z, of the form

$$\frac{\partial^2 v_z}{\partial x^2} + \frac{\partial^2 v_z}{\partial y^2} - m_0^2 v_z = 0, \tag{2.40}$$

where m_0^2 is the eigenvalue defined by Equation (2.24). Equation (2.40) was solved by assuming Dirichlet-type boundary condition, i.e. at the boundary of the magnetic waveguide the z-component of the velocity perturbation vanishes. With this type of boundary condition the numerical solution describes only slow body modes, which constitutes a limitation of this model. In order to apply the above approach to observations (line intensity), it is more convenient to write Eq. 2.40 in terms of density perturbation, ρ. The relationship between

the density and longitudinal velocity component is simply

$$v_z = \frac{k_z c_i^2}{\omega \rho_0} \rho, \tag{2.41}$$

where ρ_0 is the unperturbed density that corresponds to the equilibrium state (Aldhafeeri et al., 2021). It follows from Equation (2.41) that the evolution of the density perturbation is governed by a similar Helmholtz equation. In general, all the dominant compressive variables are proportional to each other, therefore they can be assumed to be governed by a Helmholtz-type equation.

In Figure 2.16, we show the slow body modes of the three different models of the flux tube that we have introduced in this chapter. It is remarkable, in the case of the fundamental modes (both, sausage and kink slow body modes), the change in the shape of the cross-section (from cylindrical, to elliptical and, finally, to an irregular shape) does not introduce significant changes in the spatial structure of the modes. However, the higher-order modes are affected by the change in the shape of the cross-section. Therefore, in chapter 5, we compare the observed modes from sunspots with these models to see which model has a good agreement with the observed modes.

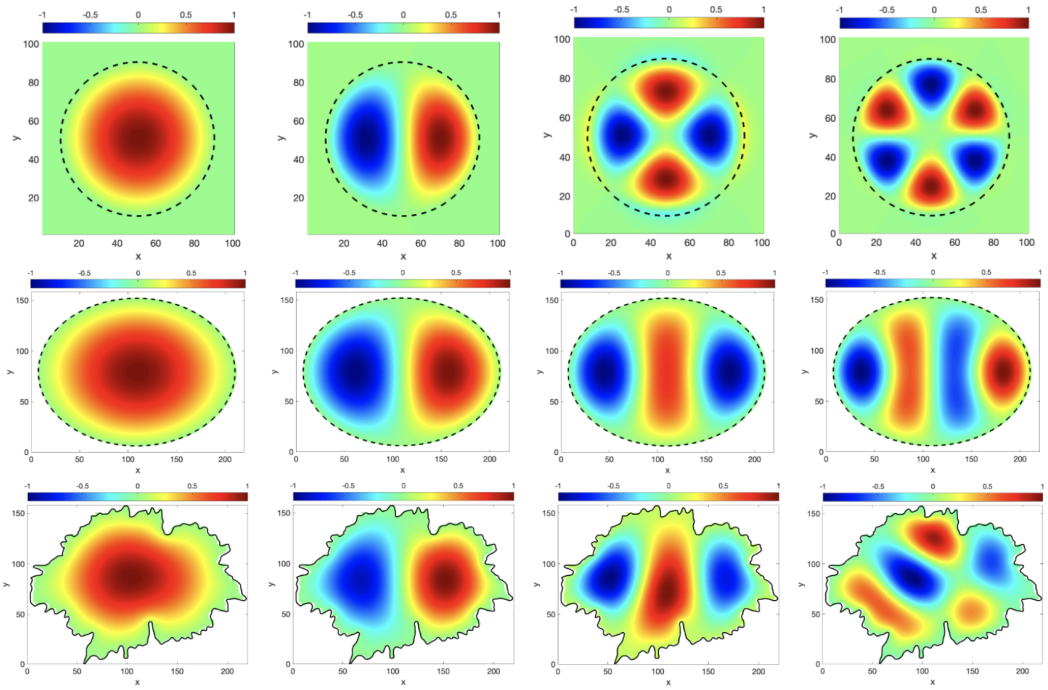

Figure 2.16: This figure shows the slow body modes in three different models of the cross-section shapes. The first row displays the modes in the cylindrical model (see section 2.2.3), the second row displays the modes in the elliptical model (see section 2.2.4) and the third row shows the modes in the model that corresponds to the realistic shape of the umbral boundary (see section 2.2.5). Whereas, the columns from left to right are displaying the fundamental sausage mode, the fundamental kink mode, the fluting mode ($n = 2$) and the fluting mode ($n = 3$). The colorbars display the density perturbation.

CHAPTER 3

Decomposition Techniques and an Application on a Numerical Simulation Data

Dynamics of natural systems are often complicated and strongly nonlinear, making comprehension challenging since the dynamics and complexity of systems are frequently entangled. There are situations when it is possible to recognise the dynamics of the system by using some nonlinear equations, which is a non-trivial process (e.g. the evolution of shocks and solitons, whose evolution in space and time are given by nonlinear partial differential equations that could be solved using various techniques). There has been a lot of effort invested over the last several decades to create data-driven algorithms for extracting spatial and temporal coherent features.

Sunspots are complex structures not only because they have an inhomogeneous density and magnetic field distribution, but also because the dynamics in these enormous magnetic features is driven by external mechanisms that are not visible. Sunspots are also structures whose transvesal shape in varying in time, affecting the nature and properties of waves. In order to resolve this complexity we applied the Proper Orthogonal Decomposition (POD) and Dynamic Mode Decomposition (DMD) techniques, whose combined diagnostic power will be used in the following chapters to detect the dominant MHD wave modes from solar sunspot datasets.

The POD technique determines spatially orthogonal patterns from time-series dataset. Similarly the DMD technique determines temporally orthogonal patterns from time-series dataset. The POD and DMD are frequently used in granular flows and fluid mechanics (Murray and Ukeiley, 2007; Berry et al., 2017; Higham et al., 2017; Higham and Brevis, 2018; Higham et al., 2020, 2021). In this chapter, we will present in details the POD and DMD techniques in sections 3.1 and 3.2 based on the description by Higham et al. (2018). In section 3.3, the synthetic data will be obtained by combining different MHD modes, which we discussed earlier in chapter 2. Then the POD and DMD will

be applied on the generated dataset to recover the modes individually. This step is considered as a test case to check whether the techniques are able to recover the MHD wave modes before applying them to real solar data.

3.1 Proper Orthogonal Decomposition (POD)

The POD technique has been known for more than a century since the pioneering work by Pearson (1901), who aimed to develop a technique to be a mechanical equivalent of the principal axis theorem. After that, Lumley (1967) developed POD as a mathematical approach in fluid dynamics for identifying coherent patterns in turbulent flow fields. POD is known by a number of names in the literature, depending on the area of application, e.g. principal component analysis (PCA) and Hotelling analysis. The POD approach enables spatially orthogonal patterns to be determined from signals, with number of modes equal the number of the snapshots of the time series. As a result, one of the most difficult aspects of this technique is determining which of the POD modes have a physical significance and their identification with the MHD modes in the umbral region of a sunspot. On the other hand, the POD will also provide straightforward ranking criteria based on the contribution of the modes to the signal's variation.

3.1.1 The mathematical algorithm of the POD

Consider a sequential dataset having a spatial dimension of $X \times Y$ in a time domain of size T, identified as the snapshots of our time series. Each of these snapshots is represented as a column in matrix $W \in \mathbb{R}^{N \times T}$, where $N = XY$. In the applications of higher-resolutions datasets on fluid dynamics and also on the upcoming applications in solar physics N is commonly much larger than T, i.e. $N \gg T$, which means that in the matrix W the number of rows is much higher than the number of columns. Each column of W will be defined as w_i with $i = 1...T$ such that

$$W = \{w_1, w_2, ...w_T\}. \tag{3.1}$$

There are three main approaches to perform POD on a dataset. The first one is the Spatial (Classical) POD method. It is performed by computing the eigenvalues and the eigenvectors of WW^T, where T is the transpose matrix. The eigenvectors will provide the POD mode, while the eigenvalues will provides the modes contribution. The second approach is the Method of Snap-

shots, which analyzing the smaller eigenvalue problem by by computing the eigenvalues and the eigenvectors of $W^T W$ (Sirovich, 1987). The third approach, which one that used in this Thesis, is to obtain the POD of W by using the optimum low rank approximation. This is known as the Singular Value Decomposition (SVD, Eckart and Young, 1936). The SVD can be applied to a rectangular matrix to find the left and right singular vectors. Applying the SVD on W, we obtain

$$W \equiv \Phi S C^*. \tag{3.2}$$

This output of decomposition in the above equation gives the spatial structure of each mode, where the POD modes are presented as columns of the matrix $\Phi \in \mathbb{R}^{N \times T}$, i.e. ϕ_i with $i = 1...T$ and these modes are orthogonal to each other. The size of every ϕ_i matrix is $N \times 1$, which means that they need to be reorganised to have same size as the original spatial domain, $(X \times Y)$ of original the dataset in order to display the spatial structure of the mode. The columns of the matrix $C \in \mathbb{R}^{T \times T}$ represent the temporal evolution of the POD modes. Hence, the product of the $X \times Y$ two-dimensional spatially orthogonal eigenfunctions and their corresponding one-dimensional time coefficients is the spatial and temporal output of the POD shown here. These modes can be periodic or non-periodic and their amplitude can also vary with time as the POD has no restriction on the time coefficients. Moreover, the left and the right singular vectors, Φ and C in Equation (3.2), are identical to the eigenvectors of WW^T and $W^T W$, respectively (Taira et al., 2017).

The POD modes have a clear ranking in terms of their contribution to the total variance of the snapshot series, and that ranking is given by the diagonal matrix $S \in \mathbb{R}^{T \times T}$, with the diagonal elements λ of the matrix S. The contribution to the total variance of each POD modes comes from the vector

$$\lambda = \frac{diag(S)^2}{N-1}. \tag{3.3}$$

3.2 Dynamic Mode Decomposition (DMD)

The DMD technique was initially used over a decade ago by Schmid (2010). The DMD a data-driven algorithm for extracting the dynamic information of a flow created by numerical simulations or a measurable physical experiment (Hemati et al., 2014). DMD is a widely used technique in the field of fluid mechanics, e.g. jet flows (Rowley et al., 2009; Jovanović et al., 2014), viscoelastic fluid flows (Grilli et al., 2013) and bluff body flows (Bagheri, 2013).

The DMD technique allows the determination of temporally orthogonal patterns of the signal with a pure frequency. Hence, the technique can extract information about the coherent spatial structure of observed MHD wave modes if the modes have distinct frequencies. The recovered DMD mode provides the spatial structure of the mode, while the corresponding eigenvalues provide information about the mode's oscillation frequency. However, the DMD does not provide any ranking of the modes in any way.

3.2.1 The mathematical algorithm of DMD

To apply the DMD approach, the time snapshots must be structured in columns in the same way as discussed earlier in the case of the POD (Section 3.1), but here we use two different matrices defined as

$$W^A = \{w_1, w_2, ...w_\tau\} \quad and \quad W^B = \{w_2, w_3, ...w_T\}. \tag{3.4}$$

Here $\tau = (T-1)$, and W^A is starting from the first column of W up to the last but one column of W and W^B starts from the second column up to the last column of W, i.e. W^B is shifted by a snapshot compared to W^A.

The matrices W^A and W^B are related by a linear operator $A \in \mathbb{C}^{N\times N}$ such that

$$W^B = AW^A. \tag{3.5}$$

The DMD is based on estimating the eigenvalues and eigenvectors of the linear operator A rather than calculating them precisely since A is very large for most practical applications. The estimating is based on reducing $A \in \mathbb{C}^{N\times N}$ to be $\tilde{A} \in \mathbb{C}^{T\times T}$ and then calculating the eigenvalues and eigenvectors of $\tilde{A}$. Therefore, the matrix W^A is decomposed using SVD as

$$W^A = \tilde{\Phi}\tilde{S}\tilde{C}^* \tag{3.6}$$

and substituted in Equation (3.5) to give

$$W^B = A\tilde{\Phi}\tilde{S}\tilde{C}^*, \tag{3.7}$$

and hence,

$$\tilde{\Phi}^* W^B \tilde{C}\tilde{S}^{-1} = \tilde{\Phi}^* A\tilde{\Phi}. \tag{3.8}$$

From this we define

$$\tilde{A} = \tilde{\Phi}^* A\tilde{\Phi}, \tag{3.9}$$

where $\tilde{A} \in \mathbb{C}^{\tau \times \tau}$ is the optimal low-dimensional representation of A, (note that $\tau \ll N$). Hence we can calculate the complex eigenvalues, μ_i, and associated eigenvectors, z_i, of $\tilde{A}$, where $i = 1...\tau$.

Now, the eigenvectors, z_i, of the reduced matrix $\tilde{A}$ will not have a size as the original spatial dimension. Therefore, according to Schmid (2010), a Vandermonde expansion of the complex eigenvalues is created to obtain a robust set of eigenvectors and that can be defined as

$$Q_{i,j} = \mu_i^{j-1}, \tag{3.10}$$

where $i = 1...\tau$ and $j = 1...\tau$. When this procedure is accomplished, the spatial structure of the DMD modes is acquired by forming

$$\Psi = W^A Q^*, \tag{3.11}$$

and the distinct frequencies (f_i) associated with each these modes (i) are

$$f_i = f_s \arg(z_i)/2\pi, \tag{3.12}$$

where f_s is the sampling frequency, the number of samples per second.

The DMD technique only provides the spatial structure of the modes with their associated frequency, and it does not provide a clear ranking of the modes. This creates a difficulty in distinguishing and identifying the modes and the power they have.

Therefore, by following the approach by Higham et al. (2018), modes are identified based on their contribution to the variance via POD. This step is followed by the calculation of a Fourier Power Spectra of the POD time coefficients associated with the dominant modes. The power spectrum is then used to determine the dominant frequency or frequencies, in case of intertwined modes, which is then used to identify the spatial structure associated to individual frequencies based on the DMD results. If there is no exact match between frequencies, the DMD modes closer to the target frequency are then selected.

Mode number	MHD wave type	Amplitude	Frequency [Hz]
1	Slow body sausage	1	0.05
2	Slow surface sausage	7	0.05
3	Fast surface kink	9	0.07
4	Slow body fluting ($n = 2$)	4	0.1
5	Slow surface fluting ($n = 3$)	3	0.15

Table 3.1: The modes that constitute the combined synthetic data for the validation of the POD and DMD techniques. The above information was collected from a simulation of waves in a theoretical cylindrical waveguide where the dispersion relations are given by Equations (2.34) and (2.35).

3.3 POD and DMD applied to a synthetic numerical dataset

Before we apply the POD and DMD techniques on an actual sunspot observation dataset, we will need to test the algorithms by applying them on a synthetic data that contains a combination of known MHD wave modes. In this section, we will generate an artificial dataset by combining several MHD wave modes and then apply the techniques of POD and DMD to see whether they are able to recover every single mode.

The synthetic dataset has been generated by combining five MHD wave modes recovered from the density perturbation collected from a cross cut in the cylindrical waveguide corresponding to a the theoretical model (see Section 2.2.3). The information about the selected modes are shown in Table 3.1, and the spatial structure of the selected modes are shown in Figure 3.1. The dataset has been taken over the course of 100 seconds with time cadence of 0.1 seconds, i.e. the data has 1000 snapshots. The radius of the magnetic flux tube was taken to be $r = 4$ m, and the spatial cadence is taken to be 0.1 m for every pixel. In the dataset, the selected modes are taken with different amplitudes and frequencies, except two modes sharing the same frequency (slow sausage body and surface modes) to validate the ability of POD and DMD to distinguish them.

3.3.1 Results

The POD and DMD analysis have been applied on the generated synthetic dataset presented above, by following the algorithms that were previously de-

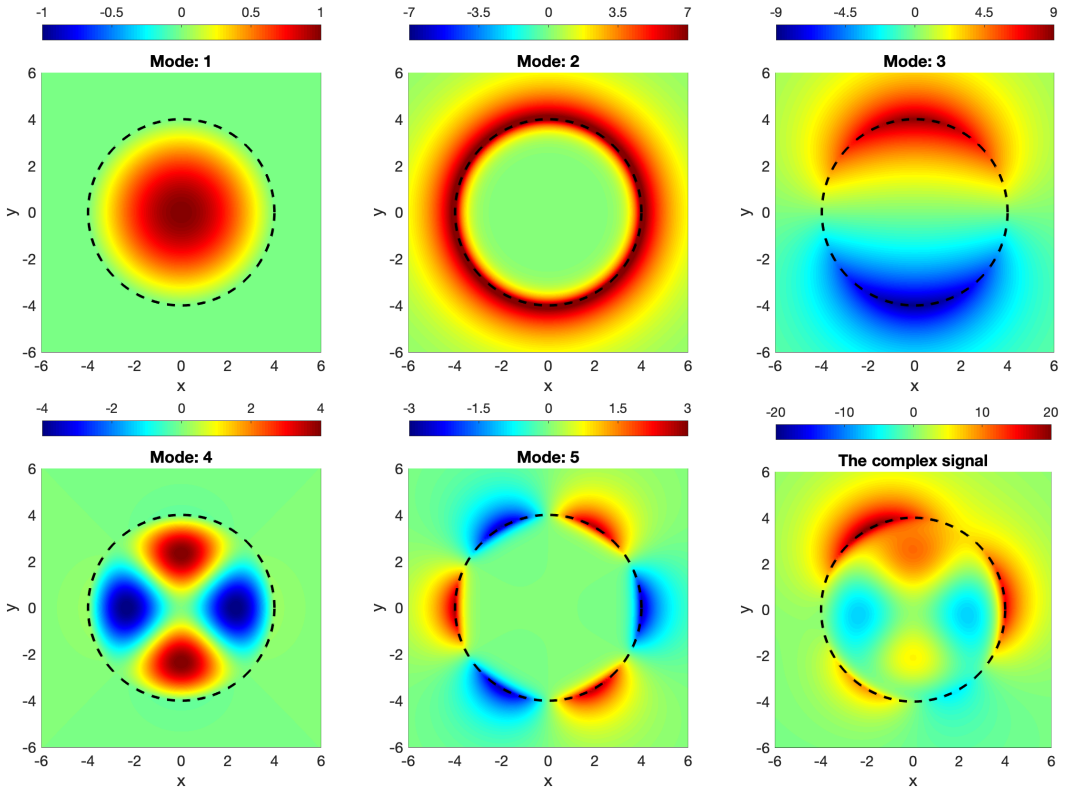

Figure 3.1: The spatial structure of the MHD waves that have been combined in the generated synthetic dataset. These modes are ranked according to their number in Table 3.1. The bottom right panel shows an arbitrary snapshot resulted from the combination of the modes.

scribed in Sections 3.1.1 and 3.2.1.

As mentioned before, the POD decomposes modes in terms of their orthogonality in space and it provides a clear ranking of the POD modes in terms of their contribution to the total variance of the signal. Hence, the number of POD modes that we expect to obtain is identical with the number of snapshots of the dataset, and their ranking is shown in Figure 3.2.

The spatial structure of the POD modes are shown in Figure 3.3, that proves the power and capability of the POD to recover all the 5 modes, even the modes that are sharing the same frequency. The reason for that, is the governing function in the radial direction of the theoretical model in the cylindrical magnetic flux tube are Bessel functions, which are orthogonal to each other, and hence as the POD identifies modes in terms of their orthogonality in space it has recovered all the 5 modes. Moreover, in Figure 3.2, it is clear that there is a gap in the power corresponding the first 4 modes and the fifth one that can be explained by taking into account that despite the slow surface sausage mode and the slow body sausage mode have the same

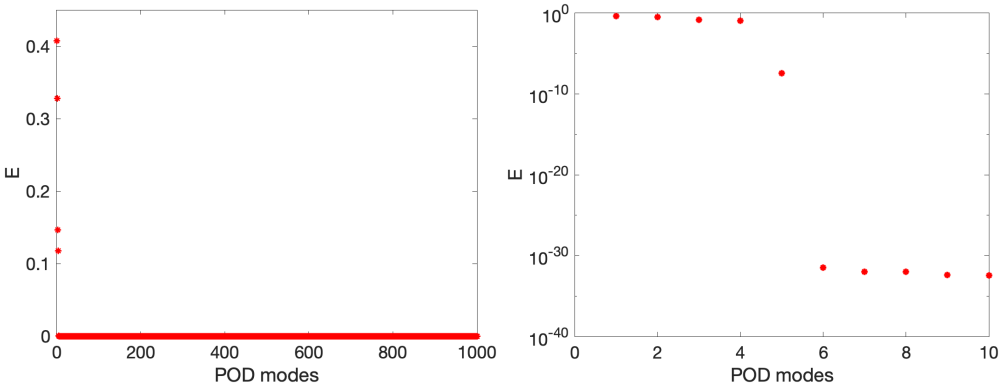

Figure 3.2: The power of the POD modes contributing to the signal, and that obtained from Equation (3.3). The left panel shows all modes recovered using the POD, while the right panel shows a zoom-in region for the first 10 modes (in logarithmic scale).

frequency, their amplitude is different, making the slow body sausage mode less important (after all, the energy of a mode is proportional to the square of their amplitude).

From the possible 1000 POD modes we select our 5 modes, the rest of the modes are having weightless contribution to the signal as shown in Figure 3.2. In addition, the spatial structure of POD 6 (and subsequent modes) displays an unrecognizable pattern with an insignificant contribution since we only have 5 modes in the synthetic dataset, as shown in Figure 3.3 for POD 6.

An additional output of the POD is the temporal evaluation of the POD modes. Hence, the power spectrum is calculated to obtain the frequency of the POD modes as shown in Figure 3.4. This power spectrum shows that the POD 2 and POD 5 modes are sharing the same frequency. Furthermore, it is clear that there is an agreement between the power of the POD modes and their frequency with the input of MHD modes in Table 3.1.

Finally, in order to obtain the spatial and temporal output of the POD modes, we can take the product of the spatial structure of the POD modes, as shown in Figure 3.3, the diagonal elements, λ, which are shown in Figure 3.2 and the one-dimensional time coefficients of the mode.

Regarding the identification of modes using DMD, this technique assumes a temporal orthogonality, i.e. different modes must not have identical frequencies. As the DMD does not rank the mode in anyway, the challenge is to identify the relevant modes as they are spread randomly among the 999 DMD modes. Therefore, following the approach developed by Higham et al. (2018),

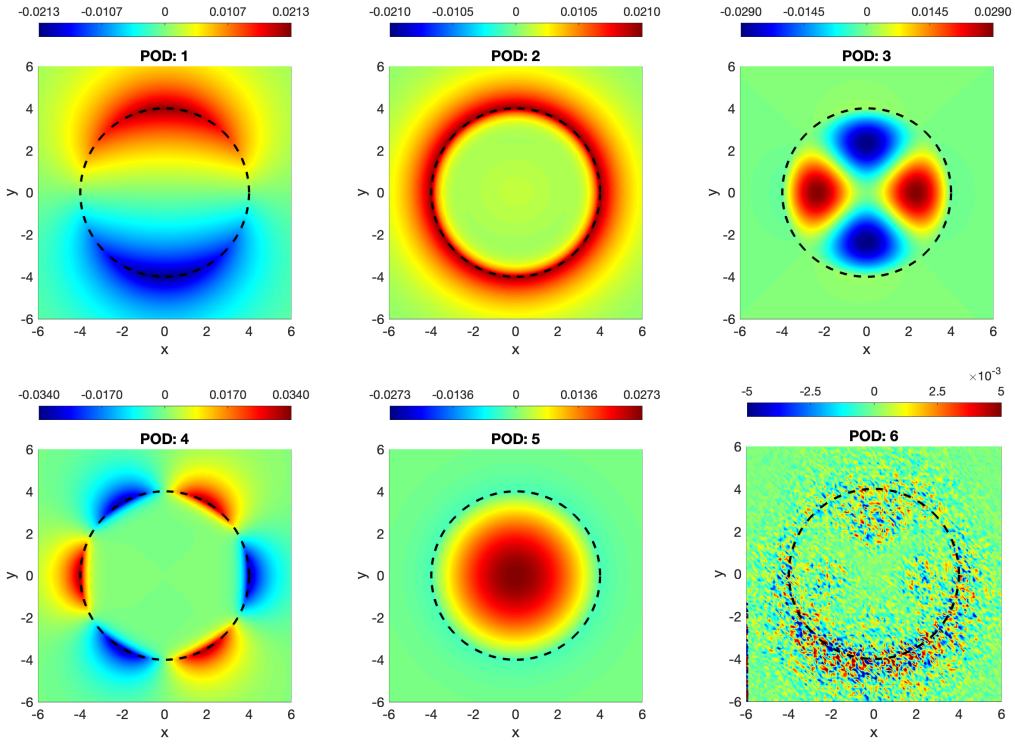

Figure 3.3: This figure shows the spatial structure of the first 6 POD modes.

we have identified our target frequencies from the power spectra of the POD time coefficients associated with the dominant modes, where the dominant frequencies are shown in Figure 3.4. Hence, the spatial structure of the DMD modes that are associated with the dominant frequencies are shown in Figure 3.5 and it is clear that the DMD has recovered the modes in terms of their frequencies, i.e. it was not able to recover all the five modes as two of them are sharing the same frequency (0.05 Hz). The DMD mode that correspond to the frequency of 0.05 Hz is a superposition of the slow body sausage mode and the slow surface mode, however, the DMD mode correspond to the slow surface sausage mode, as this is the dominant mode in that frequency.

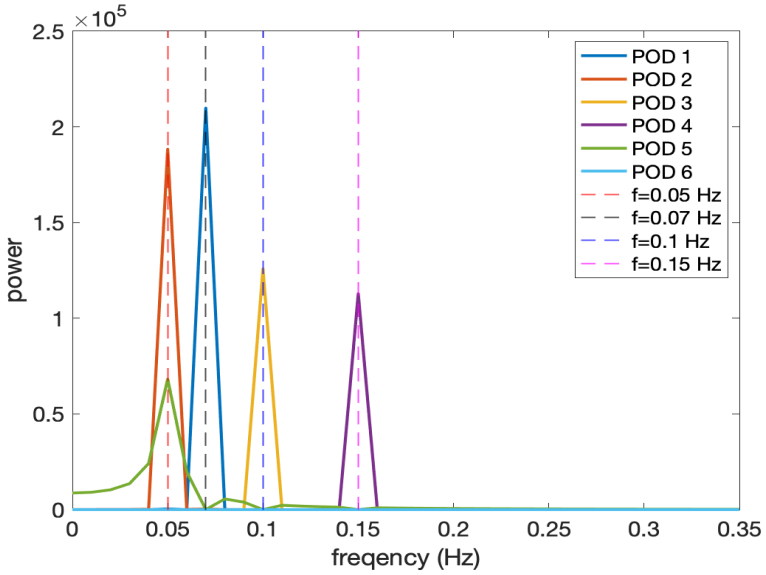

Figure 3.4: This figure shows the power spectra of the temporal evolution of the first 6 POD modes. These time evaluations are obtained from the expression of S^* in Equation (3.2).

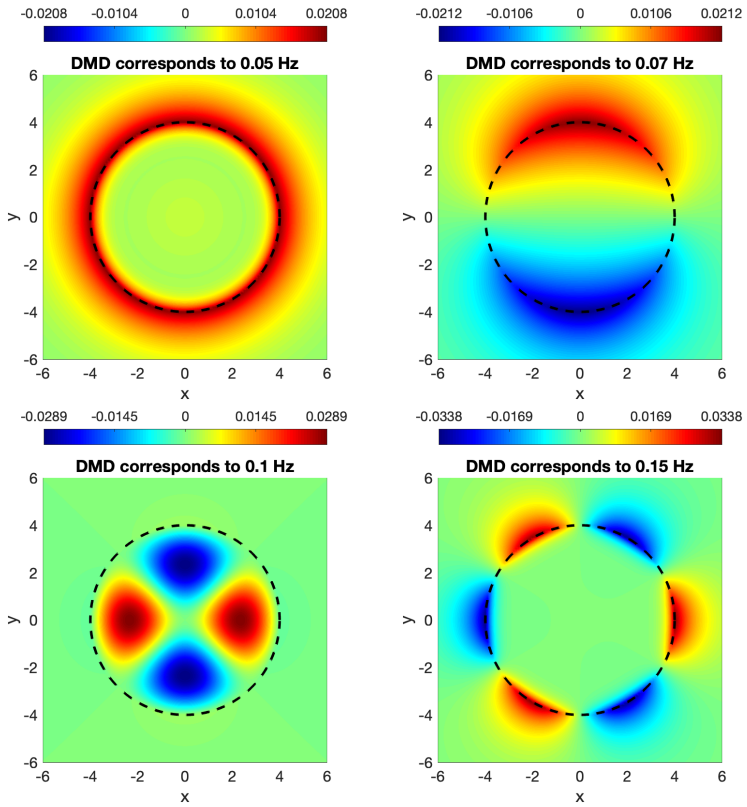

Figure 3.5: This figure shows the spatial structure of the 4 DMD modes, While the corresponding frequency for each DMD mode is shown in the title of each panel.

3.4 Summary

The present Chapter provides a detailed description of the POD and DMD decomposition techniques that will be used later in this Thesis. To validate the two techniques, these were applied to a set of synthetic data recovered from a theoretical model of wave propagation in a magnetic flux tube. The used dataset contained a superposition of possible five guided MHD modes of different types. This test case also provides the reference level for our mode identification carried out for realistic waveguides.

Our results show the remarkable capability of the POD and DMD techniques to recover the mode. The POD has recovered all 5 modes that where combined, even modes sharing same frequency, as it assumes the orthogonality in space. On the other hand, since the DMD assumes the orthogonality in time, it has recovered only 4 modes as two modes share the same frequency. Nevertheless, the technique showed the pattern of the dominant mode.

In the following Chapter, we will use the POD and DMD on an actual data originated from the observation of a sunspot, that has previously been analysed by Jess et al. (2017) using Fourier analysis filtering to detect the rotating motion of the slow body kink mode. Using the POD and DMD, we will aim to recover their identified mode, that can be considered as a further test to our techniques. The challenge that will need to face is that, unlike the ideal synthetic numerical dataset we used in this Chapter, in reality the realistic observations contains noisy data, and the resulting signal is complicated.

CHAPTER 4

Proper Orthogonal and Dynamic Mode Decomposition of Sunspot Data [1]

4.1 Introduction

To the present day the majority of research on sunspot oscillations has been carried out by Fourier transforming the observational data to produce, for example, power spectra, either on a pixel by pixel basis or by integrating over a specific Region of Interest (ROI). Although such analysis can provide valuable information for the identification of coherent structures, e.g. MHD wave modes, in the temporal and spatial domain across a particular ROI, the basic Fourier transform approach has its limitations. Despite this, one can fine tune a Fourier filter in the spatial and temporal domains to try and identify particular MHD wave modes, as was presented by Jess et al. (2017) in order to detect a slow kink body mode in a sunspot umbra.

The aim of the research presented in this chapter is to apply the more advanced techniques of POD and DMD to identify low order MHD wave modes as coherent oscillations across the sunspot umbra, both in the spatial and temporal domains, using the same sunspot data as Jess et al. (2013, 2016, 2017).

4.2 Observation

The sunspot observation employed in this Chapter was acquired using the HARDcam, which is an upgrade to the Rapid Oscillations in the Solar Atmosphere (ROSA; Jess et al., 2010) imaging system available as a common-user instrument at the National Solar Observatory's Dunn Solar Telescope (DST). Each observational image sequence was acquired through a narrowband 0.25 Å

[1] This Chapter is based on the study of Albidah et al. (2021).

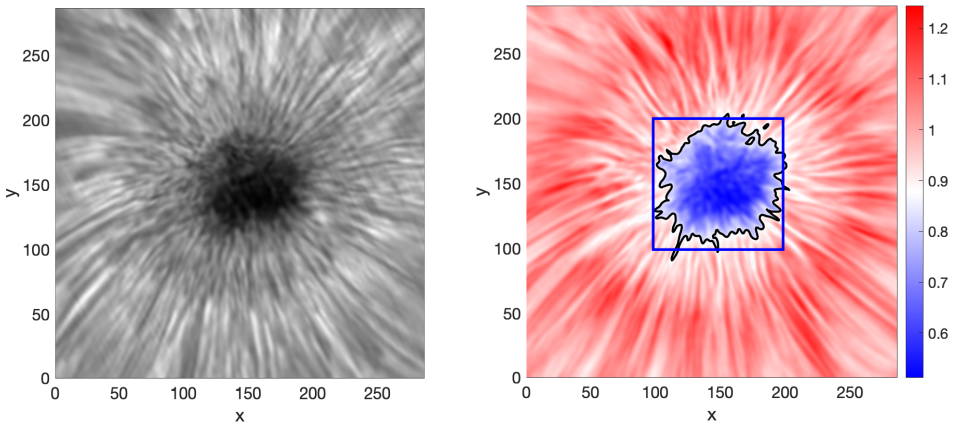

Figure 4.1: A snapshot from the Hα time series (left panel) with the spatial scale in pixels (one pixel has a width of 0.138″ which is approximately 100 km on the surface of the Sun). The right panel shows the mean intensity of the time series, the colourbar displays the magnitude of the mean time series, the solid black line shows umbra/penumbra boundary (intensity threshold level 0.85) and the blue box (101 × 101 pixels) shows the region where our POD and DMD analysis is applied.

(full-width at half-maximum) filter centered on the chromospheric Hα absorption line at 6562.808 Å. The sunspot formed part of NOAA 11366 active region, which was located at heliocentric coordinates (356″, 305″), or N18W22 in the conventional heliographic coordinate system. A pixel size of 0.″138 per pixel was chosen to provide a field-of-view size equal to 71″ × 71″. Images were acquired over the course of 75 minutes (16:10 – 17:25 UT) at a cadence of 1.78 s, i.e. the data has 2528 snapshots.

The dataset has previously been employed for studies of running penumbral waves Jess et al. (2013), connections between photospheric and coronal magnetic fields Jess et al. (2016) and in the detection of an umbral kink mode Jess et al. (2017) due to the excellent seeing conditions and the highly circularly symmetric shape of the sunspot umbra. A sample Hα image of the sunspot is displayed in the left panel of Figure 4.1.

4.3 MHD wave modes identification and discussion

Our goal is to use POD and DMD in combination to identify coherent oscillations across the sunspot's umbra and compare these modes with the MHD wave modes of a cylindrical magnetic flux tube predicted from theory.

The blue box shown on the right panel of Figure 4.1 delimitates the particular region of interest (ROI) of the sunspot umbra we are going to study. Firstly, this ROI will be analysed by using the POD technique. As mentioned earlier in Chapter 3, the number of modes that will be recovered from applying POD is the same as the number of snapshots in the time series (i.e. 2528 mode). However, POD ranks the modes based on their contribution to the overall variance, while their contribution is shown in the left panel of Figure 4.2.

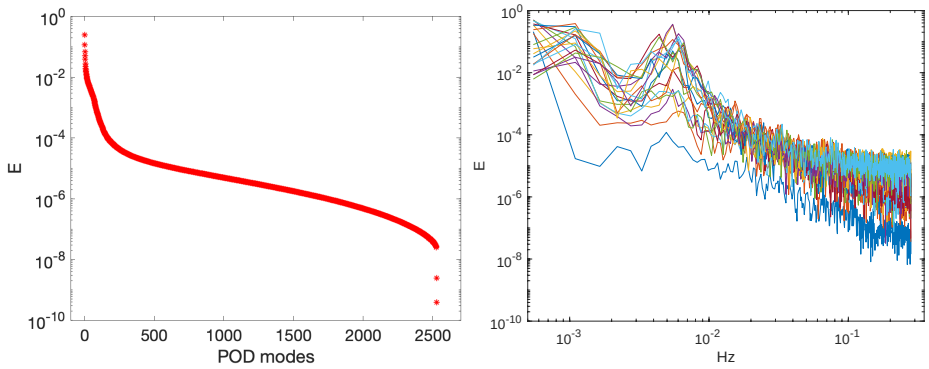

Figure 4.2: The left panel shows the power of all POD modes contributing to the signal (in log scale in y-axis). The right panel displays the power spectral density (PSD) of the time coefficients of the first 20 POD modes (in log scale). The PSD shows peaks between frequencies 4.3 mHz and 6.5 mHz (corresponding to periods of 153 - 232s).

This step is followed by the calculation of the power spectral density (PSD) of the associated POD time coefficients. The PSD of the first 20 modes displayed in the right panel of Figure 4.2 show a series of frequency peaks between 4.3 mHz and 6.5 mHz. The PSD of the individual POD modes are then used to determine the dominant frequency, or frequencies if there are a mix of frequencies, associated with a particular POD mode, so that this information could be applied to determine the coherent spatial structure of modes with distinct frequencies using DMD. If there is no exact match between frequencies, the DMD mode closest to the target frequency is selected.

For illustrative purposes we will concentrate on the first branches of the sausage and kink slow body modes, i.e. modes with only one radial node occurring at the umbra/penumbra boundary. The first POD mode shows the clear azimuthal symmetry of a slow body sausage mode as displayed in the first column in Figure 4.3, with a PSD peak at 4.9 mHz as shown in the left panel of Figure 4.5. The DMD mode that corresponds to the frequency of 4.8

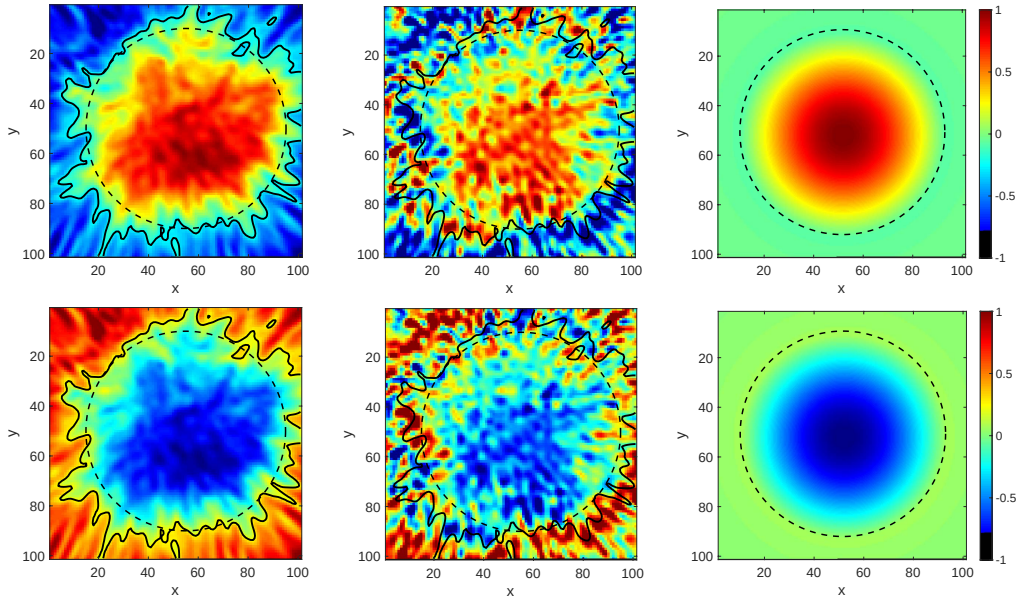

Figure 4.3: The first column displays the spatial structure of the first POD mode with peak power at $f = 4.9$ mHz. The second column displays the spatial structure of the DMD mode that corresponds to the frequency of $f = 4.8$ mHz. The third column shows the density perturbation of a slow body sausage mode in a cylindrical magnetic flux tube and the dashed circle shows the boundary. In the first and the second columns the solid black line stands for the umbra/penumbra boundary as shown in the right panel of Figure 4.1 and the dashed circle is used to compare the observations with the flux tube in the third column. The images in the two rows are chosen to be in anti-phase, hence, they represent different time snapshots.

.

mHz is shown in the second column in Figure 4.3. The third column displays the density perturbation of the slow body sausage mode from the theoretical cylindrical magnetic flux tube model.

The use of predictions of the theoretical model is important for comparison since the MHD wave modes in a cylindrical flux tube are spatially orthogonal. As we specified earlier, POD defines modes by spatial orthogonality. Therefore, in the approximately circular umbra we study, the POD is expected to perform well. What is more remarkable is that the DMD technique, which does not have any such criteria, still manages to identify the sausage mode. From both, the POD and DMD analysis, it is clear that there is strong oscillatory power in the penumbra at 4.8 mHz and the penumbral filaments can clearly be identified. Obviously, the idealised cylindrical magnetic flux tube model cannot recreate this oscillatory behaviour since it assumes a simple quiescent environment without complex fibril structuring. In addition, it is important

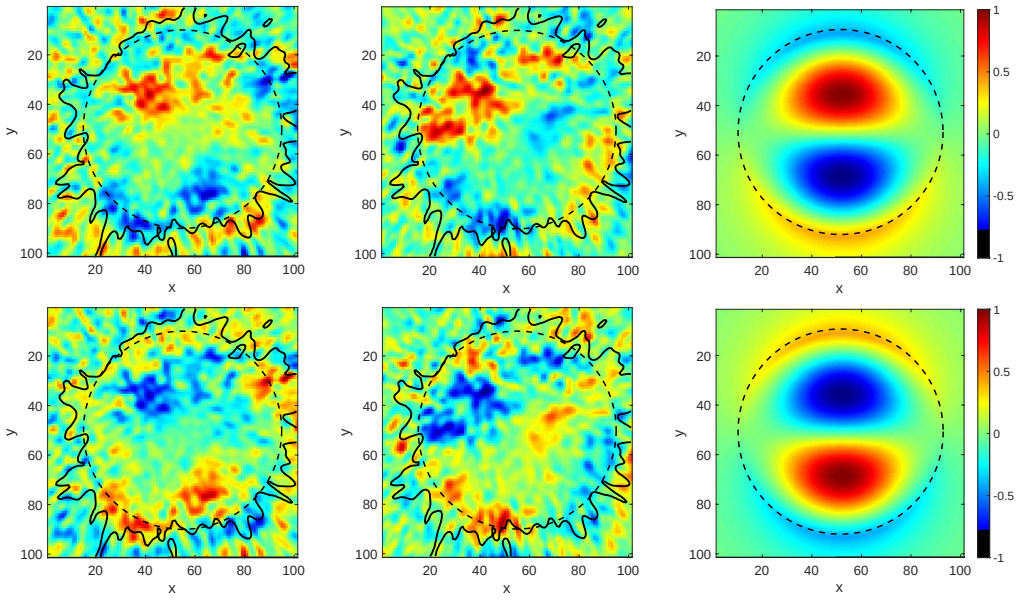

Figure 4.4: The first column displays the spatial structure of the 13^{th} POD mode with peak power at $f = 6$ mHz. The second column displays the spatial structure of the DMD mode that corresponds to the same frequency of $f = 6$ mHz. The third column shows the density perturbation of a slow body kink mode in a cylindrical magnetic flux tube, with the dashed circle indicating the boundary of the tube. In the first and the second columns the solid black line shows the umbra/penumbra boundary as presented in the right panel of Figure 4.1 and the dashed circle is to compare the observations with the flux tube in the third column. The images in the two rows of this figure are chosen to be in anti-phase, hence, they represent different time snapshots.

.

to state that even within the umbra, disagreement between observations and the eigenmodes of a magnetic cylinder could simply be due to the fact that the observed oscillations are being continually forced oscillations that contain the oscillatory footprint of the driver.

The next POD component that can be interpreted as a physical MHD wave is the 13^{th} mode which has the azimuthal asymmetry of a slow body kink mode, as shown in the first column of Figure 4.4, with a peak at 6 mHz (the right panel of Figure 4.5). The DMD mode with frequency of 6 mHz is displayed in the second column in Figure 4.4. Again, for comparison the slow kink body mode from cylindrical flux tube theory is shown in the third column. Here we can compare these results with the previous work of (Jess et al., 2017). These authors identified a kink mode rotating in the azimuthal direction by implementing a $k - \omega$ Fourier filter ($0.45 - 0.90$ arcsec^{-1} and $5 - 6.3$ mHz). Hence, the frequency of the kink mode from the POD and DMD

analysis is certainly in the same frequency range as the filter applied by Jess et al. (2017). Our analysis reveals that the time coefficients of the POD modes are almost sinusoidal. This is remarkable since POD puts no such condition on these coefficients. Hence, Fourier analysis, which has a sinusoidal basis in the temporal domain, in retrospect was a valid approach. The use of the Fourier analysis is often problematic since it assumes a sinusoidal basis in the spatial domain. However, in the cylindrical model the basis functions in the radial direction are Bessel functions that can be reduced to trigonometric functions under strict conditions (see Edwin and Roberts (1983)). The strength of POD is that it uses a spatially orthogonal basis, regardless of the geometry of the observed waveguide. The other important advantage of both POD and DMD over Fourier analysis is that these methods cross-correlate individual pixels in the ROI, in the spatial and temporal domain, respectively. This ability is a distinct advantage in identifying a coherent oscillations across the whole umbra. In agreement with the sausage mode identification in Figure 4.3, the spatial structure of the POD and DMD modes in the first and second columns of Figure 4.4 is very similar even though the DMD places no restriction on the mode being orthogonal. This further strengthens the argument that the kink mode interpretation of the identified wave is indeed physical.

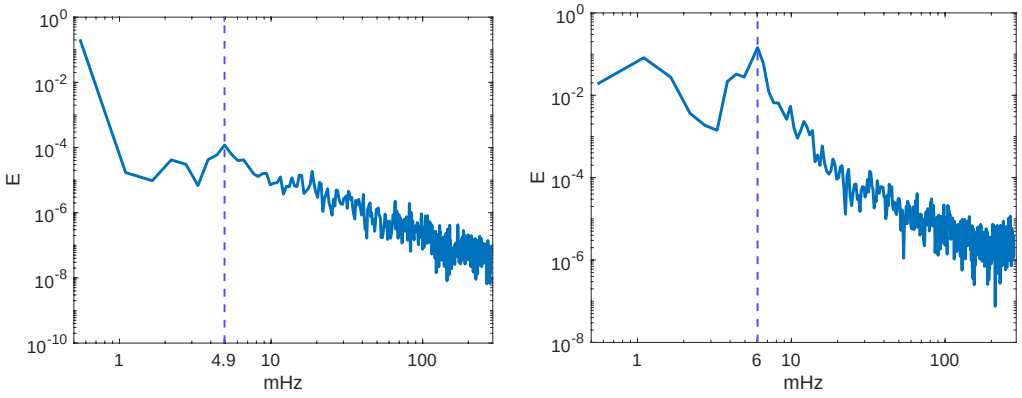

Figure 4.5: The left panel displays the PSD of POD 1 mode and it has a peak at 4.9 mHz, while the right panel displays the PSD of POD 13 mode with a a peak at 6 mHz.

Here we would like to investigate the apparent rotational motion of the kink mode detected by Jess et al. (2017), who constructed a time-azimuth diagram around the circumference of the umbra and estimated an angular velocity of approximately 2 deg s^{-1} and a periodicity of about 170 s. Physically, the rotational motion could be explained by having either (i) a kink mode that is standing in the radial direction but propagating in the azimuthal direction, or

(ii) it could be result of the superpostion of two approximately perpendicular kink modes (both standing in the radial and azimuthal directions). Before attempting to recover this rotational motion with the POD and DMD techniques we should emphasise that the filtering process performed by Jess et al. (2017) crudely oversimplified the complexity of the swirling "washing machine" motion in the original signal. In particular, the 40 s wide temporal filter could contain at least least 7 DMD modes. Spatially, the filter effectively divided the umbra into quadrants. To recreate the apparent rotational motion (or approximate circular polarisation) with POD we need to superimpose at least two spatially perpendicular kink modes with similar, but not necessarily identical, periods. From our analysis this requires the superposition of POD 10 (the left panel of Figure 4.6 and POD 13 shown on the first column on Figure 4.4).

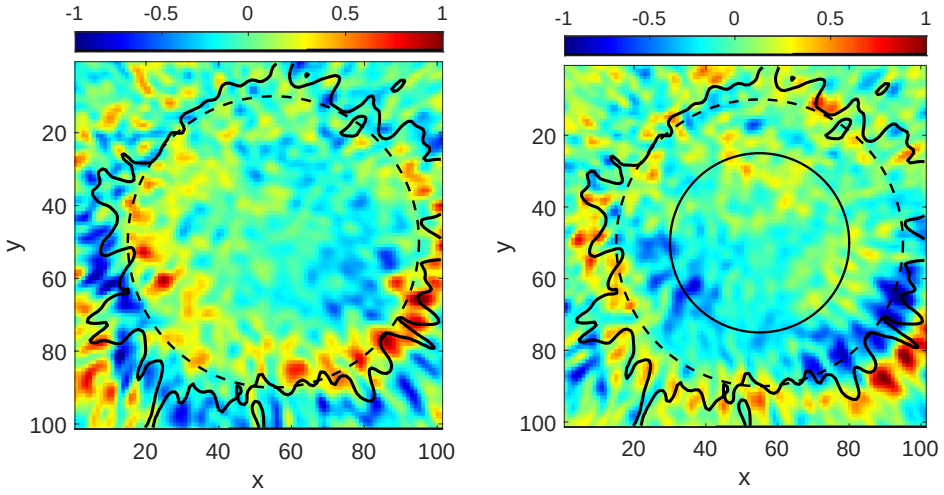

Figure 4.6: Left panel displays POD 10, which is orthogonal in space to POD 13 that is shown on the first column of Figure 4.4. The right panel shows the DMD mode with a frequency of 5.4 mHz and it is approximately orthogonal in space to the DMD mode with a frequency of 6 mHz displayed in the second column of Figure 4.4. The solid black circle displays the path of the time-azimuth diagram in Figure 4.7.

From the left panel of Figure 4.7 it is clear that the PSD of POD 10 has a peak at 5.4 mHz, while the PSD of POD 13 has a peak at 6 mHz (the right panel of Figure 4.5), with both frequencies within the temporal filter chosen by Jess et al. (2017). We can also recreate this rotational motion by superimposing at least two DMD modes. Although DMD modes are not defined to be orthogonal in space, we still find two examples of kink modes using DMD that are approximately perpendicular to each other. These modes correspond to a frequency of 5.4 mHz (see the right panel of Figure 4.6) and 6 mHz (which

we have mentioned earlier and shown on the second column of Figure 4.4). A similar time-azimuth analysis to Jess et al. (2017) was performed on the superposition of these two DMD modes along the solid black circle shown on the right panel of Figure 4.6, where the signal was strongest. This resulted in an angular velocity of about 2 deg s^{-1} and periodicity of approximately 170 s (see the right panel of Figure 4.7), consistent with the result of Jess et al. (2017).

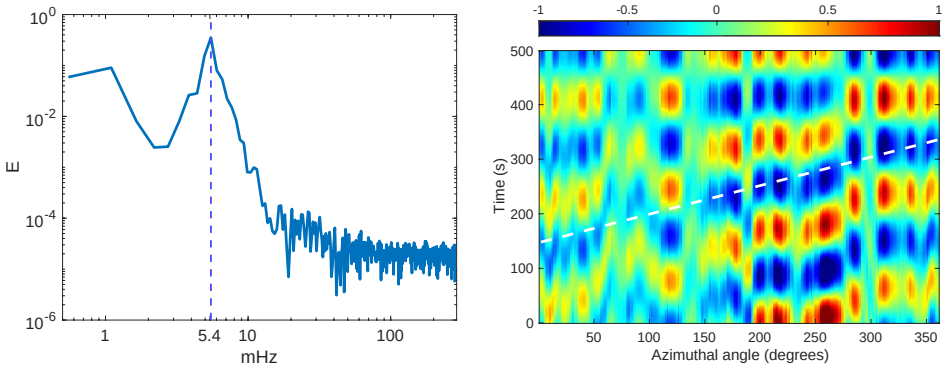

Figure 4.7: The left panel displays the PSD of POD 10. It has a peak at 5.4 mHz. The right panel shows the time-azimuth diagram after the superposition of two approximately spatially perpendicular kink modes identified with DMD. The white dashed line on the right panel gives an apparent angular velocity of about 2 deg s^{-1} consistent with the result of Jess et al. (2017).

To compare the results of the theoretical cylindrical model with the POD modes from the observational data, we performed the cross-correlation analysis (Di Stefano et al., 2005; Tahmasebi et al., 2012), calculated on a pixel-by-pixel basis for the sausage (see Figure 4.3) and kink (see Figure 4.4) modes, as shown on Figure 4.8. The general mathematical formula to indicate the elements of the two dimensional cross-correlation of two matrices X (of size $M \times N$) and H (of size $P \times Q$) is described as

$$C(k,l) = \sum_{m=0}^{M-1} \sum_{n=0}^{N-1} X(m,n) H(m-k, n-l) \quad \text{where} \quad \begin{matrix} -(P-1) \leq k \leq M-1 \\ -(Q-1) \leq l \leq N-1. \end{matrix} \tag{4.1}$$

The above equation describes the elements of the correlation matrix C, where the size of C is $(M+P-1)$ by $(N+Q-1)$. However, in our analysis we have calculated the correlation on a (pixel-by-pixel) basis. Therefore, the output of the correlation will be the product of the two values of the two pixels. The result of the correlation is a number between 1 and -1, where 1 means that the pixels have a linear correlation while -1 denotes a linear anti-correlation.

Certainly, there is a better correlation for the sausage than the kink mode, however, this result is not surprising given that the signal for the kink mode is weaker than the signal corresponding to the sausage mode (see Figures 4.4 and 4.3). Nevertheless, the kink mode stills shows a good correlation in the regions where its amplitude is maximum (see Figure 4.8).

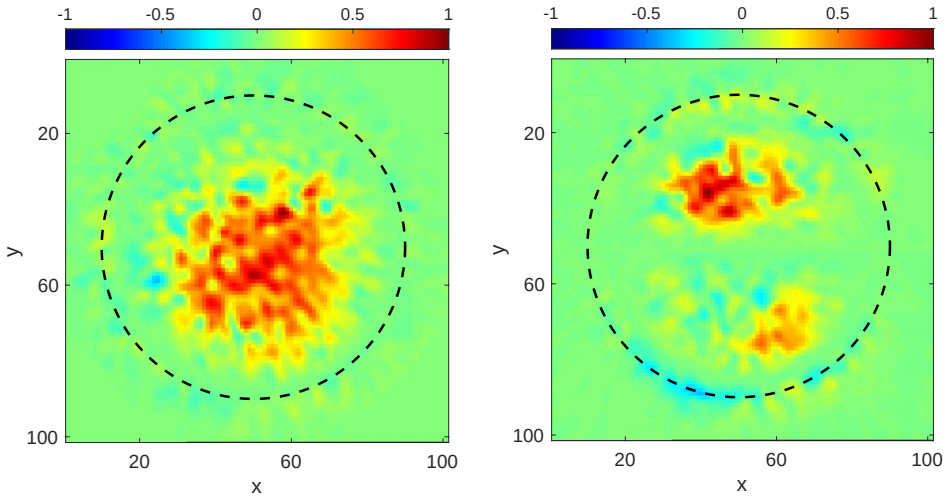

Figure 4.8: The left panel displays the cross-correlation between theoretically constructed and observationally detected sausage mode shown in Figure 4.3 and the kink mode shown in Figure 4.4. The positive/negative numbers in the colourbar denote correlation/anti-correlation.

4.4 Summary and Conclusions

Each method used to identify coherent oscillations across sunspots and pores has its particular strengths and weaknesses. We have demonstrated here that a more considered and multi-faceted approach can be more robust in pinpointing modes that are actually physical. For example, the analysis by Jess et al. (2017) required fine tuning of the Fourier filters in the temporal and spatial domain to reveal the umbral kink mode confirmed by our POD and DMD analysis. In contrast, POD requires no such filtering, and filtering would completely skew the results. The inherent problem with POD is the identification of real physical modes, as this method produces as many modes as there are time snapshots. This is where further analysis is required, as demonstrated in this study and previously by Higham et al. (2018). By calculating the PSD of each POD mode the dominant frequency (or frequencies) of each mode can be identified and these can be paired with the unique frequencies associated each DMD mode allowing for comparison between the spatial structure of

the modes produced by both methods. If there is agreement between the spatial structure of both the POD and DMD modes (up to some specified accuracy), then this provides compelling evidence that the mode is indeed physical. The results of the combined approach of using POD and DMD have been used to identify more than one MHD wave mode in a sunspot and the results were published (see, Albidah et al., 2021). We, therefore, suggest that in combination, POD and DMD could prove to be indispensable tools for decomposing the many possible MHD wave modes that could be excited in sunspots and pores, especially with the advent of high resolution observations provided by present and near future ground- and space-based observatories (e.g. Dunn Solar Telescope (DST), Swedish Solar Telescope (SST), The Daniel K. Inouye Solar Telescope (DKIST), etc).

CHAPTER 5

Magnetohydrodynamic wave mode identification in circular and elliptical sunspot umbrae: evidence for high order modes [1]

5.1 Introduction

One of the most rapidly emerging disciplines in solar physics is the study of MHD waves and oscillations in the solar atmosphere thanks to the high resolution and high cadence observations of the last few decades. Observed properties of waves and oscillations help in determining the properties of plasma and magnetic field that cannot be directly or indirectly measured. Lower order modes (sausage and kink) are continuously observed in solar magnetic structures, and their literature is vast. However, higher order modes, i.e. fluting modes were so far elusive and their existence was purely hypothetical.

The existence of higher order modes was so far mostly predicted theoretically (see e.g. Edwin and Roberts, 1983) and the very few studies of these modes used indirect methods to show their existence. Based on the observations obtained with the help of the Fast Imaging Solar Spectrograph installed at the 1.6 m Goode Solar Telescope (GST), Kang et al. (2019) suggested that the observed two-armed spiral wave patterns in pores could be explained in terms of a superposition of slow sausage body mode (corresponding to an azimuthal wavenumber $n = 0$) and a flutting mode ($n = 2$). However, correlation analysis between numerically simulated and observed modes to validate obtained results was not included in their study.

In this chapter we apply the techniques of POD and DMD on two datasets associated with the sunspots. The first one has a circular cross-sectional shape (that we have used in the previous chapter to identify the fundamental slow body sausage and kink modes), and we aim to expand our analysis to see

[1] This Chapter is based on the study of Albidah et al. (2022)

whether there are different modes are present, while the second sunspot has an elliptical cross-sectional shape. The present chapter also investigates how reliable are the POD and DMD methods in the identification of the surface and the body mode waveguides of different cross-sectional shape. The oscillatory pattern of the observed modes are compared with the theoretical models constructed for a waveguide with cylindrical (section 2.2.3), elliptical (section 2.2.4), and the irregular (section 2.2.5) cross-section.

5.2 Observation

In this section we describe the observation of the elliptical sunspot, while the observation of the circular sunspot has been already described earlier in section 4.2.

The sunspot observation employed in this chapter was acquired using the HARDcam. Each observational image sequence was acquired through a narrowband 0.25 Å (full-width at half-maximum) filter centered on the chromospheric Hα absorption line at 6562.808 Å. The sunspot formed part of NOAA 12146, which was located at heliocentric coordinates (496″, 66″), or N10W32 in the conventional heliographic coordinate system. A diffraction-limited pixel size of 0.″108 per pixel was chosen to provide a field-of-view size equal to 180″ × 180″, which is the maximum allowable by the DST optics. Images were acquired over the course of 120 minutes (13:56 – 15:56 UT) at a cadence of 1.00 s, i.e. the data has 7200 snapshots. The dataset has previously been employed in a study that examined the presence of Alfvén wave driven shocks in sunspot atmospheres (Grant et al., 2018). A sample Hα image of the sunspot is displayed in the left panel of Figure 5.1.

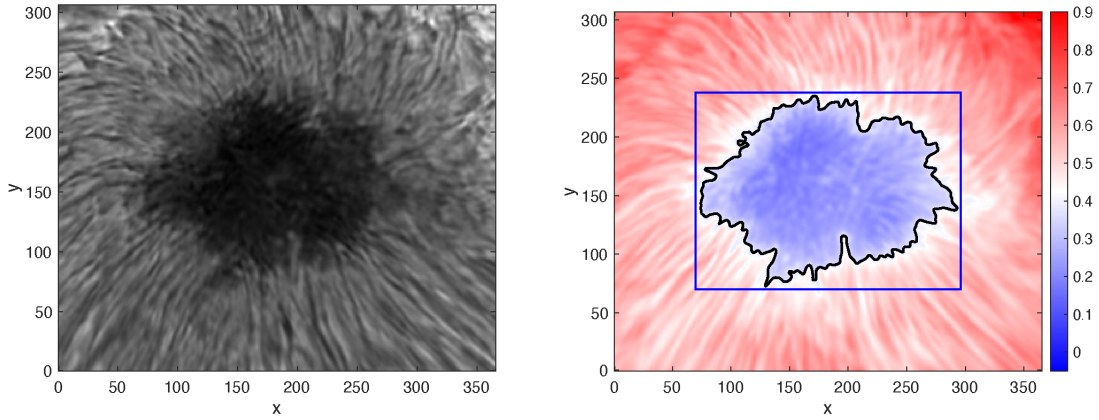

Figure 5.1: The left panel shows a snapshot from the Hα time series of the elliptical sunspot with the spatial scale in pixels (one pixel has a width of $0.108''$ which is approximately 79 km on the surface of the Sun). The right panel displays the mean intensity of the time series. The colourbar displays the magnitude of the mean time series, the solid black line shows umbra/penumbra boundary with intensity threshold level at 0.4. The blue box (220×166 pixels) shows the region where we apply our POD and DMD analysis.

5.3 MHD wave modes identification and discussion

The POD and DMD techniques were applied on the two data-sets associated with a circular and an elliptical sunspots, shown in Figures 4.1 and 5.1, respectively. The oscillatory pattern of modes recovered with the help of these techniques is compared with the results drawn from theoretical models constructed for a waveguide with cylindrical, elliptical, and the irregular cross-section. The comparison is quantified by means of a cross-correlation analysis, calculated on a pixel-by-pixel basis.

Furthermore, as POD provides information about the temporal evolution of the coefficients of the POD modes, we can determine the PSD, which will show the most dominant frequencies of modes. Since DMD identifies modes in terms of their frequency, and by using the magneto-acoustic parameters m_i and $\tilde{m}_i$ for the cylindrical and the elliptical models, respectively, the longitudinal wavenumber, k_z, was obtained by using Equation 2.24 for the sunspot with a circular cross-sectional shape (see Table 5.1), and Equation 2.39 for the sunspot with an elliptical cross-sectional shape (see Table 5.2). Here $\omega = 2\pi f$ is the angular frequency, f refers to frequency in Hz, $c_0 = 10$ km s^{-1} is the assumed sound speed, $v_A = 4c_i$ is the Alfvén speed and $\sigma^2 = 0.4174$. With the help

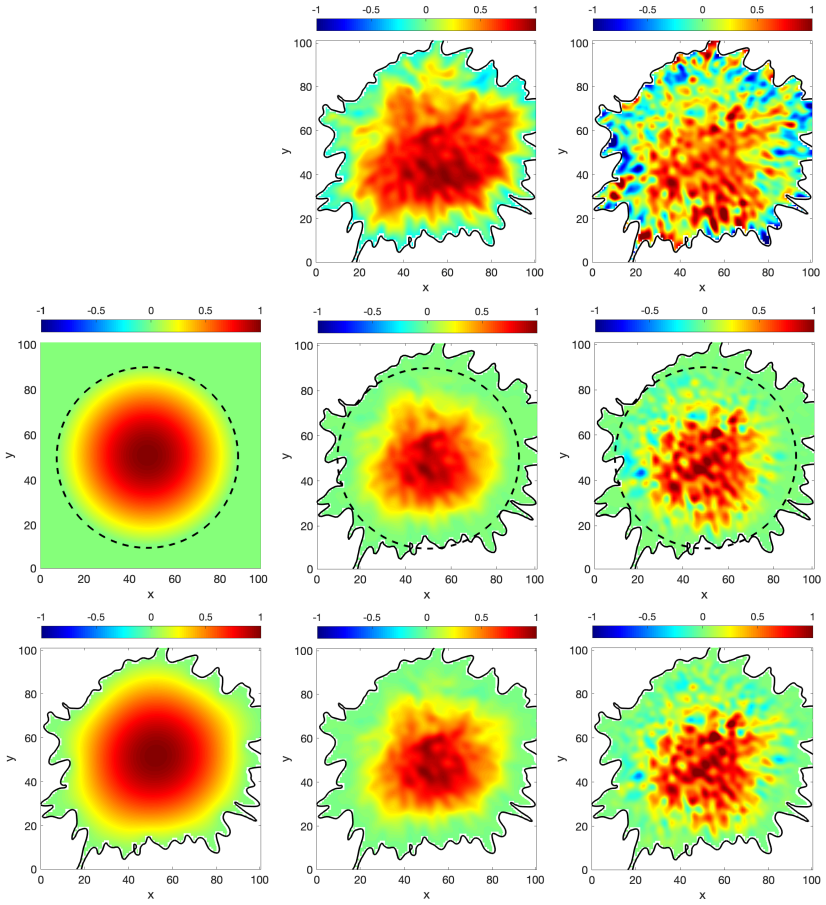

Figure 5.2: The first row displays the spatial structure of the modes that were detected from the observational data, the first POD mode (middle) and the DMD mode that corresponds to the frequency of 4.8 mHz (right). In the first column we display the theoretical spatial structure of the fundamental slow body sausage mode in the cylindrical magnetic flux tube model (middle) and the corresponding structure considering the realistic sunspot with irregular shape (bottom). The rest of the panels are showing the cross-correlation between theoretically constructed and observationally detected modes and the positive/negative numbers in the colourbar denote correlation/anti-correlation. The dashed circles show the boundary of the tube and the solid black line shows the umbra/penumbra boundary. The same configuration was used for Figures 5.3 to 5.6.

of these quantities the wavelength ($\lambda = 2\pi/k_z$) of waves and the phase speed ($V_{ph} = f\lambda$) were calculated for the MHD modes identified by our analysis.

Let us start with the sunspot with a circular cross-section shape shown in the left panel of Figure 4.1. The analysis was applied on the ROI represented by the blue box on the right panel of the same figure, where the umbra/penumbra boundary is shown by a solid black line with an intensity threshold level at 0.85. In addition to the fundamental slow body sausage mode (shown in Figure 5.2),

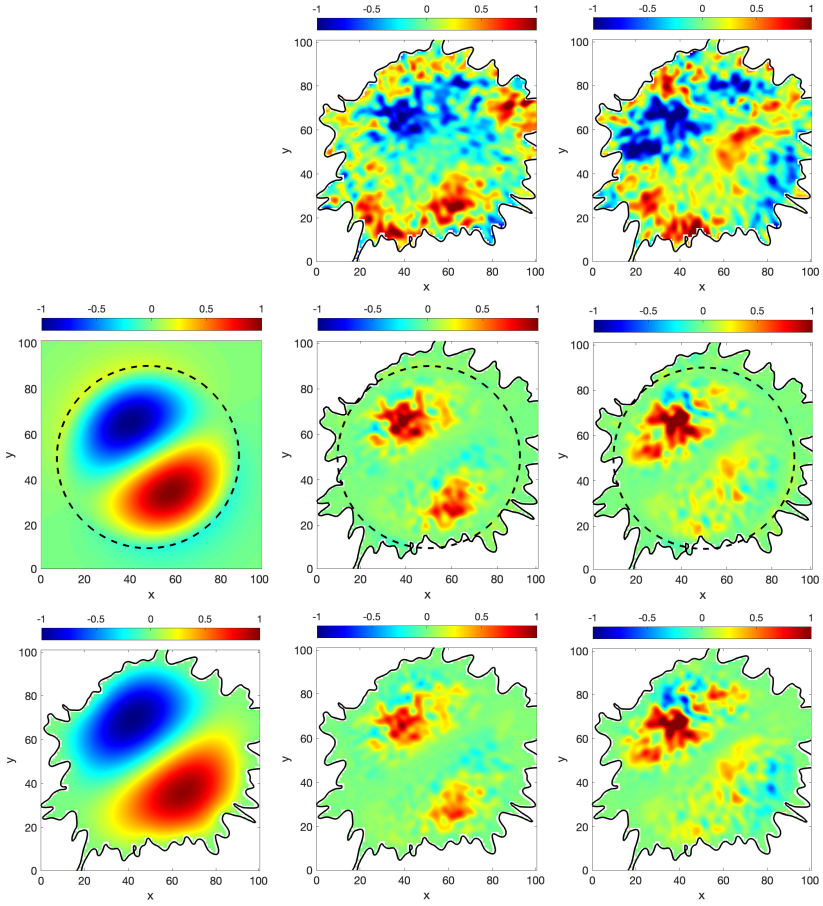

Figure 5.3: This figure displays the 13^{th} POD (top row, 1st panel) and DMD mode (top row, 2nd panel) with a frequency of 6 mHz, which has an azimuthal symmetry of the fundamental slow body kink mode.

and the fundamental slow body kink mode (Figure 5.3) identified previously (in the previous chapter, Albidah et al., 2021), the POD and DMD analysis reveals the existence of the higher-order MHD wave modes.

The POD mode that can be interpreted as a MHD wave mode is the 19^{th} mode which has the azimuthal symmetry of a slow body sausage overtone mode, i.e. a mode with more than one radial node, and the DMD mode that corresponds to the spatial structure has a frequency of 5.6 mHz, as shown in Figure 5.4. The PSD of the time coefficient of POD 19 has a mix of peaks around 4.3 mHz, 5.4 mHz and 6.5 mHz on its frequency domain, as shown in the left panel of Figure 5.7.

The next POD mode that can be interpreted as a MHD wave mode is the 20^{th} component of the POD ranking and it is visible in the DMD decomposition, too. This mode has a frequency of 7.6 mHz, and has an azimuthal symmetry corresponding to a slow body fluting mode ($n = 2$), as shown in

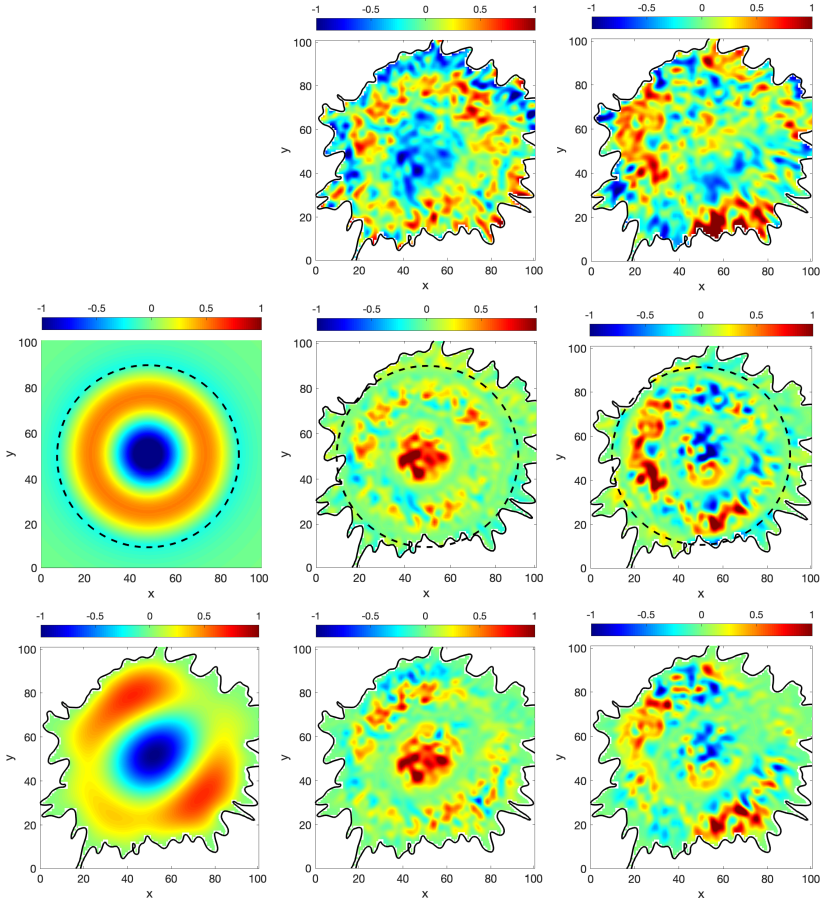

Figure 5.4: This figure displays the 19^{th} POD (top row, 1st panel) and DMD mode (top row, 2nd panel) with a frequency of 5.6 mHz which has an azimuthal symmetry of the slow body sausage overtone mode.

Figure 5.5. The PSD of the 20^{th} POD mode shows a mix of peaks around 3.7 mHz, 5.8 mHz and 7.4 mHz, as shown in the middle panel of Figure 5.7. Finally, the last mode that was detected by the POD and DMD analysis that shows an azimuthal symmetry of a slow body fluting mode ($n = 3$) is the 26^{th} POD component and the DMD mode that corresponds to 7.5 mHz, as shown in Figure 5.6. The PSD of the 26^{th} POD mode shows a mix of peaks at around 3.2 mHz and 7.2 mHz, as shown in the right panel of Figure 5.7.

It is expected that some of the PSD of POD modes may have a mix of peaks in their frequency domain, and this is one disadvantage of the POD technique, therefore, making it difficult to decide which frequency is relevant for the mode identification. However, this ambiguity is resolved by the DMD technique by taking the peaks and finding the DMD mode that correspond to the peaks, allowing us to make a decision on which DMD mode has a spatial structure similar to the mode recovered by means of POD, and hence we consider the

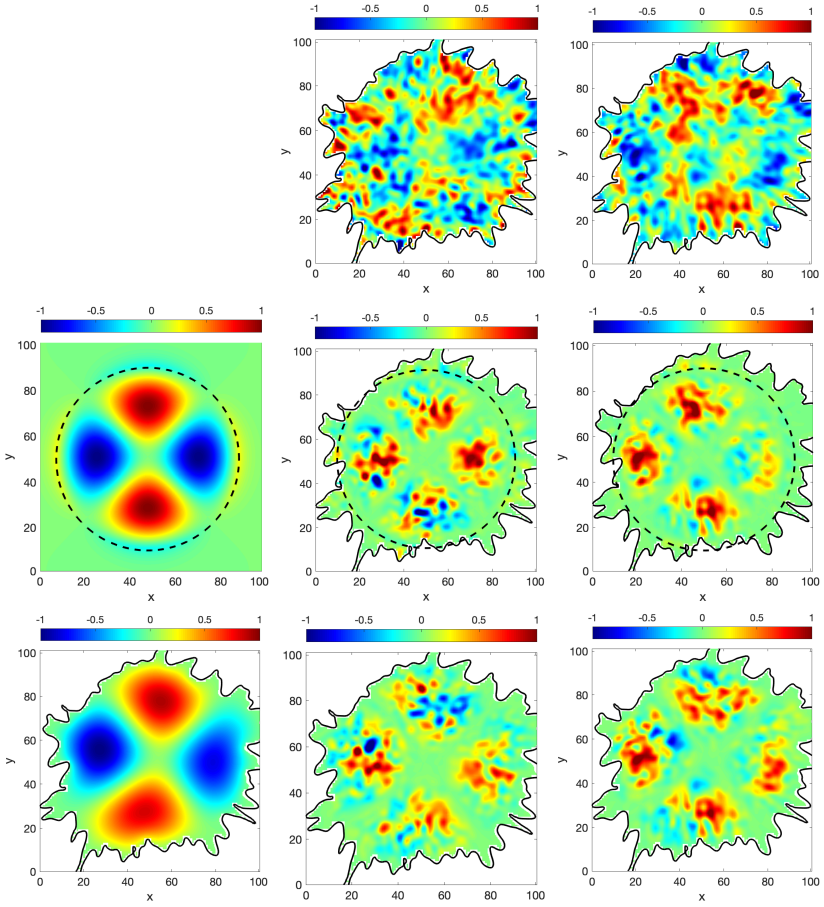

Figure 5.5: This figure displays the 20^{th} POD (top row, 1st panel) and DMD mode (top row, 2nd panel) with a frequency of 7.6 mHz, which has an azimuthal symmetry of the slow body fluting mode ($n = 2$).

distinct frequency of that DMD mode.

The sunspot with an elliptical cross-sectional shape is shown in the left panel of Figure 5.1. The POD and DMD analysis was applied to the ROI shown by the blue box in the right panel of the same figure, where the umbra/penumbra boundary is shown by a solid black line with an intensity threshold level at 0.4. The first POD mode that can be interpreted as a MHD wave is the 1^{st} POD mode that shows the symmetry of the fundamental slow body sausage mode and the associated DMD mode corresponds 3.4 mHz, as shown in Figure 5.8. The PSD of the time coefficient of POD 1 shows peaks around 3.5 mHz and 6.8 mHz, as shown on the top left panel of Figure 5.13. The next mode that can be identified in our data is the fundamental slow body kink mode, and the POD mode that shows a high correlation with this mode of oscillation is POD 14, as shown in Figure 5.9. The PSD of time coefficient of POD 14 shows a clear peak at 5.88 mHz (the top middle panel of Figure 5.13).

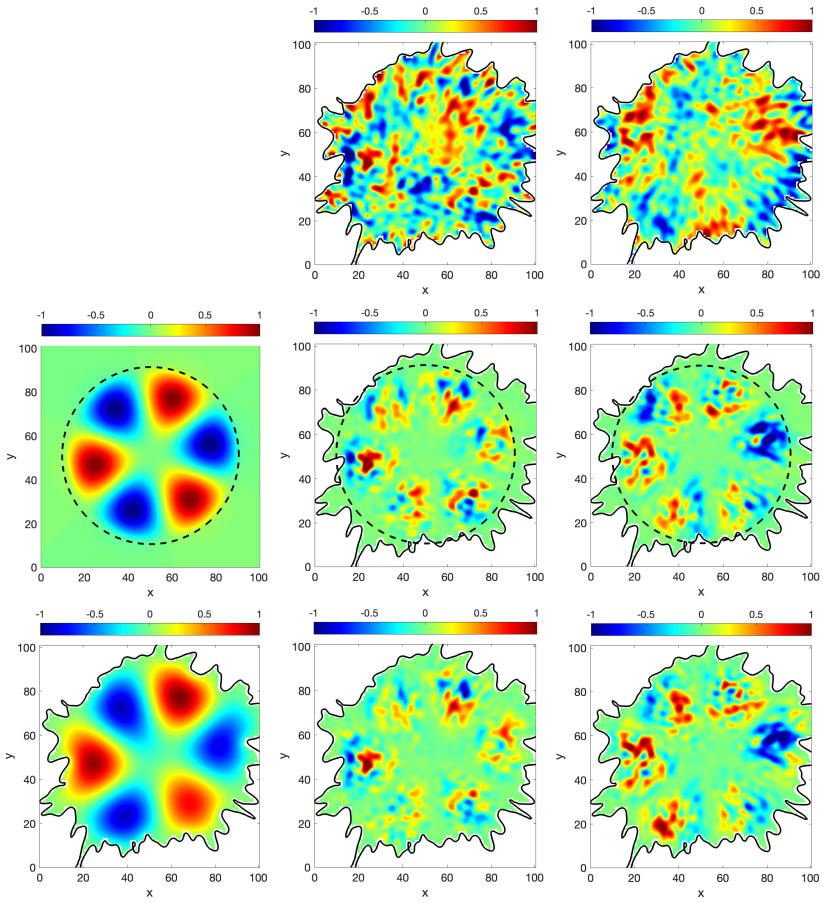

Figure 5.6: This figure displays the 26^{th} POD (top row, 1st panel) and DMD mode (top row, 2nd panel) with a frequency of 7.4 mHz which has an azimuthal symmetry of the slow body fluting mode ($n = 3$).

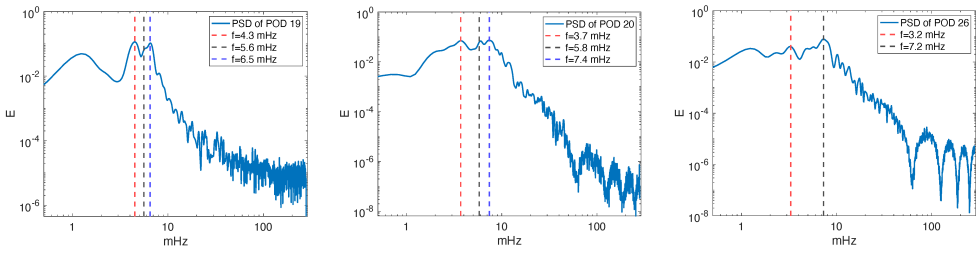

Figure 5.7: This figure shows the power spectrum density (PSD) of the time coefficients of POD 19 (left panel), POD 20 (middle panel) and POD 26 (right panel) modes. The vertical coloured-dash lines represent the values in the frequency domain that correspond to the peaks of the PSD, and the values of the peaks' location are shown in the legend of each figure. The PSD of POD 1 and POD 13 (the fundamental sausage and kink modes) are shown in Figure 4.5

MHD wave mode	m_0	f (mHz)	k_z (Mm^{-1})	λ (Mm)	V_{ph} (Km/s)
Fundamental slow body sausage	1.0353	4.8	3.0022	2.0928	10.04
Fundamental slow body kink	1.6765	6	3.73754	1.6811	10.08
Slow body overtone sausage	2.3754	5.6	3.395	1.8507	10.36
Slow body fluting ($n = 2$)	2.214	7.6	4.7294	1.3285	10.09
Slow body fluting ($n = 3$)	2.7471	7.4	4.55619	1.3790	10.20

Table 5.1: This table displays the summary of the properties of the MHD modes detected by the POD and DMD techniques in the sunspot with circular cross-section. The first column contains the name of the modes, while the second column shows the value of the magneto-acoustic parameter, m_0, (see Equation 2.24). The third column contains the frequency determined from the DMD analysis. The fourth column contains the wavenumber along the vertical direction, and these are calculated by means of Equation 2.24, with $\omega = 2\pi f$, $c_0 = 0.01$ (Mm/s) and $v_A = 4c_0$. The fifth column shows the wavelength ($\lambda = 2\pi/k_z$), while the last column gives the phase speed ($V_{ph} = f\lambda$) of the identified modes.

The DMD mode that shows an azimuthal symmetry with the fundamental kink is the DMD mode that corresponds to 5.8 mHz, as shown in Figure 5.9.

It is important to note that in the case of fundamental modes (both, sausage and kink body modes), the change in the shape of the cross-section (from cylindrical, to elliptical and, finally, to a irregular shape) does not introduce significant changes in the morphology of waves, meaning that these modes can be confidently studied in regular shapes. The above statement proves to be incorrect for higher order modes. The 30^{th} POD mode and the DMD mode that corresponds to 5.3 mHz show a high correlation with the slow body kink overtone mode, as shown in Figure 5.10. The PSD of the time coefficients of the 30^{th} POD shows a peak around 5.6 mHz, as displayed in the left panel, second row of Figure 5.13. The difference in the morphology of this wave between the pattern prediction of an elliptical and realistic (irregular) waveguide is remarkable, making the identification of the mode from observation misleading. Next, the 13^{th} POD mode and the DMD mode that corresponds to 5.6 mHz are the modes that can be interpreted to have a higher correlation with the slow body fluting mode ($n = 2$), as shown in Figure 5.11. The PSD of POD

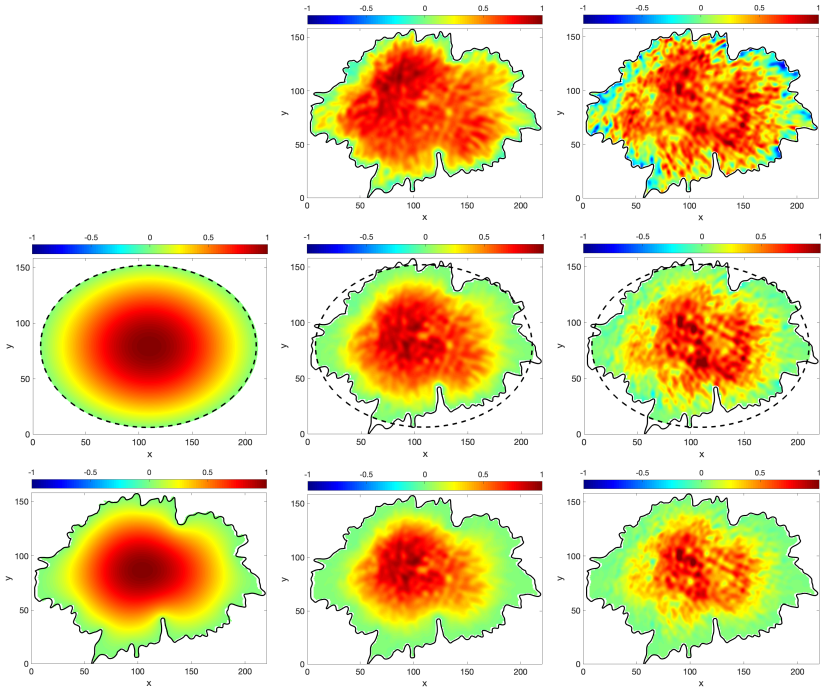

Figure 5.8: The first row displays the spatial structure of the first POD mode (left panel) and the DMD mode that corresponds to 3.4 mHz (right panel). The first column displays the theoretical modes of the fundamental slow body sausage mode in an elliptical magnetic flux tube (middle) and the theoretical modes of the fundamental sausage body mode in the irregular shape that corresponds to the actual sunspot shape (bottom). The rest of the panels are showing the cross-correlation between theoretically constructed and observationally detected modes and the positive/negative numbers on the colourbar denote correlation/anti-correlation. The dashed ellipse shows the boundary of the flux tube and the solid black line shows the umbra/penumbra boundary.The same configuration were used for figures 5.9 to 5.12.

13 shows a peak at 5.8 mHz, as visible in the right panel, first row of Figure 5.13. Finally, the last mode is the slow body fluting mode ($n = 3$) identified as the 18^{th} POD mode and the associated DMD mode with a frequency of 6.2 mHz, as shown in Figure 5.12. The PSD of POD 18 mode has a peak around 6.08 mHz, as shown in the bottom middle panel of Figure 5.13.

Apart from the sensitivity of the modes on the cross-sectional shape of the magnetic waveguide, it is also important to note that there is a higher correlation between the observed modes and the predictions of the model corresponding to the irregular shape. We should also note that there is no complete agreement between the observed modes in either in the circular or elliptical cross-section sunspot and the theoretical models and this disagreement can be attributed to the assumptions made in theoretical models regarding the con-

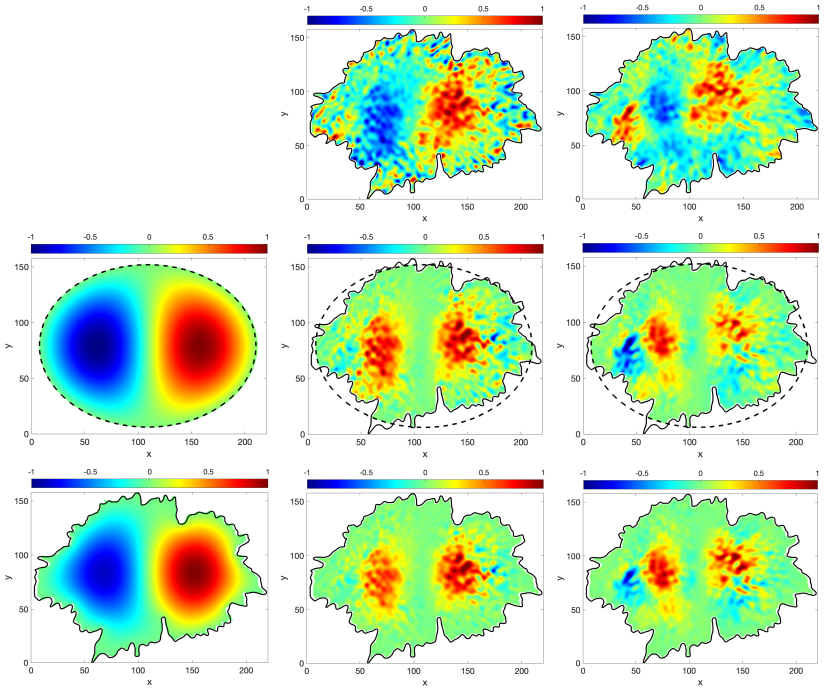

Figure 5.9: This figure displays the 14^{th} POD (top row, left panel) and DMD modes (top row, right panel) with a frequency of 5.8 mHz which has the azimuthal symmetry corresponding to the fundamental slow body kink mode.

stant values of the temperature, density, pressure, and magnetic field inside the magnetic flux tube. In reality the magnetic flux tubes are inhomogeneous in the transversal direction (see, e.g. observations of intensity provided by high-resolution observations by, to name but a few, Gopalakrishnan et al. (2013) and Fritts et al. (2017)). Furthermore, in the theory of guided MHD waves (see, e.g. Edwin and Roberts (1983)) modes are monochromatic and the lower order MHD wave modes have a lower frequency than higher-order modes, however, this holds true only when the wavenumber, k_z, is constant. In the family of identified modes in this chapter, there are some higher-order modes having a lower frequency than the lower-order modes, however, they have different wavenumber, as shown in Table 5.1 and 5.2.

One advantage of using the POD and DMD techniques for the identification of MHD modes in sunspot is the opportunity to detect a high number of MHD wave modes in one single sunspot, as these techniques provide a number of modes equal the number of snapshots of the data set. The challenge is, however, to select and identify those modes that are physical. Other techniques have their own limitation in identifying MHD waves in a sunspot. For example, the limitation of Fourier filtering is that it applies a wide range of bandpass filter. In the case of the circular sunspot, our analysis by using POD and

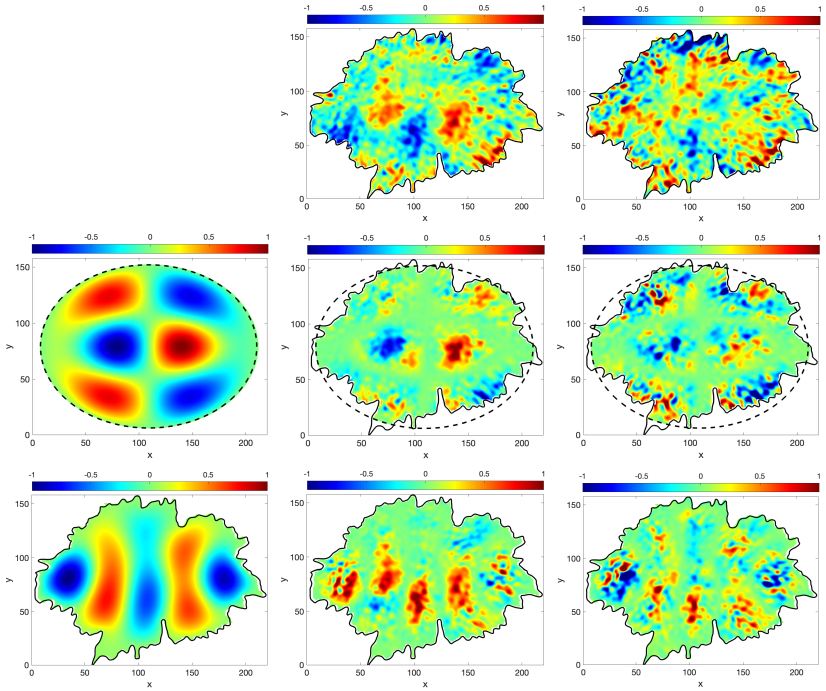

Figure 5.10: This figure displays the 30^{th} POD (top row, left panel) and DMD mode (top row, right panel) with a frequency of 5.3 mHz, which has an azimuthal symmetry of the slow body kink overtone mode.

DMD have identified the fundamental slow body kink mode with a frequency of 5.88 mHz and the slow body sausage overtone with a frequency of 5.61 mHz. However, in the original analysis by (Jess et al., 2017), using the same sunspot they applied a $k-\omega$ Fourier filter ($0.45-0.90$ arcsec^{-1} and $5-6.3$ mHz) that resulted in the identification of only the slow body kink mode. In general higher order modes cannot be detected, and this can be attributed to the fact that these modes have less energy than the fundamental modes, so it is expected that the spectrum is dominated by the fundamental modes. The POD and DMD techniques are able to address this shortcoming.

Figures 5.14 (for the circular sunspot), and 5.15 (for the elliptical sunspot), illustrate the ability of the POD technique to capture the portion of the umbral oscillations that are due to MHD wave modes among the observed intensity fluctuations. The top panel displays the POD time coefficient for the five detected MHD wave modes within a given time interval: 1000 seconds for the elliptical sunspot and 2016 seconds for the circular one. The lines and circles are color coded by the MHD wave mode, and the position of the circles indicate the value of time used for the plots in the bottom panels. The bottom left panels show the 3D surface representation of the original sunspot oscillations, while in the right panels we see the reconstructed oscillations using the POD

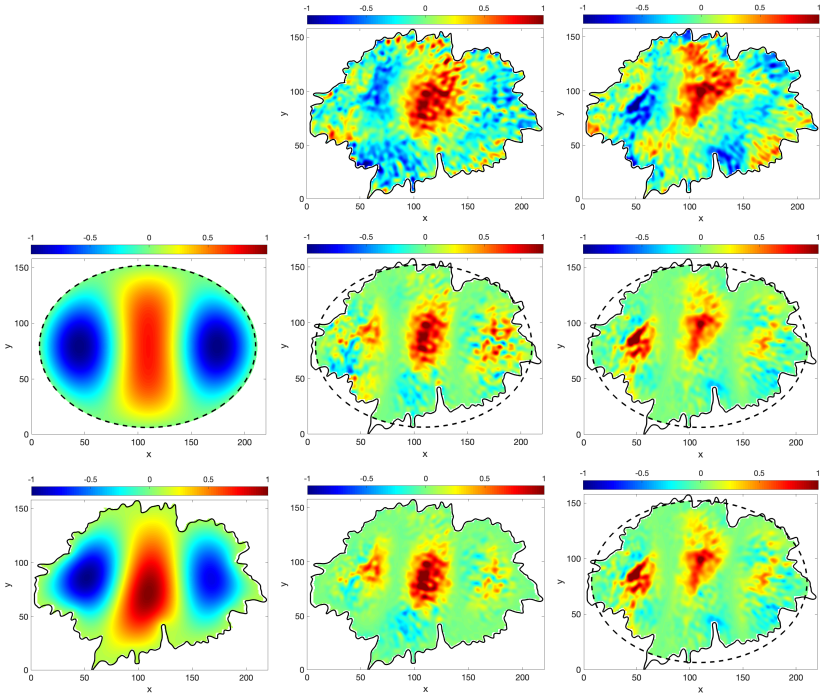

Figure 5.11: This figure displays the 13^{th} POD (top row, 1st panel) and DMD mode (top row, 2nd panel) with a frequency of 5.6 mHz, which has an azimuthal symmetry of the slow body fluting mode ($n = 2$).

modes identified as MHD wave modes. The POD technique separates the effects of oscillations that are due to wave propagation, enhancing the expected wave pattern in the umbra. An animated movies for Figures 5.14 and 5.15 can be found in Albidah et al. (2022). The analysed sunspots present a considerable discrepancy for the values of the time coefficients as the dynamics of the spatial modes changes considerably for different umbra geometry and size. Although there is a considerable difference between the POD reconstructed oscillations intensity and the original perturbations, this discrepancy is expected as the POD modes have less energy than the other "non-physical" modes detected by POD. The low contribution of wave propagation to the observed oscillations may be a consequence of different reasons (i.e. global modes, locally excited fluctuations) to the global variance of the oscillatory field in a sunspot. This reinforces the POD as a valuable tool to apply to wave detection in sunspot as other methodologies require properly filtering the data in order to disentangle and detect the resonant modes.

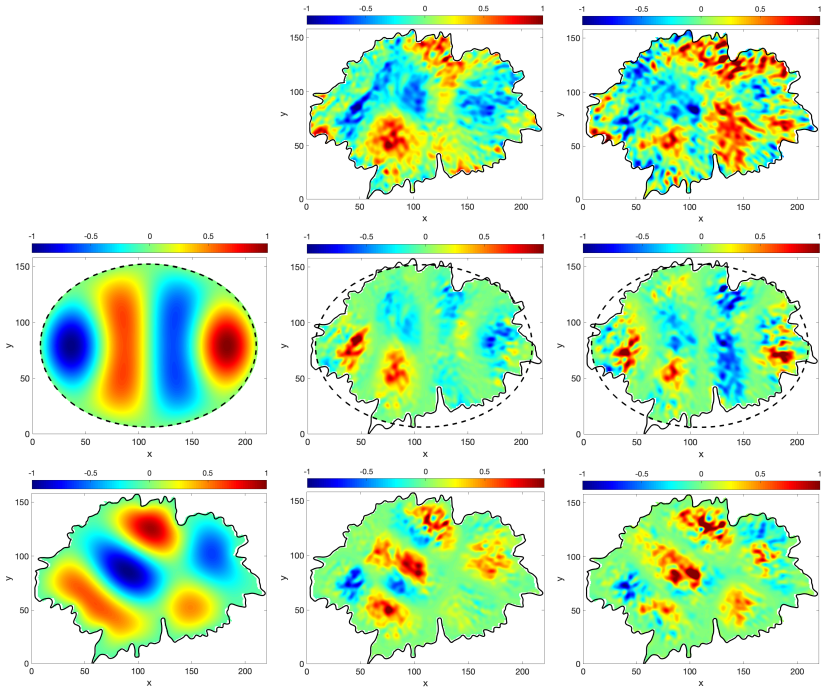

Figure 5.12: This figure displays the 18^{th} POD (top row, 1st panel) and DMD mode (top row, 2nd panel) with a frequency of 6.2 mHz, which has an azimuthal symmetry of the slow body fluting mode ($n = 3$).

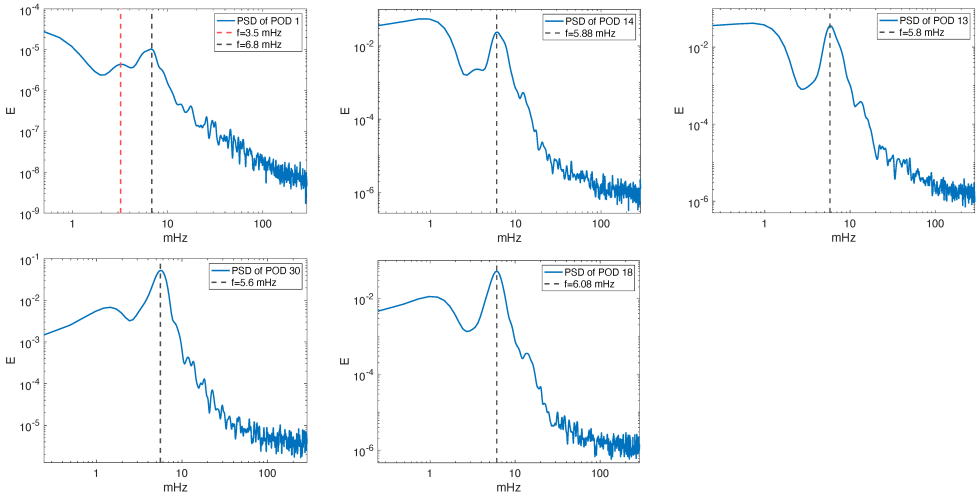

Figure 5.13: This figure shows the power spectrum density (PSD) of the time coefficients of the POD 1 (upper left panel), POD 14 (upper middle panel), POD 13 (upper right panel), POD 30 (bottom left panel) and POD 18 (bottom middle panel) modes. The coloured-dash vertical lines represent the value in the frequency domain that corresponds to the peaks of the PSD, where the frequencies are shown in the legend.

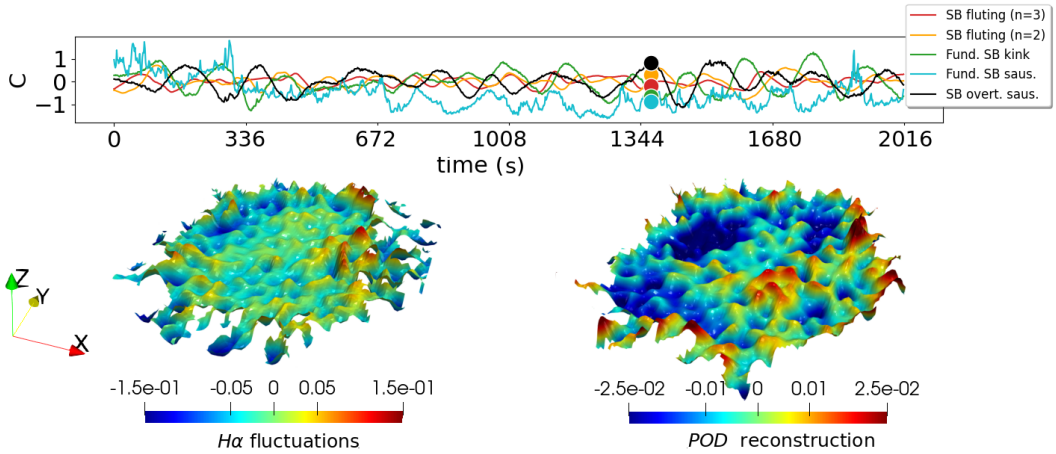

Figure 5.14: Intensity fluctuations in the circular sunspot. The top panel shows the time coefficient, C, for the POD modes identified as MHD waves: slow body (SB) sausage overtone, SB fundamental sausage, SB fundamental kink, SB fluting ($n = 2$), SB fluting ($n = 3$). The colors of the lines and circles depict the detected MHD wave modes and the position of the circle indicates the time used for the plots in the bottom panels. The left bottom panel presents a 3D surface plot of the umbra where the z-direction describes the oscillations in the Hα observations and it is colored by the observed intensity fluctuations. The right bottom panel is the 3D surface of the POD reconstruction of the intensity fluctuations using only the POD modes identified as MHD waves. The video of this 3D visualisation can be found in Albidah et al. (2022)

.

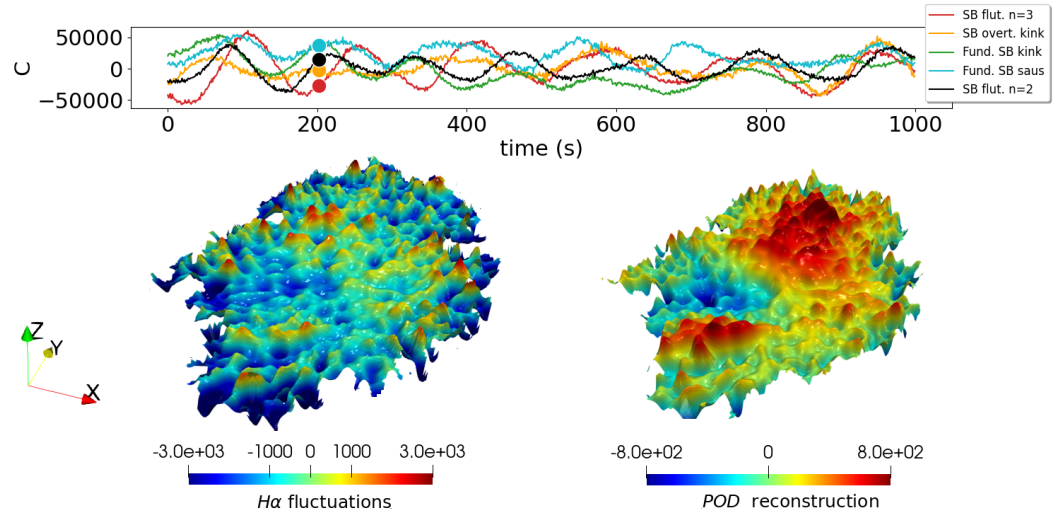

Figure 5.15: The same as Figure 5.14, but here the intensity fluctuations in the elliptical sunspot for the POD modes identified as MHD waves: slow body (SB) fluting ($n = 2$), SB fundamental sausage, SB fundamental kink, SB overtone kink, SB fluting ($n = 3$).The video of this 3D visualisation can be found in Albidah et al. (2022)

.

MHD wave mode	$\tilde{m}_0$	f (mHz)	k_z (Mm^{-1})	λ (Mm)	V_{ph} (km/s)
Fundamental slow body sausage	1.1644	3.5	2.24887	2.7939	9.77
Fundamental slow body kink	1.6368	5.88	3.7696	1.6667	9.80
Slow body overtone kink	3.1698	5.3	3.412798	1.8410	9.75
Slow body fluting ($n = 2$)	2.6328	5.61	3.6166	1.7373	9.74
Slow body fluting ($n = 3$)	2.7837	6.2	3.995553	1.5725	9.74

Table 5.2: This table shows the summary of MHD waves' properties that were detected by the POD and DMD techniques in the sunspot with elliptical cross-section. The first column contains the type of the modes, and the value of the magneto-acoustic parameter, $\tilde{m}_0$, is shown in the second column (see Equation 2.39). The third column contains the frequency of waves, as determined from the DMD analysis. The fourth column contains the wavenumber along the vertical direction of the sunspot, and it is calculated using Equation 2.39, with $\omega = 2\pi f$, $c_0 = 10$ km s^{-1}, $v_A = 4c_0$ and $\sigma^2 = 0.4174$. The fifth column shows the wavelength ($\lambda = 2\pi/k_z$) of waves, while the last column contains the phase speed ($V_{ph} = f\lambda$) of waves.

5.4 Surface wave identification

The POD and DMD techniques can also be applied to identify surface modes. In the POD analysis performed on the circular sunspot it was found that there were two modes that have the characteristics of surface waves: the POD 10 mode (see the middle panel of Figure 5.18), which shows the azimuthal symmetry corresponding to the fundamental (slow or fast) surface sausage mode, and the POD 6 mode (see the middle panel of Figure 5.19), which has a pattern close to the fundamental (slow or fast) surface kink mode. Our theoretical model is restricted to the identification of slow body modes, i.e. modes corresponding to $v_z = 0$ at the umbra/penumbra boundary (see section 2.2.5). Therefore, in the framework of this study, cross-correlation with possible surface modes detected with POD/DMD and their direct theoretical counterparts cannot be performed. Nevertheless, the cross-correlation between the theoretical slow body and slow surface modes in a magnetic cylinder, produces a distinctive closed ring for the sausage mode and a broken ring for the kink mode, see Figure 5.16, with a clear in phase relationship. Moreover, the cross-correlation between the slow body mode and the fast surface mode also provides an in phase, but the spatial structure is very close to the slow body eigenmode shown in Figure 5.17. These distinctive signatures provide, at least, an indirect way of detecting slow and fast surface modes in the observational data.

The POD modes which appear most likely to be surface modes have been correlated with the fundamental slow body sausage and kink modes as shown in Figures 5.18 and 5.19, respectively. From Figure 5.18 (middle panel) the red ring is present indicating a slow surface sausage mode but the blue regions of anti-phase inside the red ring and on the outer left edge cannot be explained by the theoretical model. The anti-phase regions are even more prominent in Figure 5.18 (right panel) and are also not predicted for the theoretical fast surface mode. The cross-correlation for the POD 6 mode shows stronger agreement with a fast surface kink mode as shown in Figure 5.19, although there are still some small anti-phase regions which are not consistent with the theoretical model.

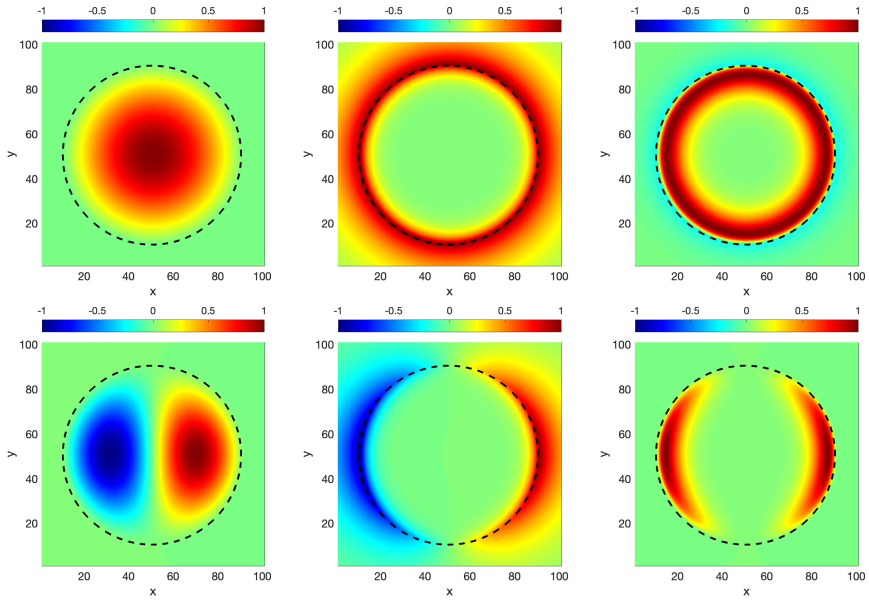

Figure 5.16: This figure shows the sausage mode (first row) and the kink mode (second row) of the cylindrical magnetic flux tube, where the first column shows the slow body mode, the second column shows the slow surface mode and the third column shows the cross-correlation between the first and second columns.

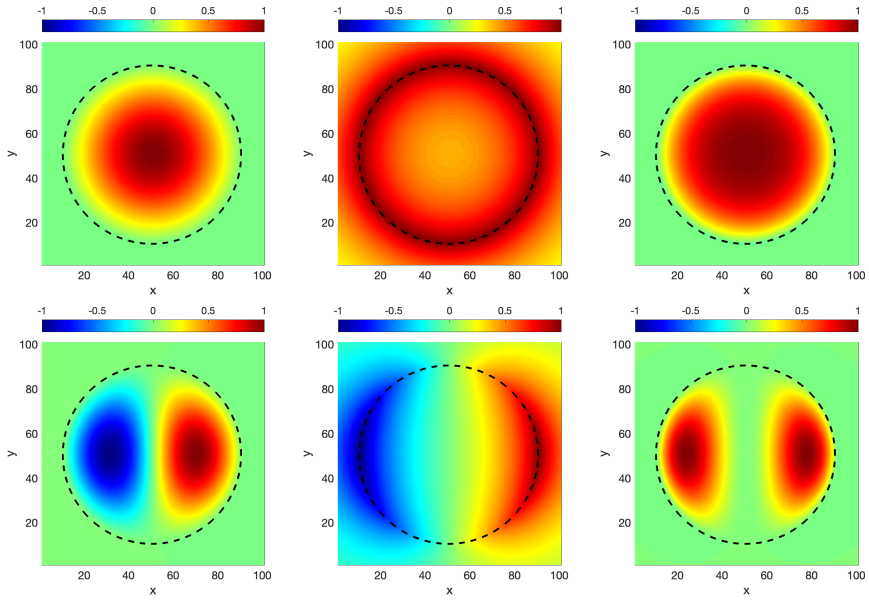

Figure 5.17: This figure shows the sausage mode (first row) and the kink mode (second row) of the cylindrical magnetic flux tube, where the first column shows the slow body mode, the second column shows the fast surface mode and the third column shows the cross-correlation between the first and second columns.

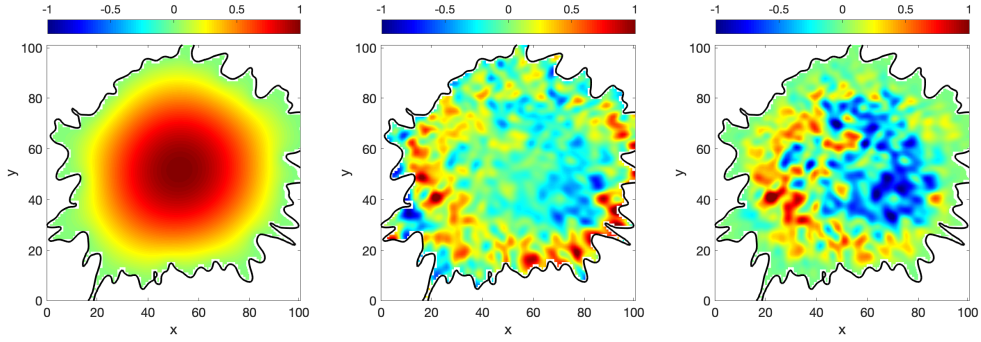

Figure 5.18: This figure shows the fundamental slow body sausage mode as shown above in Figure 5.2 (left panel), the spatial structure of POD 10 (middle panel) and the cross-correlation between the left panel and the middle panel (right panel)

.

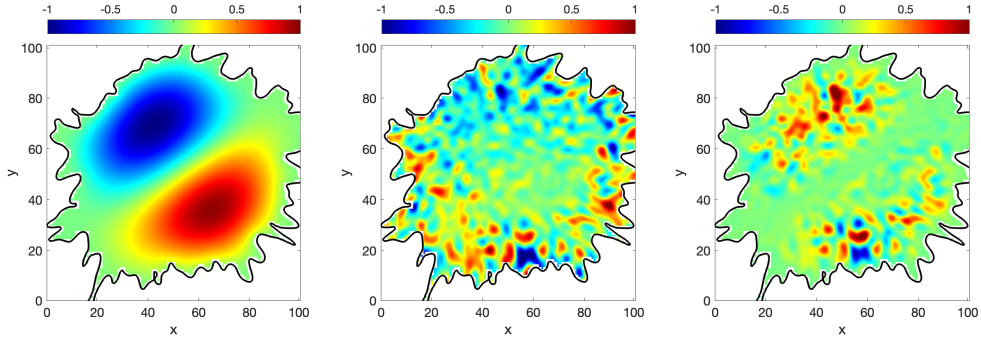

Figure 5.19: This figure shows the fundamental slow body kink mode as shown above in Figure 5.3 (left panel), the spatial structure of POD 6 (middle panel) and the cross-correlation between the left panel and the middle panel (right panel)

.

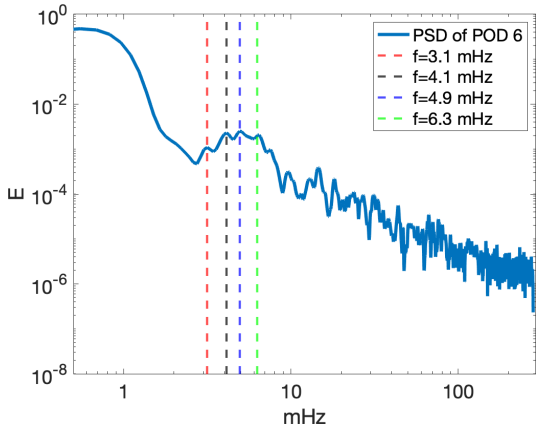

Figure 5.20: The power spectrum density (PSD) of the time coefficients of POD 6 mode.

5.5 Summary and Conclusions

The present chapter provided clear evidence of overtones to MHD sausage ($n = 0$) kink modes ($n = 1$) and higher order ($n \geq 2$) fluting modes in sunspots. The results obtained are significant extension of the previous studies by Jess et al. (2017) and Albidah et al. (2021) where MHD modes were recovered for the case of an approximately circular sunspot. Firstly, the mode detection was carried out by means of the POD and DMD techniques. Our results were compared with their theoretical counterparts obtained assuming a cylindrical magnetic flux tube model, as well as with the model of the magnetic flux tube of irregular shape that corresponds to the actual shape of the umbra boundary.

Secondly, the same techniques were further applied to a sunspot whose shape is close to an elliptical cross-section and compared the obtained results with the theoretical predictions of waves elliptical waveguide, as well as a irregular shape magnetic flux tube (that correspond to the actual shape of the umbra boundary). The comparison between modes detected in observational data and in theoretical models has been carried out by means of cross-correlation analysis calculated on a pixel-by-pixel basis. Correlation results evidence that the higher order MHD modes are more strongly affected by the sunspot shape. The correlation also shows that the detected modes have a much better correlation in the case of a sunspot with irregular shape than a sunspot with elliptical cross-section. The vertical wavenumber, k_z, and modes frequencies have been calculated by using magneto-acoustic wave parameter (m_0) and Equation 2.24 for sunspot with a circular cross-sectional shape (Equation 2.39 for the sunspot with an elliptical cross-sectional shape), see Tables 5.1 and 5.2.

The existence of these MHD waves were theoretically predicted almost 40 years ago (see, e.g. Edwin and Roberts, 1983), so our study offers probably one of the first observational evidence for the existence of higher order modes in the chromosphere. Only few papers reported their observational presence (see, e.g. Yuan, 2015; Kang et al., 2019; Stangalini et al., 2022). These waves offer an unprecedented diagnostic tool for describing the dynamical state of the plasma and the structure of the magnetic field since they are carrying information about the medium in which they are propagating and seismological techniques can be applied to compare observationally determined quantities with theoretical predictions to infer values that cannot be (directly or indirectly) measured. Seismology using a single wave is a sort of "under-determined" system, because many variables are implicit and the variables that can be extracted are not in-

dependent (similar to a system of equations having $n \geq 2$ variables, but only $n-1$ equations are given). The observation of at least two or more modes in the same structure helps resolve this degeneracy.

Concurrent observations of different kinds of waves (including higher order modes presented in our study) could allow us to more fully understand the true nature of the dynamics and comprehensively describe the plasma state and structure of the magnetic field. Potentially, our results could help us better understand the nature and properties of modes in more realistically structured waveguides, where the sound and Alfvén speeds are spatially varying, which would modify the eigenvalues and eigenfunctions, especially of the higher-order modes.

Higher order modes also give a more complete description of sub-surface driver. It is clear that in the present situation we are dealing with a broad band driver. However slow body modes are weakly dispersive and their phase speeds are confined to a narrow band between the tube speed and internal sound speed. This means that a helioseismological approach of exploiting detected p-modes, where modes in $\omega - k$ space correspond to distinct clear ridges, would certainly be a challenge.

In addition, due to the presence of the higher order modes (as these are the most sensitive to the shape of the waveguide), we demonstrated that the using the exact cross-sectional shape of the waveguide is essential for the correct interpretation of waves.

CHAPTER 6

Temporal evaluation of MHD waves in a sunspot

6.1 Introduction

The studies presented in previous chapters assumed that the umbral boundary is not changing. However, extended high resolution observations show that the boundary between a sunspot umbra and its penumbra is not stationary, instead its shape can change in time. The results presented in previous chapters also show that higher order modes are sensitive to the shape of the flux tube, therefore we expect that identified modes will show changing properties in time. In this Chapter we consider the effect of umbral boundary change on the oscillatory pattern of waves and their properties.

To evidence the effect of changing the shape of the flux tube in time on the nature and properties of waves, we will divide a long time period Doppler velocity measurements of a sunspot with a circular cross sectional shape into subdata-sets, T_i, where $i = 1, ..., 10$ is the number of the time intervals. Next, we will apply the POD and DMD on every single subdata-set to detect and track the appearance of various MHD waves and the change in their morphology with the change in the shape of the waveguide. The oscillatory patterns of the observed modes are then compared with the predictions of the irregular shape model that correspond to the shape of the sunspot (see section 2.2.5).

6.2 Observation

Continuum intensity and Doppler velocity measurements of the active region NOAA 11366 were obtained from observations by the Helioseismic and Magnetic Imager (HMI; Schou et al., 2011) onboard the Solar Dynamics Observatory (SDO; Pesnell et al., 2011). The active region contain a sunspot with a circular cross sectional shape. The data were acquired from 15:00–18:00 UT

on 2011 December 10. The time cadence of the measurements was 45 s, which provided 241 images (with time period of $\sim$ 3 hours) for both the continuum intensity and the Doppler velocity. The spatial sampling products was $0''.504$ per pixel, which is approximately 356 km on the surface of the Sun.

To account for the rotation of the Sun relative to SDO spacecraft, the observation was reprojected to the reference frame of Earth-based observer at 15:00 UT, on 2011 December 10 using version 3.0.0 (Mumford et al., 2021) of the SunPy open source software package (The SunPy Community et al., 2020). The pixel values of each image are mapped to the new projection and interpolated using a nearest neighbor algorithm. The motion of the center of the Sun is ignored such that coordinates are always relative to the center of the Sun.

6.3 Analysis and Results

The main additive of the present chapter is that the umbral boundary is changing with time, and this can be captured in the long period (3 hours) observation. Therefore, the time series is divided into equal sub-datasets to which we apply the techniques of POD and DMD.

Accordingly, the time series of the continuum intensity and the Doppler velocity are divided into 10 time intervals (T_i), where $i = 1 \ldots 10$, such that every time interval contains 50 images ($\sim$ 37.5 minutes) and overlapped with the previous time interval by 20 images, i.e. the initial time of T_{i+1} is after the initial time of T_i by 20 images ($\sim$ 15 minutes). Then, we have taken the mean of the continuum intensity time series for every time intervals and then we have applied the intensity threshold level at 0.45 to construct the boundaries between the umbra and penumbra. For each time intervals, the umbral boundary will have a different shape, as shown in Figure 6.1, as a representative example of three different time intervals.

To obtain the theoretical modes that corresponds to the shape of the umbra, for every time interval, we have used the model that corresponds to the realistic shape of the umbra, which has been described earlier in section 2.2.5. As a result of that, the MHD wave modes, for every time interval, are shown in Figures 6.2, where each column represent a theoretical mode. It is clear that while the lower order, fundamental modes show a fairly constant morphology, the spatial structure of the higher-order modes are changing in time, with the change in the shape of the sunspot.

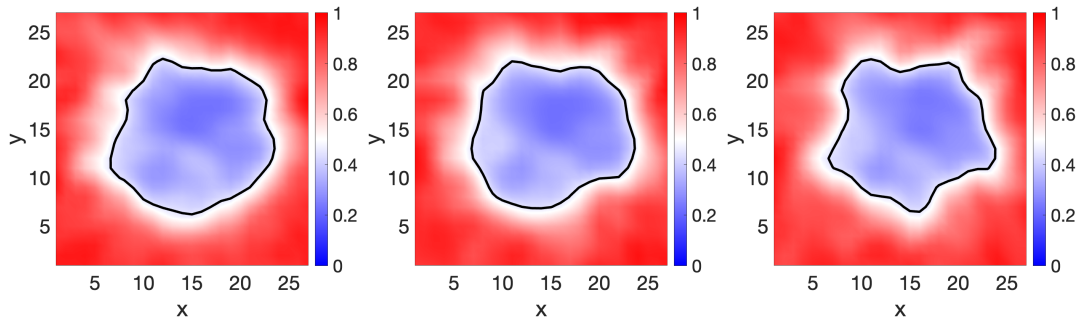

Figure 6.1: This figure shows the mean of the continuum intensity time series for three different time intervals of the data time series of the observed sunspot. The time intervals that are displayed, from left to right, are T_1, T_5 and T_{10}. The colourbar displays the magnitude of the mean time series for each time interval, and the solid black line shows umbra/penumbra boundary by taking threshold level at 0.45. The spatial scale is given in pixels (one pixel has a width of 0.504″, which is approximately 356 km on the surface of the Sun).

Next, the POD and DMD techniques were applied to every time intervals of the original data-sets. The spatial structure of the first 10 POD modes, for each time interval is shown in Figures 6.3. This step is followed by applying the cross-correlation analysis, for every time interval, investigating the correlation between the first 10 POD modes and the models, and then we take the integral of the correlations, defined as the summation of the pixels in the correlation matrix (see Appendix A.2 for more explanation). The integrated correlations are shown in the Appendix in Figure A.1. We should mention that the POD and DMD modes are interpolated to have the same size as the model since the cross-correlation analysis is calculated on a pixel-by-pixel basis.

This step is taken as guideline to observe and avoid missing the higher correlations as we have too many modes of the POD analysis and the model at every time interval. However, these higher correlations need to be checked and validated in order to be considered. Finally, the power spectrum of the time coefficient that corresponds to the selected POD modes are calculated to obtain the dominant frequencies. This is followed by obtaining the spatial structure of the DMD modes that correspond to the dominant frequencies.

To discuss and analyse the observed MHD wave modes, we have selected some of the modes that have a good agreement with the theoretical modes, i.e. having highest correlation from Figure A.1. All possible observed modes that show a good correlation with the theoretical models are presented in Table 6.1. It is remarkable the observed fundamental modes have a lower POD order number as the first and the second POD mode, which means the observed

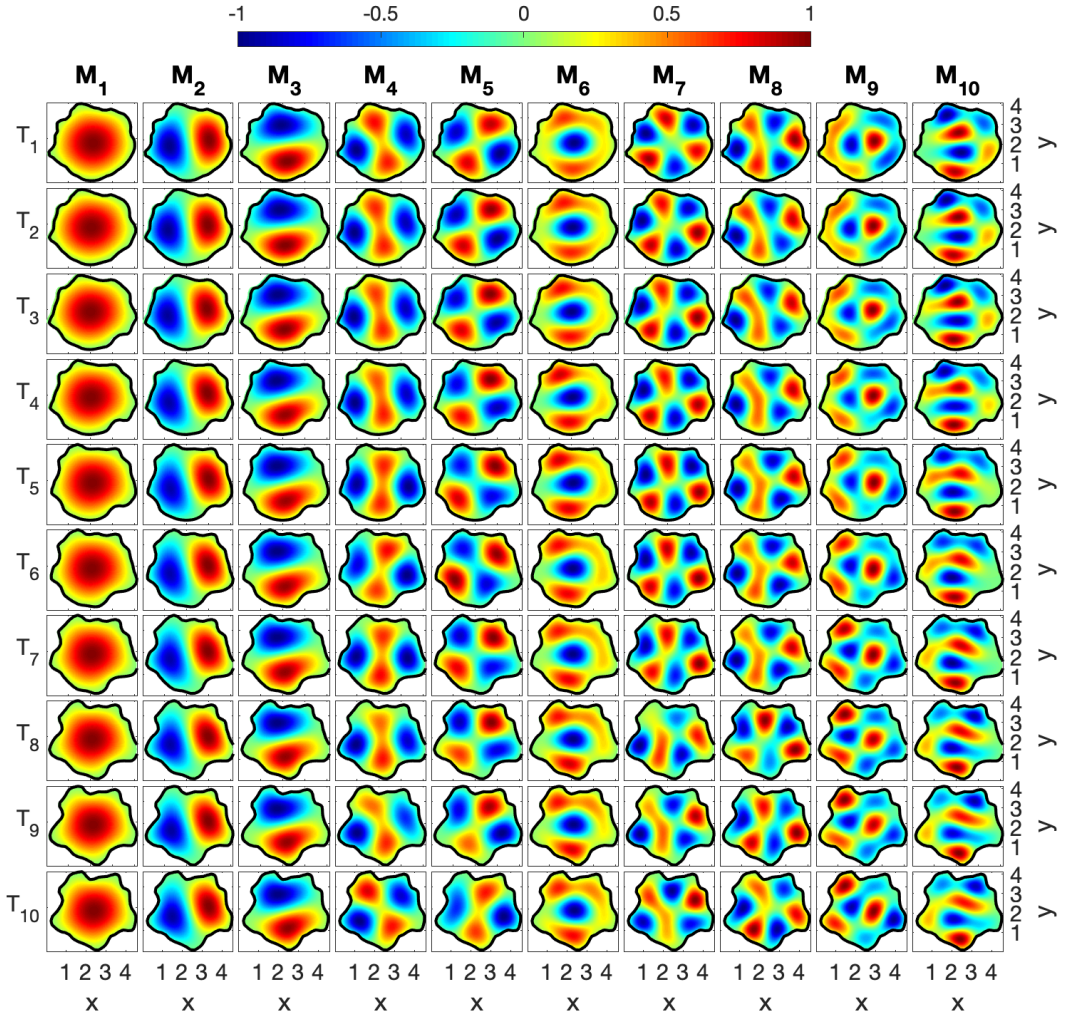

Figure 6.2: The theoretical morphology of slow body modes that correspond to the changing shapes of the observed sunspot. Every row shows the spatial structure of the models at different times and changing shape. Columns represent different types of slow body modes, and they are labelled by M_i, where $i = 1, \ldots, 10$. In particular, M_1 stands for the fundamental sausage, M_2 and M_3 denote the fundamental kink, M_4 and M_5 are showing the fluting ($n = 2$), M_6 is showing the sausage overtone, M_7 and M_8 are showing the fluting ($n = 3$) and the last two columns (M_9 and M_{10}) are showing the kink overtone.

MHD wave modes have the highest contribution to the total variance of the signal.

The first MHD wave mode that was observed is the fundamental slow body sausage mode, and it appears as the first POD mode in the time intervals from T_5 up to T_7 as shown in Figure 6.3, while it has a lower contribution in T_3 and T_4, where it appears as the 4^{th} POD mode. In Figure 6.4 we show the fundamental slow body sausage mode in two time intervals (T_6 and T_7) and the spatial structure of the DMD mode that correspond to the dominant frequency

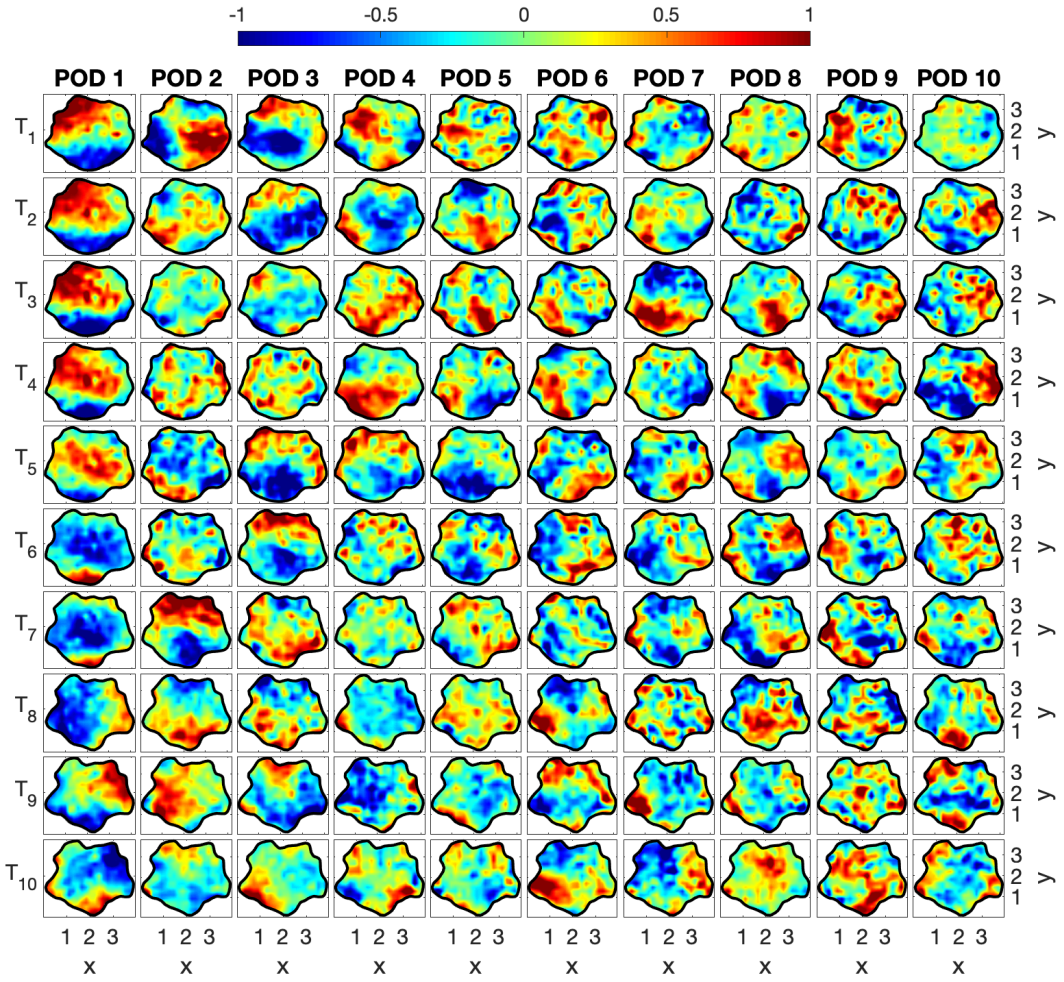

Figure 6.3: This figure represents the first 10 POD modes of the sunspot data set, Every column shows a POD mode and the rows shows how the modes are changing along the time intervals, T_i, of the data time series. Every time interval contains 50 images, and has a duration of 37.5 minutes. Every time interval is shifted by 20 images, i.e. the initial time of T_{i+1} is after the initial time of T_i by 20 images, corresponding to 15 minutes.

of the time coefficient of the POD modes. These DMD modes correspond to 3 mHz, in T_6, and 4.3 mHz, in T_7, respectively.

The second MHD wave mode that we have observed has an azimuthal asymmetry of a fast surface kink mode and it is shown in Figure 6.5. These modes have the pattern corresponding to surface waves, as the magnitude increases along the radial direction and reaching its maximum at the boundary. Due to the limitation of the model describing waves in a waveguide with, the modes that can be theoretically determined are only the slow body modes, i.e. modes corresponding to $v_z = 0$ at the umbra/penumbra boundary (see section 2.2.5). Hence, the cross-correlation with possible surface modes detected with

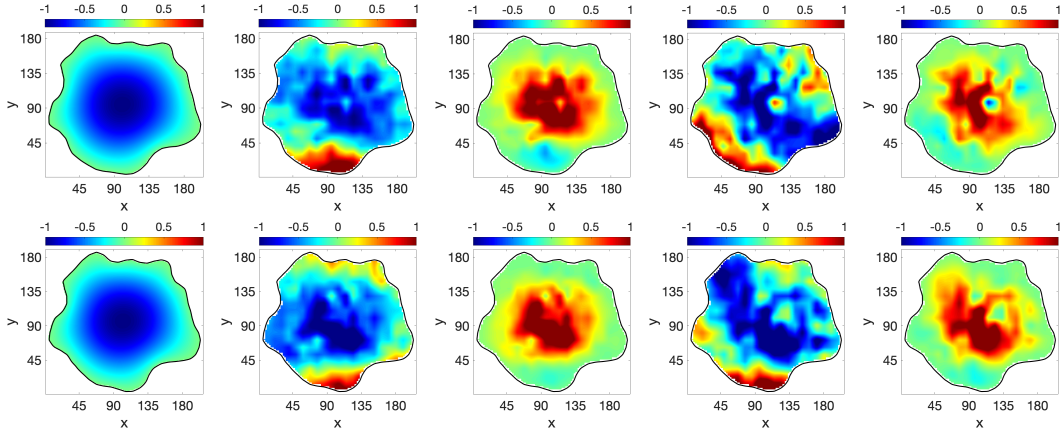

Figure 6.4: Here rows correspond to different time interval (T_i), where T_6 (top panels) and T_7 (bottom panels). The first column displays the theoretical spatial structure of the fundamental slow body sausage mode determined by means of the irregular shape model. The second column displays the spatial structure of the 1^{st} (top and bottom) POD modes. In the third column we show the cross-correlation between the model and the determined POD mode . The fourth column displays the spatial structure of the DMD modes corresponding to 3 mHz (top) and 4.3 mHz (bottom). Finally, the last column contains the cross-correlation between the model (first column) and the DMD mode (fourth column). The solid black line shows the umbra/penumbra boundary. The same configuration was used for Figures 6.5 and 6.6.

POD/DMD and their direct theoretical counterparts cannot be performed. However, it was shown earlier in section 5.4, in the cylindrical magnetic flux tube model, the cross-correlation between the slow body mode with the fast surface mode provides a spatial structure with a pattern closed to the slow body mode. In contrast, the cross-correlation between the slow body mode and the slow surface mode produces a spatial structure closed to a ring for the sausage mode and a broken ring for the kink mode.

Therefore, the correlation in Figure 6.5 between the slow body modes and the observed modes show a pattern closed to slow body modes, hence we can identify this mode as being a fast surface kink. The modes that are presented in the first and second row of the second and fourth columns of Figure 6.5 are the 1^{st} and the 2^{nd} POD modes and the DMD modes corresponding to 3.4 and 3.1 mHz, respectively, at T_1. The superposition of these two approximately perpendicular kink modes with close frequencies can provide an apparent rotational motion. The mode that is presented in the third row of Figure 6.5 is the 2^{nd} POD and DMD mode corresponding to 3.9 mHz at T_7.

It is clear from Figure 6.3 the mode that has the highest contribution (i.e. the mode with highest power) to the total variance of the signal is the fast

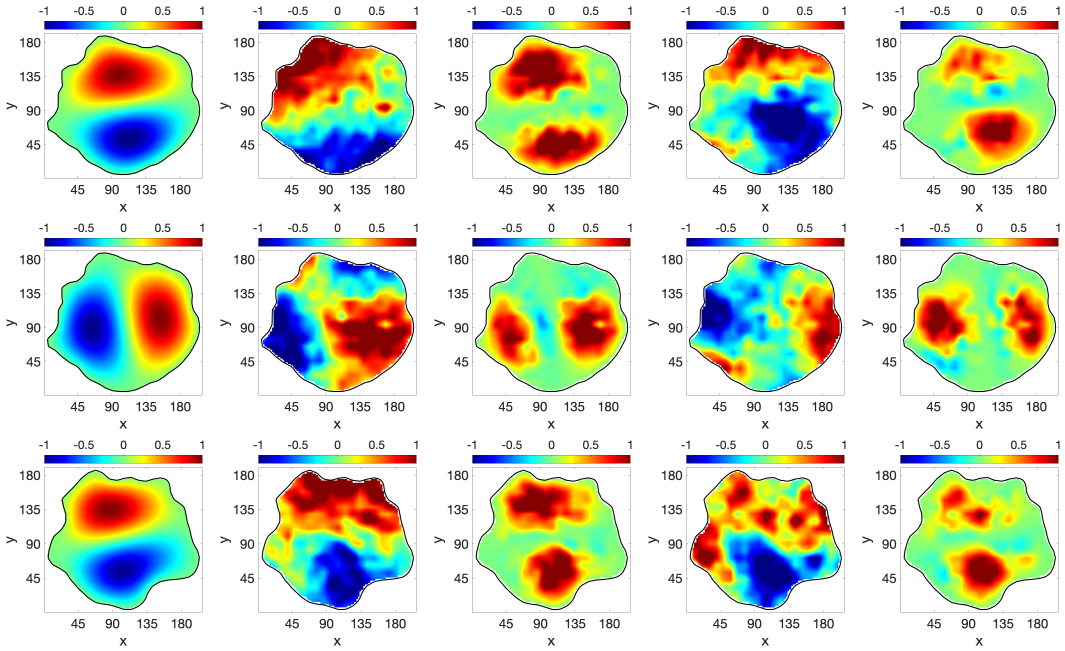

Figure 6.5: The same as Figure 6.4, but here the first row shows the 1^{st} POD mode and the spatial structure of the DMD mode corresponding to 3.4 mHz at T_1. The second row shows the 2^{nd} POD mode and the spatial structure of the DMD mode corresponding to 3.1 mHz at T_1. The third row shows the 2^{nd} POD mode and the spatial structure of the DMD mode corresponding to 3.9 mHz at T_7. The first column shows the fundamental slow body kink mode that corresponding to T_1 (top and middle) and T_7 (bottom).

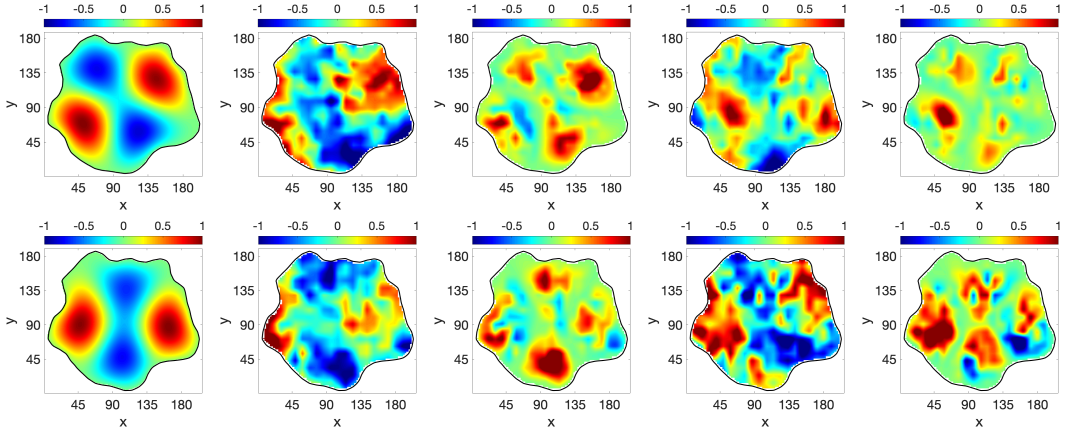

Figure 6.6: The same as Figure 6.4, but here the first row shows the 8^{th} POD mode and the spatial structure of DMD mode corresponding to 4 mHz at T_6. The second row shows the 7^{th} POD and DMD mode corresponding to 3 mHz at T_7. The first column shows the slow body fluting (n=2) corresponding to T_6 (top) and T_7 (bottom).

surface kink mode from T_1 to T_3. Starting from the time set T_5 the dominant wave in the studied waveguide becomes the slow body sausage mode up to T_7.

Furthermore, Figure 6.7 shows that the contribution of the first POD mode to the total variance of the signal is decreasing sharply up to the fourth time interval, and that could be due to a very effective damping of the fast surface kink mode (or mode conversion). At the same time, as shown in table 6.1, the frequency of the fast surface kink mode (the first POD mode at the first 3 time interval) is increasing.

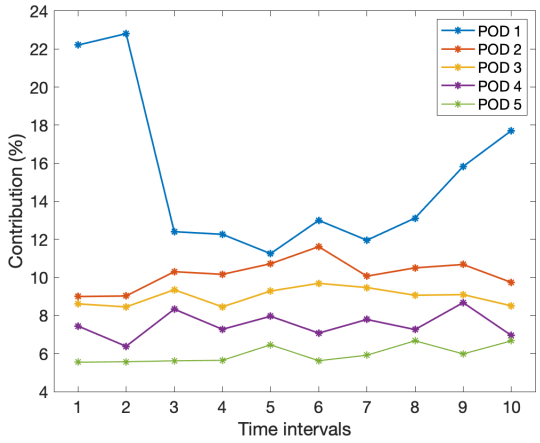

Figure 6.7: This figure shows the contribution of the first 5 POD modes to the total variance of the signal along the considered time intervals (T_i).

The fast surface kink mode is still present in the remaining time intervals, as shown in Figure 6.3, but with a lower contribution as this mode becomes the 3^{rd} POD mode at T_5 and T_6 and the 2^{nd} POD at T_7. The last MHD wave mode that we have observed in the circular sunspot is the slow body fluting mode ($n = 2$), which appears at T_6 and T_7 (see Figure 6.6). The first row of Figure 6.6 shows the 8^{th} POD and DMD modes corresponding to 4 mHz at T_6. The second row of this figure shows the 7^{th} POD and DMD modes corresponding to a frequency of 3 mHz at T_7.

In addition, given the far from ideal spatial resolution of the HMI instrument, it is likely that some significant information on the dynamics within the sunspot cannot be acquired. As a result, there could be other higher order modes or further overtones that cannot be identified via the POD/DMD techniques. Nevertheless, POD/DMD have shown their ability to identify the higher order modes and overtones for observations that have a much better spatial resolution, e.g. the Hα time series presented in previous Chapter 5.

The above analysis constitute a first step in the complex identification of waves in sunspots whose shape is changing in time. The information we got so far gives a very cumbersome picture, where different kinds of waves, all with different frequencies, are present in a sunspot at the same time. The diagnos-

M_i	T_i	POD	peaks of PSD [mHz]	DMD [mHz]	MHD mode observed
M_1	T_3	4	3.5 and 4.4	3	FSB sausage
M_1	T_4	4	3.5 and 4.4	3.4	FSB sausage
M_1	T_5	1	3.5 and 4.8	3.6	FSB sausage
M_1	T_6	1	3.1 and 4.8	3.04	FSB sausage
M_1	T_7	1	3.5 and 4.4	4.3	FSB sausage
M_2	T_1	2	4	3.1	FFS kink
M_3	T_1	1	3.5	3.4	FFS kink
M_3	T_2	1	3.5	3.2	FFS kink
M_3	T_3	1	2.6 and 4	4.22	FFS kink
M_3	T_5	3	3.1 and 4.4	4.23	FFS kink
M_3	T_6	3	3.1 and 4.4	3.44	FFS kink
M_3	T_7	2	3.1 and 4.4	3.9	FFS kink
M_4	T_7	7	3.5 and 4.8	3	SB fluting ($n = 2$)
M_4	T_8	6	3.5 and 4.4	3.17	SB fluting ($n = 2$)
M_5	T_6	8	3.5	4	SB fluting ($n = 2$)

Table 6.1: A summary of all possible MHD modes that identified in the observed sunspot along the time intervals. The first column represents the theoretical mode and they are labelled according to the Figure 6.2. The second column shows the time interval of the sub-data in which the mode was observed. The POD mode numbers are presented are displayed in the third column, similar to Figure 6.3. The fourth column contains the frequencies (in mHz) corresponding the peaks in the power spectrum density (PSD) of the time coefficient of the POD mode. The fifth column shows the frequency (in mHz) corresponding to the DMD mode. Finally, the last column displays the MHD wave mode that the POD mode and DMD mode have a good agreement with. Here the abbreviations FSB, FFS and SB stand for fundamental slow body, fundamental fast surface and slow body modes, respectively.

tics of morphology and properties of waves becomes even more complicated due to a continuous change in the modes' contribution to the overall signal.

The results showing the contribution of modes to the overall signal (see Figure 6.7) also can shed light on the driver of these modes and it clear that these modes seem to be driven by various drivers, many of them driven continuously, with different timescale. Equally, the analysis presented here offers the possibility to gain essential information about the attenuation of waves.

6.4 Summary and Conclusion

In the current chapter, we have assumed the shape of the umbral boundary on a dataset of long period (3 hours) is change with time, while in the previous

chapters the shape was assumed to be constant. The dataset was divided into 10 overlapped sub-dataset, T_i. The techniques of POD/DMD were applied for every T_i as shape is changing with time. Our observed modes were compared with the theoretical model of magnetic flux tube that corresponds to the realistic shape of the umbra at every T_i. The comparison was calculated on a pixel-by-pixel basis of the cross-correlation analysis.

We have shown the alternation of having the highest contribution to the signal between the fast surface kink mode and the fundamental slow body sausage mode. Moreover, we have shown the diminution of the fast surface kink contribution to the signal. In addition to the slow body sausage and the fast surface kink mode, the fluting ($n = 2$) mode was observed.

We have concluded that, the preeminent time intervals to assess the impact of changing umbral shape on observed MHD, based on our analysis in the sunspot, is 37 minutes. This estimate, however, will vary based on the sunspot that considered in the analysis and the observation instrument's temporal and spatial resolution. Hence, our research demonstrates that statistical analysis of more sunspot data sets, particularly those with more complicated forms and evolutionary behaviour than the examples presented here, is required.

CHAPTER 7
Conclusions

The research presented in the present Thesis discusses the possibility of using the combined POD and DMD techniques for solar observations, to identify MHD modes in sunspots. Up to our knowledge, this is the first time when these techniques were applied in conjunction with solar datasets. The combination of the these techniques have also shown for the first time the presence of *five* different MHD wave modes in a sunspot, simultaneously, including overtone modes and fluting modes.

A correct and accurate detection of waves in solar magnetic waveguides allows a much better diagnostic capability of the plasma and magnetic field using techniques similar to the seismology of the Earth. Here observational information (amplitude, frequency, wavelength, damping time and length, etc.) can be combined with theoretical results (dispersion relations, evolutionary equations, etc.) to obtain quantities that cannot be measured directly or indirectly (magnitude and structure of the magnetic field, transport coefficients, densities, ionisation degrees, etc.).

After a brief historical overview of solar studies, we described the structure of the Sun and a few features that appear on the solar surface and they are relevant to our purpose (i.e. sunspot, coronal loop etc.). Since the Thesis deals with waves in sunspots, a review of the observational results discussing waves and oscillations in sunspots was presented.

The physical framework of MHD and the governing equations was discussed in details, together with their wave solutions in an unbounded, unstructured and homogeneous plasma environment. In reality, waves in the solar atmosphere propagate guided, confined to magnetic structures, therefore an overview of guided waves in various magnetic structures were presented, together with the dispersion diagrams of waves propagating in structures as magnetic slabs and cylinders. Waves were classified according to their speed (slow and fast magneto-acoustic modes), their symmetry with respect to the

symmetry axis of the magnetic structures (sausage, kink, fluting) or the oscillatory pattern of waves in the transversal direction (body, surface). The dispersion curves obtain as solutions of the dispersion relations allowed us to correctly identify the observed waves and study their properties.

Given that the present Thesis revolves around the application of the POD and DMD techniques for mode identification, we described in details the mathematical background of these techniques and presented their applicability (for the purpose of validation) on a set of synthetic numerical data, as a test case. Our results showed that the POD and DMD techniques are indeed suitable methods to decompose signals, with truly remarkable accuracy.

The original research carried out in the present Thesis involved the application of these techniques on real observational datasets from sunspots with the purpose to identify the nature and properties of waves propagating along sunspots. In what follows we are going to summarise and discuss the results of our analysis, presenting a few pathways along which our research can be continued.

7.1 Summary of results

7.1.1 Chapter 3

In this Chapter, POD and DMD were applied on a synthetic numerical dataset generated by combining five different modes propagating in cylindrical magnetic flux tube. To evidence the true power of the techniques and their capabilities, two of the modes were chosen to have the same frequency. This step was considered as a test case, before applying them on real sunspots data, to prove whether these techniques can help recovering every single mode or not. Consequently, POD managed to detected all the five MHD wave modes. This result can be easily explained since the POD decompose modes in terms of their orthogonality in space, and the governing functions on the radial direction of the theoretical modes are the Bessel functions, which are orthogonal to each other. On the other hand, the DMD detected only four modes. Since DMD identifies the temporal orthogonality, it cannot decompose the modes having the same frequency, instead it identifies the mode that is formed as the superposition of the two modes that share same frequency.

7.1.2 Chapter 4

The POD and DMD were applied on a sunspot that has an approximately circular cross-sectional shape. The sunspot has been recently analysed by Jess et al. (2017), and they have detected the rotational motion of the fundamental slow body kink mode by implementing a $k - \omega$ Fourier filter. The POD and DMD have successfully recovered the slow body kink mode with the azimuthal motion, and also have recovered the fundamental slow body sausage mode.

7.1.3 Chapter 5

In this Chapter we have expanded our analysis presented in Chapter 4 by applying the POD and DMD on two different sunspots; one having a circular cross-sectional shape (the same one in 4) and the other one has an elliptical cross-sectional shape. The observed modes were compared with the theoretical models (assuming a waveguide with cylindrical and elliptical cross-section) and the model that corresponds to the actual shape of the sunspots.

For the circular sunspot, the sausage overtone ($n = 0$) and the higher order modes ($n = 2$ and $n = 3$) were observed, in addition to the fundamental slow body modes that were determined in Chapter 4. In the elliptical sunspot the fundamental slow body modes, kink overtone ($n = 1$) and the higher order modes ($n = 2$ and $n = 3$) were observed. We have also found that when the observed modes are compared with the results that were predicted by the model involving irregular shape, modes have a better agreement than when comparing them with the results corresponding to a waveguide with elliptical cross-section. Moreover, the vertical wavenumber (k_z) of all observed modes were calculated, and are shown in Tables 5.1 and 5.2 for the circular and elliptical sunspots, respectively.

7.1.4 Chapter 6

Our analysis presented in the previous Chapters assumed that the boundary of the sunspots' umbra was assumed to be stationary. In reality, observations show that this boundary is changing its shape in time and the temporal scale of these changes are comparable with the periods of waves. Therefore, in this Chapter, we have applied the POD and DMD techniques on a dataset which clearly showed the change in the shape of the boundary. Our analysis has been carried out on a long time series (3 hours long) of Doppler velocity dataset. The dataset was divided into ten time intervals (T_i), and for every T_i the shape

of the boundary is slightly changing. The theoretical modes of the model that correspond to the real shape of sunspot were obtained at every T_i.

Then, the POD and DMD were applied at every time interval, and the observed modes were compared with the theoretical predictions. As a result of that, we have observed, at most time intervals, the damped fast surface kink mode, and the fundamental slow body sausage mode. Fluting ($n = 2$) modes were observed at partial time, and that may be explained due to the wide range of the spatial observation.

The results presented in the Thesis and the techniques used for wave detection may have important implications for the interpretation of observational data from next generation ground-based observing facilities (for example, the new 4m DKIST solar telescope, Solar Orbiter (ESA) and European Solar Telescope (EST)).

7.2 Future work

The theoretical models explaining the nature and properties of MHD waves propagating in cylindrical (Edwin and Roberts, 1983) and the elliptical (Aldhafeeri et al., 2021) cross-sectional magnetic waveguides are well developed, however these are mostly ideal models. High resolution observations showed that in reality the shape and structure of the waveguides is far from being ideal, the cross-sectional shape not symmetrical, the waveguide does not have a homogeneous distribution of density and magnetic field, etc. Moreover, these properties are changing in time that can modify the properties of waves during their propagation. We have shown in Chapter 5, the higher-order modes are sensitive and affected by the shape of the waveguide and have a clear agreement with model that corresponds to the actual shape of the sunspot.

One important way of expanding the current research in this field is to develop the theoretical model describing waves in a sunspot having irregular shape such that it can predict the appearance of surface modes, too. This would imply another type of approach than presented in this thesis (in terms of governing equations, boundary conditions, etc.).

The POD and DMD analysis presented in Chapters 4 and 5 was applied on sunspots with a circular and elliptical cross-sectional shapes, respectively. The MHD wave modes in the circular and elliptical models are governed, in the radial direction, by Bessel and Mathieu functions, respectively. These functions are orthogonal to each other, which will give the POD the power

to detect the modes. However, the magnetic waveguides may have a shape neither circular nor elliptical, and as a result, of that, the shape may lose the property of orthogonality in space, i.e. the POD will not work well to detect modes. In contrast, the DMD will be able to decompose the signal, but the challenge is to know what are the dominant frequencies as the POD is no longer working. Therefore, as an important future extension of Chapter 5, we could try to apply the POD and DMD techniques on a sunspot whose shape is far from being a circle or ellipse.

The research presented in Chapter 6 can also be expanded by carrying out the POD and DMD techniques to identify MHD wave modes on a long time series applied to a waveguide of arbitrary shape that is changing in time.

APPENDIX A

Appendix

A.1 Numerical algorithm used to solve the dispersion relations

In this section we present an algorithm designed to solve the dispersion relation for a cylindrical magnetic flux tube (see, Figures 2.6 and 2.7) as Edwin and Roberts (1983).

Equation (2.34) can be rewritten in terms of the phase speed ($v_{ph} = \omega/k_z$) as

$$\rho_0(v_{A_0}^2 - v_{ph}^2)m_{e_1}\frac{K_n'(m_{e_1}k_z a)}{K_n(m_{e_1}k_z a)} - \rho_e(v_{A_e}^2 - v_{ph}^2)m_{0_1}\frac{I_n'(m_{0_1}k_z a)}{I_n(m_{0_1}k_z a)} = 0 \qquad \text{(A.1)}$$

for the surface waves ($m_0^2 > 0$), and a similar equation for the body waves ($m_0^2 = -n_0^2 < 0$) with replacing $I_n(m_{0_1}ka)$ and $I_n'(m_{0_1}ka)$ to be $J_n(n_{0_1}ka)$ and $J_n'(n_{0_1}ka)$. In the above relations the modified magneto-acoustic paramaters m_{0_1} and m_{e_1} are defined as

$$m_{0_1}^2 = \frac{(c_0^2 - v_{ph}^2)(v_{A_0}^2 - v_{ph}^2)}{(c_0^2 + v_{A_0}^2)(c_{T_0}^2 - v_{ph}^2)} \quad \text{and} \quad m_{e_1}^2 = \frac{(c_e^2 - v_{ph}^2)(v_{A_e}^2 - v_{ph}^2)}{(c_e^2 + v_{A_e}^2)(c_{T_e}^2 - v_{ph}^2)}. \qquad \text{(A.2)}$$

Equation (A.1) is function of two variables, the phase speed v_{ph} of waves and the dimensionless quantity ka.

Numerically, we have taken ka along the x-axis as fixed points and we have tested the v_{ph} vertically along the y-axis. The algorithm that we have used to test v_{ph} is to discretise the y-axis into a small intervals such as

$$v_{ph} = \{[v_0, v_1] \cup [v_1, v_2] \cup, \cdots, \cup [v_{n-1}, v_n]\}$$

where v_0 and v_n are the minimum and the maximum values of v_{ph} along y-axis

respectively, whit $v_i - v_{i-1} = \epsilon$
1 and $i = 1, 2, \cdots, n$. As a result, each interval has an upper and a lower limit. Let $f_1(v_{ph}, ka) = 0$ be the dispersion relations for the sausage modes. For a fixed ka and for each intervals of v_{ph}, we have tested the product of $f_1(v_l, ka) \times f_1(v_u, ka)$, where v_l and v_u are the lower and the upper limits of each intervals. If the sign of the product is negative, hence there is a solution in the interval, otherwise there is no solution. Finally, we have taken all intervals that included solutions and we applied the bisection method to find the solution. Similarly, for all values of ka along the x-axis, we obtain the solution for the sausage mode.

A.2 The correlation between the observed modes and the theoretical modes in Chapter 6

To obtain the correlation between the theoretical modes shown in Figure 6.2 and the POD modes in Figure 6.3, we have applied cross-correlation analysis, calculated on a pixel-by-pixel basis, at all time intervals (T_i). For every correlation matrix we have taken the summation of the pixels, and hence every correlation of the observed mode and the theoretical mode is represented as an integer. As a result of that, we have obtained the correlation panels shown in Figure A.1, where every panel refers to different time interval (T_i). For example, upper left panel of Figure A.1, labelled with T_1, refers to the correlation of the POD modes in the first row of Figure 6.3 and theoretical modes in the first row of Figure 6.2. At the end, every column of the correlation panels are normalised by the maximum value of that column along all time intervals. This step is required to make the correlation of higher order modes to be visible. Without this step, the correlation of the sausage and kink mode will be the dominant and other modes will not be visible as high correlation. However, the higher correlations need to be checked and validated in order to be considered.

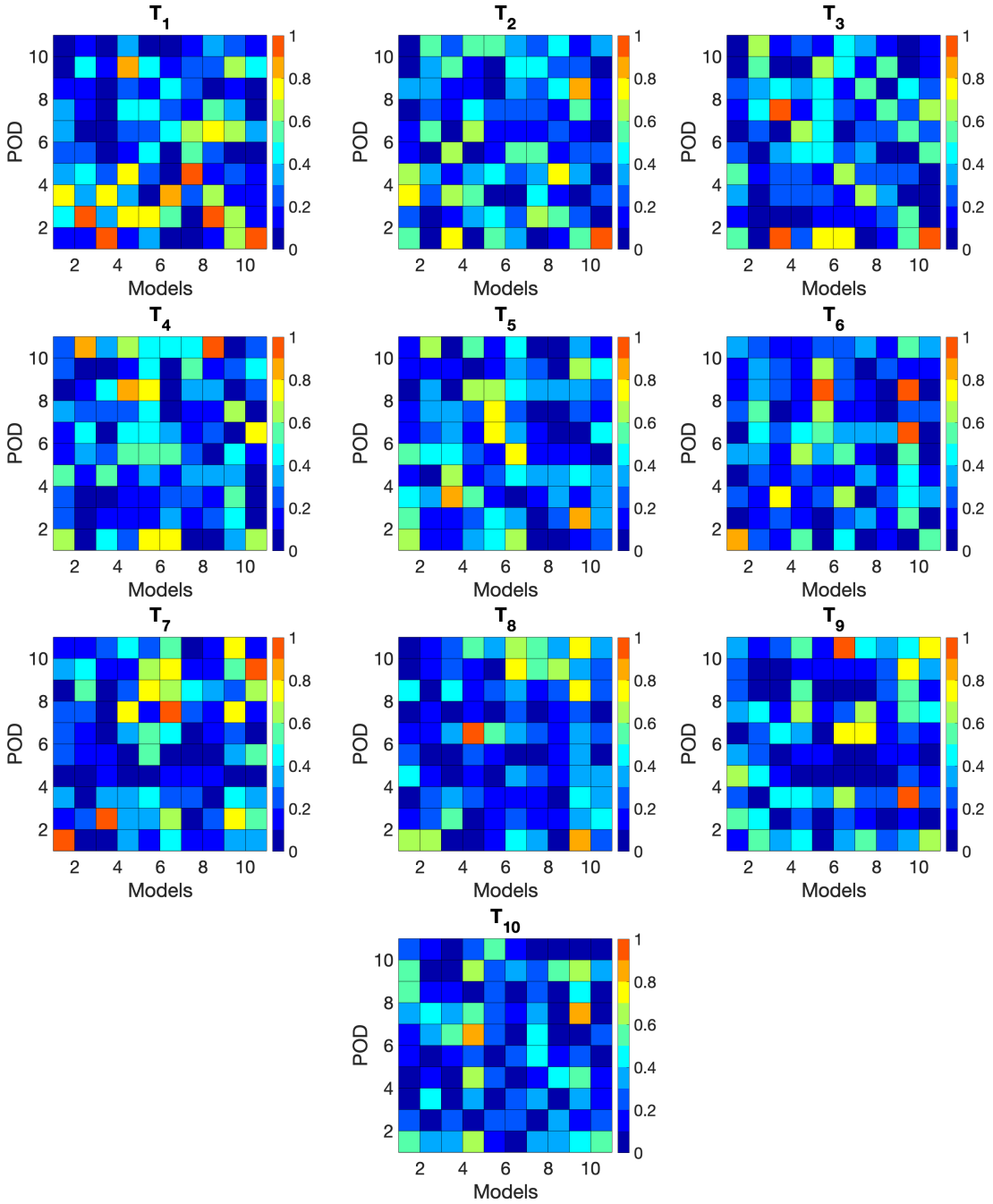

Figure A.1: This figure shows the summation of pixels in the correlation matrix between models in Figure 6.2 and POD modes in Figure 6.3, for every T_i. The colorbar shows the amplitude of the summation of the correlation matrix, while every column along the time intervals were normalised by the maximum.

Bibliography

Albidah, A. B., Brevis, W., Fedun, V., Ballai, I., Jess, D. B., Stangalini, M., Higham, J. and Verth, G. (2021), 'Proper orthogonal and dynamic mode decomposition of sunspot data', *Philosophical Transactions of the Royal Society A* **379**(2190), 20200181.

Albidah, A. B., Fedun, V., Aldhafeeri, A. A., Ballai, I., Brevis, W., Jess, D. B., Higham, J., Stangalini, M., Silva, S. S. A. and Verth, G. (2022), 'Magnetohydrodynamic wave mode identification in circular and elliptical sunspot umbrae: Evidence for high-order modes', *The Astrophysical Journal* **927**(2), 201.

Aldhafeeri, A. A., Verth, G., Brevis, W., Jess, D. B., McMurdo, M. and Fedun, V. (2021), 'Magnetohydrodynamic wave modes of solar magnetic flux tubes with an elliptical cross section', *The Astrophysical Journal* **912**(1), 50.

Alfvén, H. (1942), 'Existence of Electromagnetic-Hydrodynamic Waves', *Nature* **150**(3805), 405–406.

Arlt, R. (2014), 'Sunspots from the past, treasures for today', *Astronomy & Geophysics* **55**(3), 3–24.

Aschwanden, M. (2004), 'Physics of the solar corona. an introduction, ed. aschwanden, mj'.

Aschwanden, M. (2006), *Physics of the solar corona: an introduction with problems and solutions*, Springer Science & Business Media.

Avrett, E. H. and Loeser, R. (2008), 'Models of the solar chromosphere and transition region from sumer and hrts observations: formation of the extreme-ultraviolet spectrum of hydrogen, carbon, and oxygen', *The Astrophysical Journal Supplement Series* **175**(1), 229.

Bagheri, S. (2013), 'Koopman-mode decomposition of the cylinder wake', *Journal of Fluid Mechanics* **726**, 596–623.

Balthasar, H. and Schmidt, W. (1993), 'Polarimetry and spectroscopy of a simple sunspot. 2: On the height and temperature dependence of the magnetic field', *Astron. Astrophys.* **279**(1), 243–250.

Banerjee, D., O'Shea, E., Goossens, M., Doyle, J. and Poedts, S. (2002), 'On the theory of mag waves and a comparison with sunspot observations from cds/soho', *Astronomy & Astrophysics* **395**(1), 263–277.

Beckers, J. M. and Tallant, P. E. (1969), 'Chromospheric inhomogeneities in sunspot umbrae', *Solar Physics* **7**, 351–365.

Beckers, J. and Schultz, R. (1972), 'Oscillatory motions in sunspots', *Solar Physics* **27**(1), 61–70.

Berry, M., Magstadt, A. and Glauser, M. N. (2017), 'Application of pod on time-resolved schlieren in supersonic multi-stream rectangular jets', *Physics of Fluids* **29**(2), 020706.

Bhatnagar, A. (1971), On the oscillatory velocity field in sunspot atmosphere., *in* 'Bulletin of the American Astronomical Society', Vol. 3, p. 259.

Bhatnagar, A. and Tanaka, K. (1972), 'Intensity oscillation in hα-fine structure', *Solar Physics* **24**(1), 87–97.

Brisken, W. F. and Zirin, H. (1997), 'New data and models of running penumbral waves in sunspots', *The Astrophysical Journal* **478**(2), 814.

Brynildsen, N., Maltby, P., Fredvik, T., Kjeldseth-Moe, O. and Wilhelm, K. (2001), 'Sunspot plumes and flow channels', *Solar Physics* **198**(1), 89–131.

Buss, A. A. (1926), 'Persistent solar prominences', *Nature* **118**(2968), 412–412.

Capitaine, N., Klioner, S. and McCarthy, D. (2012), 'The re-definition of the astronomical unit of length: reasons and consequences', *IAU Joint Discussion* **7**, 40.

Chae, J., Yang, H., Park, H., Maurya, R. A., Cho, K.-S. and Yurchysyn, V. (2014), 'Superpenumbral fibrils powered by sunspot oscillations', *The Astrophysical Journal* **789**(2), 108.

Christopoulou, E., Skodras, A., Georgakilas, A. and Koutchmy, S. (2003), 'Wavelet analysis of umbral oscillations', *The Astrophysical Journal* **591**(1), 416.

Di Stefano, L., Mattoccia, S. and Tombari, F. (2005), 'Zncc-based template matching using bounded partial correlation', *Pattern recognition letters* **26**(14), 2129–2134.

Dorotovič, I., Erdélyi, R., Freij, N., Karlovskỳ, V. and Márquez, I. (2014), 'Standing sausage waves in photospheric magnetic waveguides', *Astronomy & Astrophysics* **563**, A12.

Eckart, C. and Young, G. (1936), 'The approximation of one matrix by another of lower rank', *Psychometrika* **1**(3), 211–218.

Edwin, P. and Roberts, B. (1982), 'Wave propagation in a magnetically structured atmosphere', *Solar Physics* **76**(2), 239–259.

Edwin, P. and Roberts, B. (1983), 'Wave propagation in a magnetic cylinder', *Solar Physics* **88**(1-2), 179–191.

Fludra, A. (1999), 'Intensity oscillations in a sunspot plume', *Astronomy and Astrophysics* **344**, L75–L78.

Fludra, A. (2001), 'Transition region oscillations above sunspots', *Astronomy & Astrophysics* **368**(2), 639–651.

Foukal, P. V., Noyes, R. W., Reeves, E. M., Schmahl, E. J., Timothy, J. G., Vernazza, J. E., Wilhbroe, G. L. and Huber, M. C. E. (1974), 'Extreme-Ultraviolet Observations of Sunspots with the Harvard Spectrometer on the Apollo Telescope Mount', *Astrophys. J. Lett.* **193**, L143.

Fritts, D. C., Wang, L., Baumgarten, G., Miller, A. D., Geller, M. A., Jones, G., Limon, M., Chapman, D., Didier, J., Kjellstrand, C. B. et al. (2017), 'High-resolution observations and modeling of turbulence sources, structures, and intensities in the upper mesosphere', *Journal of Atmospheric and Solar-Terrestrial Physics* **162**, 57–78.

Giovanelli, R. (1972), 'Oscillations and waves in a sunspot', *Solar Physics* **27**(1), 71–79.

Gopalakrishnan, S. G., Marks Jr, F., Zhang, J. A., Zhang, X., Bao, J.-W. and Tallapragada, V. (2013), 'A study of the impacts of vertical diffusion on the structure and intensity of the tropical cyclones using the high-resolution hwrf system', *Journal of the atmospheric sciences* **70**(2), 524–541.

Grant, S. D. T., Jess, D. B., Zaqarashvili, T. V., Beck, C., Socas-Navarro, H., Aschwanden, M. J., Keys, P. H., Christian, D. J., Houston, S. J. and Hewitt, R. L. (2018), 'Alfvén wave dissipation in the solar chromosphere', *Nature Physics* **14**(5), 480–483.

Grilli, M., Vázquez-Quesada, A. and Ellero, M. (2013), 'Transition to turbulence and mixing in a viscoelastic fluid flowing inside a channel with a periodic array of cylindrical obstacles', *Physical review letters* **110**(17), 174501.

Gurman, J., Leibacher, J., Shine, R., Woodgate, B. and Henze, W. (1982), 'Transition region oscillations in sunspots', *The Astrophysical Journal* **253**, 939–948.

Hale, G. E. (1908*a*), 'On the Probable Existence of a Magnetic Field in Sun-Spots', *Astrophys. J.* **28**, 315.

Hale, G. E. (1908*b*), 'The Tower Telescope of the Mount Wilson Solar Observatory', *Astrophys. J.* **27**, 204.

Hawking, S. (2002), *On the shoulders of giants : the great works of physics and astronomy.*

Hemati, M. S., Williams, M. O. and Rowley, C. W. (2014), 'Dynamic mode decomposition for large and streaming datasets', *Physics of Fluids* **26**(11), 111701.

Henze, W., Tandberg-Hanssen, E., Reichmann, E. and Athay, R. (1984), 'Smm/uvsp observations of the distribution of transition region oscillations and other properties in a sunspot', *Solar physics* **91**(1), 33–44.

Higham, J. and Brevis, W. (2018), 'Modification of the modal characteristics of a square cylinder wake obstructed by a multi-scale array of obstacles', *Experimental Thermal and Fluid Science* **90**, 212–219.

Higham, J., Brevis, W. and Keylock, C. (2018), 'Implications of the selection of a particular modal decomposition technique for the analysis of shallow flows', *Journal of Hydraulic Research* **56**(6), 796–805.

Higham, J., Brevis, W., Keylock, C. and Safarzadeh, A. (2017), 'Using modal decompositions to explain the sudden expansion of the mixing layer in the wake of a groyne in a shallow flow', *Advances in Water Resources* **107**, 451–459.

Higham, J., Shahnam, M. and Vaidheeswaran, A. (2020), 'Using a proper orthogonal decomposition to elucidate features in granular flows', *Granular Matter* **22**(4), 1–13.

Higham, J., Vaidheeswaran, A., Brevis, W., Nicolleau, F. and Marlow, J. (2021), 'Modification of modal characteristics in wakes of square cylinders with multi-scale porosity', *Physics of Fluids* **33**(4), 045117.

Hufbauer, K. (1991), *Exploring the sun : solar science since Galileo.*

Jess, D. B., Mathioudakis, M., Christian, D. J., Keenan, F. P., Ryans, R. S. I. and Crockett, P. J. (2010), 'ROSA: A High-cadence, Synchronized Multi-camera Solar Imaging System', *Solar Phys.* **261**(2), 363–373.

Jess, D. B., Morton, R. J., Verth, G., Fedun, V., Grant, S. D. T. and Giagkiozis, I. (2015), 'Multiwavelength Studies of MHD Waves in the Solar Chromosphere. An Overview of Recent Results', *Space Sci. Rev.* **190**(1-4), 103–161.

Jess, D. B., Reznikova, V. E., Ryans, R. S., Christian, D. J., Keys, P. H., Mathioudakis, M., Mackay, D. H., Prasad, S. K., Banerjee, D., Grant, S. D. et al. (2016), 'Solar coronal magnetic fields derived using seismology techniques applied to omnipresent sunspot waves', *Nature Physics* **12**(2), 179–185.

Jess, D. B., Shelyag, S., Mathioudakis, M., Keys, P. H., Christian, D. J. and Keenan, F. P. (2012), 'Propagating wave phenomena detected in observations and simulations of the lower solar atmosphere', *The Astrophysical Journal* **746**(2), 183.

Jess, D. B., Van Doorsselaere, T., Verth, G., Fedun, V., Prasad, S. K., Erdélyi, R., Keys, P. H., Grant, S. D., Uitenbroek, H. and Christian, D. J. (2017), 'An inside look at sunspot oscillations with higher azimuthal wavenumbers', *The Astrophysical Journal* **842**(1), 59.

Jess, D., Reznikova, V., Van Doorsselaere, T., Keys, P. and Mackay, D. (2013), 'The influence of the magnetic field on running penumbral waves in the solar chromosphere', *The Astrophysical Journal* **779**(2), 168.

Jing, J., Li, Q., Liu, C., Lee, J., Xu, Y., Cao, W. and Wang, H. (2019), 'High-resolution observations of dynamics of superpenumbral hα fibrils', *The Astrophysical Journal* **880**(2), 143.

Jovanović, M. R., Schmid, P. J. and Nichols, J. W. (2014), 'Sparsity-promoting dynamic mode decomposition', *Physics of Fluids* **26**(2), 024103.

Jurčák, J., Bello González, N., Schlichenmaier, R. and Rezaei, R. (2015), 'A distinct magnetic property of the inner penumbral boundary. Formation of a stable umbra-penumbra boundary in a sunspot', *Astron. Astrophys.* **580**, L1.

Kang, J., Chae, J., Nakariakov, V. M., Cho, K., Kwak, H. and Lee, K. (2019), 'The Physical Nature of Spiral Wave Patterns in Sunspots', *Astrophys. J. Lett.* **877**(1), L9.

Keys, P. H., Morton, R. J., Jess, D. B., Verth, G., Grant, S. D., Mathioudakis, M., Mackay, D. H., Doyle, J. G., Christian, D. J., Keenan, F. P. et al. (2018), 'Photospheric observations of surface and body modes in solar magnetic pores', *The Astrophysical Journal* **857**(1), 28.

Khomenko, E. and Collados, M. (2015), 'Oscillations and waves in sunspots', *Living Reviews in Solar Physics* **12**(1), 1–78.

Kobanov, N. and Makarchik, D. (2004), 'Propagating waves in the sunspot umbra chromosphere', *Astronomy & Astrophysics* **424**(2), 671–675.

Kopp, G. and Rabin, D. (1992), 'A relation between magnetic field strength and temperature in sunspots', *Solar physics* **141**(2), 253–265.

Langhans, K., Scharmer, G., Kiselman, D., Löfdahl, M. and Berger, T. (2005), 'Inclination of magnetic fields and flows in sunspot penumbrae', *Astronomy & Astrophysics* **436**(3), 1087–1101.

Leighton, R. B., Noyes, R. W. and Simon, G. W. (1962), 'Velocity Fields in the Solar Atmosphere. I. Preliminary Report.', *Astrophys. J.* **135**, 474.

Lighthill, M. J. (1960), 'Studies on magneto-hydrodynamic waves and other anisotropic wave motions', *Philosophical Transactions of the Royal Society of London. Series A, Mathematical and Physical Sciences* **252**(1014), 397–430.

Lites, B. (1984), 'Photoelectric observations of chromospheric sunspot oscillations. ii-propagation characteristics', *The Astrophysical Journal* **277**, 874–888.

Lites, B. (1986*a*), 'Photoelectric observations of chromospheric sunspot oscillations. iv-the ca ii h line and he i 10830 a', *The Astrophysical Journal* **301**, 1005–1017.

Lites, B. W. (1986*b*), 'Photoelectric Observations of Chromospheric Sunspot Oscillations. III. Spatial Distribution of Power and Frequency in Umbrae', *Astrophys. J.* **301**, 992.

Lites, B. W. (1992), Sunspot Oscillations - Observations and Implications, *in* J. H. Thomas and N. O. Weiss, eds, 'Sunspots. Theory and Observations', Vol. 375 of *NATO Advanced Study Institute (ASI) Series C*, p. 261.

Livingston, W., Harvey, J., Malanushenko, O. and Webster, L. (2006), 'Sunspots with the strongest magnetic fields', *Solar Physics* **239**(1), 41–68.

Lumley, J. L. (1967), 'The structure of inhomogeneous turbulent flows', *Atmospheric turbulence and radio wave propagation* .

Maltby, P., Brynildsen, N., Kjeldseth-Moe, O. and Wilhelm, K. (2001), 'Plumes and oscillations in the sunspot transition region', *Astronomy & Astrophysics* **373**(1), L1–L4.

Mitalas, R. and Sills, K. (1992), 'On the photon diffusion time scale for the sun', *The Astrophysical Journal* **401**, 759.

Moore, R. (1981), 'Dynamic phenomena in the visible layers of sunspots', *Space Science Reviews* **28**(4), 387–421.

Morton, R. J., Verth, G., Jess, D. B., Kuridze, D., Ruderman, M. S., Mathioudakis, M. and Erdélyi, R. (2012), 'Observations of ubiquitous compressive waves in the sun's chromosphere', *Nature Communications* **3**(1), 1–8.

Mumford, S. J., Freij, N., Christe, S., Ireland, J., Mayer, F., Stansby, D., Shih, A. Y., Hughitt, V. K., Ryan, D. F., Liedtke, S., Pérez-Suárez, D., I., V. K., Hayes, L., Chakraborty, P., Inglis, A., Pattnaik, P., Sipőcz, B., Sharma, R., Leonard, A., Hewett, R., Hamilton, A., Manhas, A., Panda, A., Earnshaw, M., Barnes, W., Choudhary, N., Kumar, A., Singh, R., Chanda, P., Haque, M. A., Kirk, M. S., Konge, S., Mueller, M., Srivastava, R., Jain, Y., Bennett, S., Baruah, A., Arbolante, Q., Maloney, S., Charlton, M., Mishra, S., Chorley, N., Himanshu, Chouhan, A., Modi, S., Mason, J. P., Sharma, Y., Naman9639, Zivadinovic, L., Rozo, J. I. C., Bobra, M. G., Manley, L., Paul, J. A., Ivashkiv, K., Chatterjee, A., Stern, K. A., von Forstner, J. F., Bazán,

J., Jain, S., Evans, J., Ghosh, S., Malocha, M., Stańczak, D., SophieLemos, Verma, S., Visscher, R. D., Singh, R. R., Airmansmith97, Buddhika, D., Pathak, H., Alam, A., Agrawal, A., Sharma, S., Rideout, J. R., Bates, M., Park, J., Mishra, P., Goel, D., Sharma, D., Taylor, G., Cetusic, G., Reiter, G., Jacob, Inchaurrandieta, M., Dacie, S., Dubey, S., Parkhi, U., Sidhu, S., Surve, R., Eigenbrot, A., Meszaros, T., Bray, E. M., Zahniy, S., Guennou, C., Bose, A., Ankit, Chicrala, A., J, A., D'Avella, D., Ballew, J., Price-Whelan, A., Robitaille, T., Augspurger, T., Murphy, N., Lodha, P., Krishan, Y., Pandey, A., honey, Verma, D., neerajkulk, Williams, D., Wiedemann, B. M., Kothari, Y., mridulpandey, Habib, I., Molina, C., Mampaey, B., Streicher, O., Nomiya, Y., Gomillion, R., Letts, J., Bhope, A., Hill, A., Keşkek, D., Ranjan, K., Pereira, T. M. D., Dang, T. K., Bankar, V., Bahuleyan, A., B, A., Stevens, A. L., Agrawal, Y., nakul shahdadpuri, Ghosh, K., Hiware, K., yasintoda, Krishna, K., Lyes, M. M., Mangaonkar, M., Cheung, M., platipo, Buitrago-Casas, J. C., Mendero, M., Dedhia, M., Wimbish, J., Calixto, J., Babuschkin, I., Schoentgen, M., Mathur, H., Kumar, G., Verstringe, F., Dover, F. M., Tollerud, E., Gyenge, N. G., Arias, E., Mekala, R. R., MacBride, C., Das, R., Mishra, R., Stone, B., resakra, Agarwal, S., Chaudhari, K., Kustov, A., Smith, A., Srikanth, S., Jain, S., Mehrotra, A., Gaba, A. S., Kannojia, S., Yadav, T., Paul, T., Wilkinson, T. D., Caswell, T. A. and Murray, S. A. (2021), 'Sunpy'.
URL: *https://doi.org/10.5281/zenodo.4762113*

Murray, N. E. and Ukeiley, L. S. (2007), 'An application of gappy pod', *Experiments in Fluids* **42**(1), 79–91.

Nagashima, K., Sekii, T., Kosovichev, A. G., Shibahashi, H., Tsuneta, S., Ichimoto, K., Katsukawa, Y., Lites, B., Nagata, S., Shimizu, T. et al. (2007), 'Observations of sunspot oscillations in g band and ca ii h line with solar optical telescope on hinode', *Publications of the Astronomical Society of Japan* **59**(sp3), S631–S636.

O'shea, E., Muglach, K. and Fleck, B. (2002), 'Oscillations above sunspots: Evidence for propagating waves?', *Astronomy & Astrophysics* **387**(2), 642–664.

Parker, E. (1974), 'The nature of the sunspot phenomenon. ii: Internal overstable modes', *Solar Physics* **37**, 127–144.

Parker, E. N. (1958), 'Dynamics of the interplanetary gas and magnetic fields.', *The Astrophysical Journal* **128**, 664.

Pearson, K. (1901), 'Liii. on lines and planes of closest fit to systems of points in space', *The London, Edinburgh, and Dublin Philosophical Magazine and Journal of Science* **2**(11), 559–572.

Pesnell, W. D., Thompson, B. J. and Chamberlin, P. C. (2011), 'The solar dynamics observatory (SDO)', *Solar Physics* **275**(1-2), 3–15.
URL: *https://doi.org/10.1007/s11207-011-9841-3*

Phillis, G. L. (1975), 'Hα oscillations in sunspot umbrae', *Solar Physics* **41**(1), 71–79.

Priest, E. (2014), *Magnetohydrodynamics of the Sun*, Cambridge University Press.

Roberts, B. (1981*a*), 'Wave propagation in a magnetically structured atmosphere, surface waves at a magnetic interface', *Solar Physics* **69**(1), 27–38.

Roberts, B. (1981*b*), 'Wave propagation in a magnetically structured atmosphere, waves in a magnetic slab', *Solar Physics* **69**(1), 39–56.

Rouppe van der Voort, L. H. M., Rutten, R. J., Sütterlin, P., Sloover, P. J. and Krijger, J. M. (2003), 'La Palma observations of umbral flashes', *Astron. Astrophys.* **403**, 277–285.

Rowley, C. W., MEZI?, I., Bagheri, S., Schlatter, P., HENNINGSON, D. et al. (2009), 'Spectral analysis of nonlinear flows', *Journal of fluid mechanics* **641**(1), 115–127.

Rueedi, I., Solanki, S. K. and Livingston, W. C. (1995), 'Infrared lines as probes of solar magnetic features. X. HeI 10830A as a diagnostic of chromospheric magnetic fields.', *Astron. Astrophys.* **293**, 252–262.

Schlichenmaier, R., Rezaei, R., Bello González, N. and Waldmann, T. A. (2010), 'The formation of a sunspot penumbra', *Astron. Astrophys.* **512**, L1.

Schmid, P. J. (2010), 'Dynamic mode decomposition of numerical and experimental data', *Journal of fluid mechanics* **656**, 5–28.

Schou, J., Scherrer, P. H., Bush, R. I., Wachter, R., Couvidat, S., Rabello-Soares, M. C., Bogart, R. S., Hoeksema, J. T., Liu, Y., Duvall, T. L., Akin, D. J., Allard, B. A., Miles, J. W., Rairden, R., Shine, R. A., Tarbell, T. D., Title, A. M., Wolfson, C. J., Elmore, D. F., Norton, A. A. and Tomczyk, S. (2011), 'Design and ground calibration of the helioseismic and magnetic imager (HMI) instrument on the solar dynamics observatory (SDO)', *Solar Physics* **275**(1-2), 229–259.
URL: *https://doi.org/10.1007/s11207-011-9842-2*

Sirovich, L. (1987), 'Turbulence and the dynamics of coherent structures, parts i, ii and iii', *Quart. Appl. Math.* pp. 561–590.

Sobotka, M. and Hanslmeier, A. (2005), 'Photometry of umbral dots', *Astronomy & Astrophysics* **442**(1), 323–329.

Solanki, S. K. (2003), 'Sunspots: An overview', *Astron. Astrophys. Rev.* **11**(2-3), 153–286.

Solar Dynamics Observatory (SDO) (n.d.), https://sdo.gsfc.nasa.gov Solar Dynamics Observatory (SDO) . Accessed: 2021-12-03.

Spruit, H. (1982), 'Propagation speeds and acoustic damping of waves in magnetic flux tubes', *Solar Physics* **75**(1), 3–17.

Stangalini, M., Del Moro, D., Berrilli, F. and Jefferies, S. (2011), 'Mhd wave transmission in the sun's atmosphere', *Astronomy & Astrophysics* **534**, A65.

Stangalini, M., Jess, D. B., Verth, G., Fedun, V., Fleck, B., Jafarzadeh, S., Keys, P. H., Murabito, M., Calchetti, D., Aldhafeeri, A. A., Berrilli, F., Del Moro, D., Jefferies, S. M., Terradas, J. and Soler, R. (2021), 'A novel approach to identify resonant MHD wave modes in solar pores and sunspot umbrae: B $-$ ω analysis', *Astron. Astrophys.* **649**, A169.

Stangalini, M., Verth, G., Fedun, V., Aldhafeeri, A. A., Jess, D. B., Jafarzadeh, S., Keys, P. H., Fleck, B., Terradas, J., Murabito, M., Ermolli, I., Soler, R., Giorgi, F. and MacBride, C. D. (2022), 'Large scale coherent magnetohydrodynamic oscillations in a sunspot', *Nature Communications* **13**, 479.

Tahmasebi, P., Hezarkhani, A. and Sahimi, M. (2012), 'Multiple-point geostatistical modeling based on the cross-correlation functions', *Computational Geosciences* **16**(3), 779–797.

Taira, K., Brunton, S. L., Dawson, S. T., Rowley, C. W., Colonius, T., McKeon, B. J., Schmidt, O. T., Gordeyev, S., Theofilis, V. and Ukeiley, L. S. (2017), 'Modal analysis of fluid flows: An overview', *Aiaa Journal* **55**(12), 4013–4041.

Tavabi, E., Koutchmy, S. and Ajabshirizadeh, A. (2012), 'solar spicules and jets', *EAS Publications Series* **55**, 71–78.

The SunPy Community, Barnes, W. T., Bobra, M. G., Christe, S. D., Freij, N., Hayes, L. A., Ireland, J., Mumford, S., Perez-Suarez, D., Ryan, D. F., Shih, A. Y., Chanda, P., Glogowski, K., Hewett, R., Hughitt, V. K., Hill, A., Hiware, K., Inglis, A., Kirk, M. S. F., Konge, S., Mason, J. P., Maloney, S. A., Murray, S. A., Panda, A., Park, J., Pereira, T. M. D., Reardon, K., Savage, S., Sipőcz, B. M., Stansby, D., Jain, Y., Taylor, G., Yadav, T., Rajul and Dang, T. K. (2020), 'The sunpy project: Open source development and status of the version 1.0 core package', *The Astrophysical Journal* **890**, 68–. **URL:** *https://iopscience.iop.org/article/10.3847/1538-4357/ab4f7a*

The Space Place Webpage of NASA (n.d.), https://spaceplace.nasa.gov The Space Place Webpage of NASA . Accessed: 2021-12-03.

The Swedish Solar Telescope (SST) (n.d.), https://www.iac.es/en?op1=2&op2=3&id=10 The Swedish Solar Telescope (SST) . Accessed: 2021-12-03.

Thomas, J. H., Cram, L. E. and Nye, A. H. (1984), 'Dynamical phenomena in sunspots. I - Observing procedures and oscillatory phenomena.', *Astrophys. J.* **285**, 368–385.

Thomas, J. H., Weiss, N. O., Tobias, S. M. and Brummell, N. H. (2002), 'Downward pumping of magnetic flux as the cause of filamentary structures in sunspot penumbrae', *Nature* **420**(6914), 390–393.

Watanabe, H., Kitai, R. and Ichimoto, K. (2009), 'Characteristic dependence of umbral dots on their magnetic structure', *The Astrophysical Journal* **702**(2), 1048.

Wentzel, D. (1979), 'Hydromagnetic surface waves', *The Astrophysical Journal* **227**, 319–322.

Wittmann, A. (1969), 'Some properties of umbral flashes', *Solar Physics* **7**, 366–369.

Yuan, D. (2015), 'Signature of high-order azimuthal mhd body modes in sunspot's low atmosphere', *Research in Astronomy and Astrophysics* **15**(9), 1449.

Zhou, X. and Liang, H. (2017), 'The relationship between the 5-min oscillation and 3-min oscillations at the umbral/penumbral sunspot boundary', *Astrophysics and Space Science* **362**(3), 46.

Zirin, H. and Stein, A. (1972), 'Observations of running penumbral waves', *The Astrophysical Journal* **178**, L85.